NUMERICAL INVESTIGATION OF GAS TRANSPORT THROUGH MICRO/NANO-SCALE POROUS MEDIA AT SLIP FLOW REGIME

A Thesis Submitted to
the Graduate School of Engineering and Sciences of
İzmir Institute of Technology
in Partial Fulfillment of the Requirements for the Degree of

DOCTOR OF PHILOSOPHY

in Mechanical Engineering

by
Safa SABET

November 2021
İZMİR

To my beloved grandfather, Mohammad Bagher Sabet

ACKNOWLEDGMENTS

Firstly, I would like to be thankful to my advisor Assoc. Prof. Dr. Murat Barışık for supporting my PhD study. Without his endless support, excellent guidance, and patience this thesis or research would not have been possible. His guidance helped me in all the time of research and writing of this thesis. Also, I would like to express my sincere gratitude to my co-advisor Prof. Manca and Dr. Buonomo for providing me the opportunity to complete my thesis at Università degli Studi della Campania Luigi Vanvitelli. I especially want to thank them, whose support and guidance made my thesis work possible. I also would like to thank my examining committee members, Assoc. Prof. Erdal Çetkin, Prof. Sacide Alsoy Altınkaya, Prof. Aytunç Erek and Assoc. Prof. Sercan Acarer for their valuable contributions to this dissertation.

Additionally, I am very grateful for the friendship of all of the members of MiNaEng research group. In particular I would like to thank to my friends Gökberk Özçelik, Cihan Özdemir, Öykü Alan, Gülce Kalyoncu and Tümcan Şen.

I would like to be thankful to Parisa and Hamidreza for their helps. My sincere thanks also go to my aunt Mensure, Sevil's family, my grandmother, and my dear friend Ramin for their supports during writing my thesis.

Finally, and most importantly, I take this opportunity to express my appreciation from my deep heart to my father Sadegh and my valuable sister Parinaz. Also, I am very thankful to my unique love Seda. They were always supporting and encouraging me with their best wishes. It would be really challenging for me to end up this period without their presence.

ABSTRACT

NUMERICAL INVESTIGATION OF GAS TRANSPORT THROUGH MICRO/NANO-SCALE POROUS MEDIA AT SLIP FLOW

Gas flow in micro/nano-scale porous systems is observed in many applications and technologies. Gas dynamics at such small scales differ from conventional fluid dynamics estimations due to rarefaction effects. In the literature, the Knudsen number (Kn) for the characterization of rarefaction effects on permeability is calculated based on a characteristic flow height estimated from the pore size, while the geometric parameters such as pore shape and pore-throat ratios are mostly ignored. Therefore, an accurate characterization of rarefaction effects could not be ascertained. For the first time in literature, a general characterization of gas transport through systems at different porosity and pore throat size values and at different rarefaction levels was obtained using a modified Kn definition. The characteristic height required for an accurate Kn of a porous system is defined using the "equivalent diameter" calculated from the corresponding permeabilities. Pore-level calculations were performed in a wide range of systems while the observed permeability variation by porous parameters was successfully described by an extended volume-averaged model developed as a combination of the Darcy, Kozeny-Carman, and Klinkenberg models. The characterization systematic and volume-averaged model was applied for various cases of (i) two-dimensional porous, (ii) two-dimensional multi- porous, and (iii) three-dimensional complex porous system. For all these systems, the permeability values could be estimated in terms of the geometric parameters of the porous structures and rarefaction levels. In addition, the rarefaction effects on heat convection in metal foams were studied through Darcy to Forchheimer flow regimes using the Kelvin Cell structure. A 60% increase in permeability and a substantial decrease in inertial effects developed due to rarefaction, while Nusselt numbers were found mostly related to Reynolds number. Further, the influence of variation in gas thermophysical properties coupled with rarefaction as a function of increasing gas temperature for high heat flux applications was described. A 40% decrease in hydraulic conductivity for a temperature increase from 300K to 400K is observed, independent from the Kn number.

Keywords: Apparent gas permeability; Rarefaction; Pore connectivity effects; Velocity slip; Equivalent Knudsen number.

ÖZET

KAYMA AKIŞ REJİMİNDE MİKRO/NANO ÖLÇEKLİ GÖZENEKLİ YAPILARDA GAZ TAŞINIMININ SAYISAL OLARAK İNCELENMESİ

Birçok önemli uygulamalarda karşımıza çıkan mikro/nano-ölçek gözenekli sistemlerdeki gaz akışı mevcut geleneksel akışkanlar dinamiği hesaplarından seyrelme etkileri nedeniyle farklılaşmaktadır. Literatürde geçirgenlik üzerindeki seyrelme etkilerinin karakterizasyonunda kullanılan Knudsen sayısı gözenek boyutu cinsinden hesaplanmış, gözenek-boğaz genişliği gibi diğer geometrik parametreler göz ardı edilmiştir. Bu nedenle mikro/nano-ölçek seyrelme etkilerinin doğru bir karakterizasyonu elde edilememiştir. Literatürde ilk kez, faklı gözenek ve gözenek-boğaz genişliğindeki sistemlerde farklı seyrelme seviyelerindeki gaz taşınımın doğru Knudsen tanımı ile genel bir karakterizasyonu elde edilmiştir. Çok farklı akış alanları içeren bir gözenekli sistemin doğru Knudsen sayısını hesaplamak için gerekli karakteristik akış boyutu geçirgenlik kat sayısından hesaplanan bir "eşdeğer çap" tanımı ile sağlanmıştır. Gözenek seviyesi hesaplamaları çok çeşitli sistemlerde uygulanmış ve gözenekli parametrelerle gözlemlenen geçirgenlik değişimi Darcy, Kozeny-Carman ve Klinkenberg modellerinin bir kombinasyonu olarak hacim ortalamalı bir model ile başarıyla tanımlanmıştır. Bu karakterizasyon sistematiği ve geçirgenlik hesaplama modeli (i) iki boyutlu, (ii) çoklu gözenekli ve (iii) üç boyutlu kompleks gözenekli gibi farklı yapılarında uygulanmış ve başarılı sonuçlar elde edilmiştir. Bahsi geçen yapılarda gözenekli sistemin geometrik parametreleri ve seyrelme seviyesi cinsinden geçirgenlik değerleri geliştirilen model ile karakterize edilebilmiştir. Ek olarak konvektif gaz taşınımın seyrelme etkileri Kelvin cell yapısına sahip metal köpükler üzerinde Darcy ile Forchheimer arasındaki rejimlerde hesaplanmıştır. Seyrelme etkileri geçirgenlik kat sayısının 60% artışına ve eylemsizlik etkilerinin azalmasına sebep olurken hesaplanan Nu katsayısının seyrelme etkilerinden bağımsız olarak sadece Reynols sayısı ile ilişkili bulunmuştur. Ayrıca, yüksek ısı akış uygulamaları için gazın termofiziksel özelliklerindeki değişikliğin seyrelme ile birleştiğinde etkisi açıklanmıştır. Kn sayısından bağımsız olarak 300K'dan 400K'ya kadar bir sıcaklık artışı için hidrolik iletkenlikte %40'lık bir azalma gözlemlenmiştir.

Anahtar kelimeler: Gerçek gaz geçirgenliği; Seyrelme etkileri; Gözenek bağlantı etkileri; Hız kayması; Eşdeğer Knudsen sayısı.

TABLE OF CONTENTS

LIST OF FIGURES

Figure **Page**

LIST OF TABLES

CHAPTER 1

INTRODUCTION

Characterization of gas flow behaviors in micro/nano-scale porous media are observed in several industrial and environmental applications. Many promising applications at this level, including membrane filtration[1], oil-gas recovery processes[2], gated/functionalized sensing[3], geologic sequestration of CO_2[4], and various lab-on-a-chip devices[5], require proper flow characterization.

In order to accurately describe transport behavior through micro/nanoscale porous media, non-equilibrium effects should be characterized[6]. The interactions between fluid and wall at micro or nano confinement results in non-equilibrium in fluid dynamics. Such effects are resulted to the failure of classical continuity-based theories which are not able to solve the heat and mass transport. Effects of the non-equilibrium behavior are observed in the near-wall region. A possible solution procedure should be determined according to the extent of this near-wall non-equilibrium region into the entire flow domain.

The micro/nanoscales dynamics developing in the case of a gas flow is comprehensively studied subject because of practical and easy calculation methods available by gas Kinetic Theory (KT) and Molecular Dynamics (MD)[7,8]. Basically, the Knudsen number ($Kn = \lambda / H$) computed as the ratio of mean free path (λ) of gas molecules to the characteristic length of confinement (H, L_c) shows the degree of non-equilibrium gas dynamics. For system sizes larger than 20nm[9], surface force effects are mostly negligible that gas dynamics are governed by so-called rarefaction effects. Four different flow regimes can exist in the system based on Kn calculation which is described below[10]:

I. For $Kn < 0.001$, flow is in the full continuum regime. The continuum and thermodynamic equilibrium assumptions are valid, and the flow can be described by Navier-Stokes (N-S) equations with conventional no-slip boundary conditions.

II. For $0.001 < Kn < 0.1$, flow can be considered as the slip flow. The non-equilibrium effects (slip velocity and temperature jump) dominate near the walls but continuum assumption within the fluid bulk is valid. In other words, the conventional boundary condition, i.e., no slip boundary condition, fails at the walls flow path. Usually,

the slip boundary models are applied to N-S equations to describe the rarefaction effects of this flow regime.

III. For 0.1 < Kn < 10, flow is in the transition region between slip and free molecule flow.

IV. For Kn > 10, the free-molecular regime should be considered. In this regime non-equilibrium effects dominate almost all gas bulk flow. The collisions between the gas molecules and wall surfaces are dominant and the inter- molecular collisions can be ignored. Under such conditions, usually other methods such as molecular dynamic (MD), direct simulation Monte Carlo (DSMC) or solution of linearized Boltzmann equation (LBE) are used to describe the flow at the molecular level.

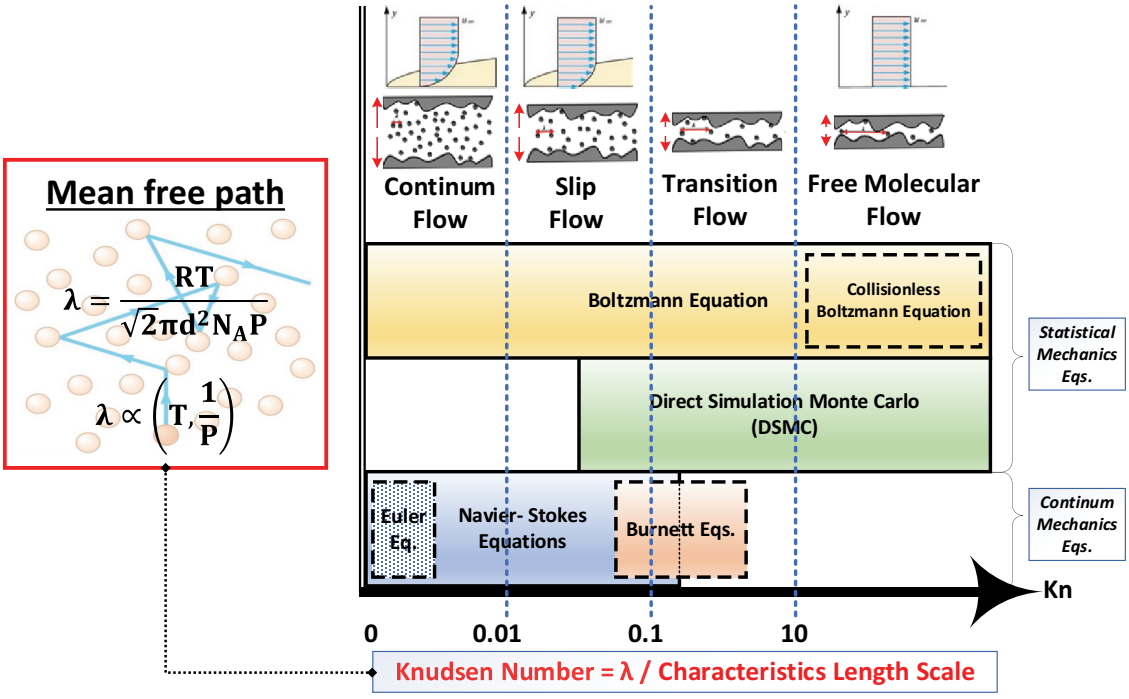

Figure 1.1. Illustration of different gas flow regimes based on Kn number.

At micro/nano scale gas dynamics is a coupled function of pore size and pressure. For example, a 5MPa reservoir pressure inside a 20nm pore or a 0.2MPa reservoir pressure inside a 500nm pore develops flows in the slip flow regime. The correlation between characteristic pore size, mean gas pressure, and the resulting Kn value is described in Figure 1.2. Depending on the flow regime, various forms of Kinetic theory-based solutions provide accurate results. A vast number of existing applications lie in the slip flow regime where the Naiver-Stokes is applicable with an appropriate velocity slip defined on the surface as practiced by many to resolve micro/nano porous transport.

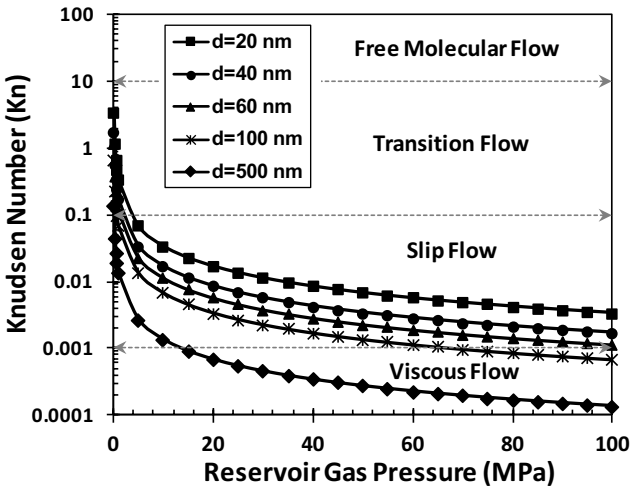

Figure 1.2. Variation of Knudsen Number with Reservoir Gas Pressure[11].

There are two main approaches frequently using in the literature to characterize the transport: Pore-Scale Method (PSM)[12–14] and Volume-Average Method (VAM)[15–17]. PSM yields very sensitive results however it is not an appropriate method for estimating the flow in large scale since every pore needs to be considered for calculations. Thus, VAM is mainly preferred instead of PSM. The application of volume averaging method on continuity, momentum, and energy equations causes appearing of extra terms in corresponding equations. These terms involve macroscopic properties such as permeability, Forchheimer, thermal dispersion, thermal tortuosity, and interfacial convective heat transfer coefficients. There are huge numbers of studies in the literature to specify the macroscopic flow parameters for various porous media[18–22]. The main aims in these studies generally were to understand the effects of the geometrical and/or flow properties such as porosity, Reynolds number, flow direction on the macroscopic transport parameters. Although the effects of many geometrical and flow parameters on macroscopic transport properties were studied and reported, still there are important parameters that have not been considered, such as pore to throat size ratio.

While the characterization of gas dynamics using Kn is simple, describing a characteristic pore size for the complex structures of the porous systems is not trivial. Specific for PSM, almost all of the existing studies use height of the corresponding REV to define the Kn number[23,24]. Such a perspective will result in incorrect Kn values and gas dynamic characterization. In general fluid dynamics, hydraulic diameter (d_h) concept is devoted to estimate an appropriate characteristic flow height for an ambiguous flow shape. Many studies adapted similar d_h calculations to predict an accurate Kn value for porous systems[25]. However, d_h was also incapable of providing a general characterization,

as it cannot consider pore connectivity. Simply, two different pore structures at the same porosity will have the same d_h but can have a different pore size to pore throat size, creating very different flow characteristics. Hence, using d_h will not yield a correct Kn number and characterization of gas dynamics.

1.1. Literature Review

1.1.1. Klinkenberg Theory

Permeability experiments are mostly performed using liquids to keep the experimental setup simple. Assuming incompressible flow, permeability of gas and liquid in a given porous system is the same. However, since the distance of gas molecules is more than the molecular spacing of liquids, such confinement size directly affects gas dynamics. When the spacing becomes comparable with the characteristic confinement size, non-equilibrium gas dynamics develop. For such a case, gas permeability of corresponding material becomes different than its' liquid permeability. The first time this problem was observed and examined by Klinkenberg[26], who proved that non-equilibrium significantly impacts the permeability values. Klinkenberg relates the gas permeability of a material to its liquid permeability as,

$$K_a = K_\infty \left(1 + \frac{b_k}{\bar{P}}\right) \tag{1.1}$$

where K_a is the apparent gas permeability calculated from the intrinsic permeability value (K_∞) as a function of the gas mean pressure ($\bar{P}$) and coefficient b_k is known as the Klinkenberg slip factor or Klinkenberg coefficient. In his original work, the b_k is suggested as,

$$b_k = \bar{P}\frac{4c\lambda}{r} \tag{1.2}$$

where c is a constant approximated to unity, λ is the mean free path of the gas at the mean pressure, and r is the effective pore radius. Equation (1.1) is very practical and easy to use, but the required b_k value approximated by Equation (1.2) is incapable of describing various porous systems. Hence, subsequent researchers mostly focused on developing a better model to calculate the Klinkenberg constant for a general definition of non-

equilibrium effects. First, researchers determined the Klinkenberg slip factor b_k from permeability values estimated from real field results and lab experiments. Alternative to experiments, theoretical calculations of fluid dynamics inside the porous system, namely Pore Scale Methods (PSM), can find permeability directly from numerical solution of gas dynamics in a control volume representing the porous system (REV). Recent studies follow such a systematic approach to estimate the Klinkenberg constant. The most well-known and cited works proposing a Klinkenberg slippage factor are summarized and tabulated in Table 1.1.

The size value of pore throat in porous media is shown by r, which is very difficult to measure exactly for a porous medium. As a result, Heid et al.[27] proposed a power-law relation correlating intrinsic permeability (K_∞) and gas slippage coefficient b_k,

$$b_k = \alpha \left(K_\infty \right)^\beta \tag{1.3}$$

Later Sampath and Keighind[28] proposed another way of representing the correlation using porosity fraction as an additional parameter,

$$b_k = \alpha \left(\frac{K_\infty}{\varepsilon} \right)^\beta \tag{1.4}$$

the α and β constants are determined by the experimental results. To compute the intrinsic permeability the interception of straight-line on apparent permeability of Klinkenberg plot with respect to adverse mean gas pressure is used. The above two forms of relation are frequently used in the literature by many researchers to investigate gas permeability in rock, coal, sandstone, shale, etc. Some of these works which determined the Klinkenberg slippage factor numerically or by experimental methods are summarized and tabulated in Table 1.1.

Florence et al.[29] applied a microflow model using a second-order coefficient for slippage of gas to find permeability for low and very-low permeability core samples. C. Jones[30] developed an instrument and theory which calculates Forchheimer coefficient, Klinkenberg permeability and Klinkenberg constant for more than 100 core plugs in an unsteady-state condition. Yu-Shu Wu[31] used analytical methods and developed a new model for the Klinkenberg constant, which can be used for transient and steady-state gas flow through various geometries in porous media. Tanikawa et al.[32] proposed a correlation based on Heid et al. and found the relationship between *b* parameter and water permeability. They found that the permeability of nitrogen gas was 2-10 times higher than water. Darabi et al.[33] model, known as apparent permeability function (APF) describes

gas transport inside an inter-connected shape of micro/nanopores with tortuosity effect. Their APF models that are valid for a large scale of Knudsen numbers can be used in slip flow and Knudsen diffusion. QingBao & XiaoSong[34] results recommended using a power-law relationship for the Klinkenberg constant. They concluded that the Klinkenberg effect on the fault rocks, both breccia, and gouge, is uniform. Civan[35] proposed an equation for Klinkenberg gas slippage factor to describe the gas flow in fine porous medium with respect to porosity, tortuosity and intrinsic (liquid) permeability. He demonstrated the effect of these parameters on rarefaction, apparent gas permeability, and Klinkenberg slippage factor by verifying the proposed correlation with experimental data. In micro-porous media and slip flow regime Zheng et al.[36] proposed a model based on fractal theory to describe gas slippage factor for minor permeability values. They predicted gas slippage factor as a function of geometrical parameters of porous medium which make the results of gas slippage coefficient similar to experimental data trend. Moghadam & Chalaturnyk[37] paper suggests a new analytical expression to predict and explain the influence of gas slippage on transport. Their equation is simplified form of Klinkenberg's proposed model to estimate low permeable porous medium. Wang et al.[38] proposed two modified models to predict coal gas permeability with matchstick hypothesis model. They showed that under constant effective stress, Klinkenberg coefficient changes is in a significant range. Also, the result of second model was verified by the field data which assumed of uniaxial strain and non-variable high stress during the coalbed methane (CBM) recovery. Hooman et al.[39] obtained Klinkenberg's constant with respect to porosity, intrinsic permeability and gas properties. Their results were compared to existing experimental data in the literature and observed to be in good agreement. Li et al.[40] offered analytical model including geometrical parameters of porous media such as pore radius, porosity and fractal dimensions with gas property as a function of Klinkenberg. The model was obtained with respect to fractal capillary and microflow models to predict gas permeability. Zhu et al.[41] used numerical simulation to estimate the gas transport with Klinkenberg effect for solid deformation and gas transport in coal grains, and then verified analytical solutions. Tao et al.[42] suggested a coal permeability model take into consideration of gas stream in isotropic components with Klinkenberg model. The proposed model is based on strain effects while the Klinkenberg factor is included as a dynamic parameter (not empirical). In this way, the model becomes only function of deformation and changes of effective stress in the coal bed. Li & S.Sultan[43] studied the Klinkenberg slippage effect by applying Monte Carlo molecular simulation

method at pore-scale level. They used data fitting formula to increase the accuracy of their equation in the permeability computation, making the results of their proposed model consistent with the experimental observations of real rock samples.

Table 1.1. Proposed models for the calculation of Klinkenberg constant in literature.

Author	Correlation	Comments/Units
Klinkenberg (1941)	$b_K = \frac{4c\lambda\bar{P}}{r}$, c ≈ 1	Field Data
Heid et al. (1950)	$b_K = 0.777(K_\infty)^{-0.39}$	Field Data
Florence et al. (2007)	$b_K = \beta(K_\infty / \varnothing)^{-0.5}$	Field Data
Stanley C. Jones (1972)	$b(psi) = 6.9(K_l)^{-0.36}$	Experimental Study
Sampath and Keighin (1982)	$b_K = 0.0955(K_\infty / \varepsilon)^{-0.53}$	Experimental Study
Yu-Shu Wu (1998)	$b_K = -\frac{P_n + P_i}{2} - \frac{\mu q_m}{4\pi h k_\infty \beta (P_n + P_i)} Ei\left(\frac{r_w^2}{4\alpha t_n}\right)$	Experimental Study
Tanikawa et al. (2009)	$b_K = (0.15 \pm 0.06)(K_\infty)^{(-0.37 \pm 0.038)}$	Experimental Study
Darabi et al. (2012)	$b_K = \left(\frac{8\pi RT}{M}\right)^{0.5} \frac{\mu}{R_{avg}}\left(\frac{2}{\alpha} - 1\right)$	Experimental Study
QingBao & XiaoSong (2014)	$b_K = 0.2 \times 10^{-3} K_l^{-0.557}$	Experimental Study
Civan (2010)	$b_K = 0.0094(K_\infty / \varepsilon)^{-0.5}$	Analytical Study
Zheng et al. (2013)	$b = \frac{8\mu(3 + D_t - D_p)}{\sqrt{32\bar{\tau}\left(4 - \frac{D_p}{2} - D_p\right)(1-\varnothing)(2 + D_t - D_p)}} \sqrt{\frac{\pi R_g T}{2M}} \left(\frac{K_\infty}{\varnothing}\right)^{-1/2}$	Analytical Study
Moghadam & Chalaturnyk (2014)	$b_K = b - \frac{a}{\bar{P}}$, $m = c\mu\sqrt{\frac{\pi RT}{2M}}$ $b = \frac{4m}{r_0}$, $a = \frac{b^2}{4}$	Analytical Study
Wang et al. (2014)	Constant effective Stress $b_{ME} = \frac{\varnothing_0}{\varnothing_0 - \varepsilon_L \frac{P}{P_L + P}} \cdot \frac{\mu_{Me}}{\mu_{He}} \sqrt{\frac{M_{Me}}{M_{He}} b_{He}}$ For coal: $b = \frac{32c\mu}{a\varnothing}\sqrt{\frac{2RT}{\pi M}}$	Analytical Study (Model verified by field data)
Hooman et al. (2014)	$b_K = \frac{2-\sigma}{\sigma} \frac{7.9\varepsilon}{\sqrt{2\Gamma(1-\varepsilon)}} \frac{k_B T}{\pi d^2} \frac{1}{\sqrt{K_{no-slip}}}$ $K_{no-slip} = \frac{\varepsilon^2 D_h^2}{\Gamma(1-\varepsilon)}$ and $D_h = \frac{2s}{\tan\left(\frac{\pi}{m}\right)}$	Analytical Study (Model verified by experimental data from literature)

(cont. on next page)

Table 1.1. (cont.)

Li et al. (2016)	$b_K = \frac{\left(3+D_T-D_f\right)}{\left(2+D_T-D_f\right)}\left(\frac{32\pi R_g T}{M}\right)^{1/2}\left(\frac{\varnothing}{1-\varnothing}\right)^{1/2}$	Analytical and Numerical Study (validate by experimental)
Zhu et al. (2007)	$b=\alpha_k(K_\infty)^{-0.36}$	$\alpha_k = 0.251$ (Ref 3 JonesFo 1980) Numerical Study
Tao et al. (2016)	Permeability module coupled to the Klinkenberg effect	Numerical and Experimental Study
Li & S.Sultan (2017)	$b_K = 18.5\times10^4$ Pa	Numerical Study

However, all the proposed models still could not provide a general characterization and remain mostly case specific. Regardless of the vast number of studies, there is still a need for improved fundamental understanding and proper quantification.

1.1.2. Pore connectivity effect

Determination of permeability, only by considering the porosity itself, could be resulted in misleading evaluations. Basically, if the pore throat structures are highly tight, then flowing of the fluid through the throats becomes very difficult due to the surface tension forces (Serra, 1984)[44]. In such cases, permeability estimation by measuring porosity does not lead to accurate results. Hence, to prevent any incorrect permeability predictions other geometrical parameters such as pore throat size should also be considered together with porosity. Micro/nanoscale porous media have rather complicated and tight porous structures. Particularly, for the unconventional reservoirs whose large pore dimensions and relatively small throat sizes make them different from the conventional ones, the ratio between pore and throat sizes is investigated in detail by several researchers, and some attempts have been made to define pore to throat size ratio as a function of porosity. For instance, Huang et al.[45] investigated the effects of pore throat structure on gas permeability in tight sand reservoir using helium-measured porosity, pulse decay permeability, casting thin sections, scanning electron microscopy (SEM), nuclear magnetic resonance (NMR), and constant-rate mercury injection. They obtained those large throats result in larger throat radius and higher pore connectivity, resulted to higher permeability. In the work of Rezaee et al.[46] the relationship between permeability,

porosity and pore throat size were examined with neural networks. The study showed that pore throat radius at 50% mercury saturation yields the best correlation coefficient for permeability, porosity, and pore throat radii for carbonates rocks. Glover and Déry[47] investigated the effect of different grain size and pore throat size on the streaming potential coupling coefficient of porous granular media by theoretical and experimental methods. They developed a new equation which relates the variation of streaming potential coupling coefficient with pore diameter and pore throat diameter. With the proposed equation the streaming potential coupling coefficient of a reservoir rock can be evaluated as a function of grain size and pore throat size. Jin et al.[48] conducted a study to understand water flow mechanism in nanochannels by using LBM. They showed that both pore-throat ratio and throat length can greatly affect water flow in nanochannels while the effect of interfacial layer on water flow in nanochannels becomes more obvious with increasing pore-throat ratio and throat length. Zhang et al.[49] presents an experimental study of microscopic pore throat structure characteristics of tight sandstone reservoirs. They found that pore size distribution of tight sandstone reservoirs ranges from 2 nm to 500 mm distribution. Pore throat analysis results showed that pore-throat size mainly control permeability stress sensitivity in tight sandstone reservoirs, which can affect well oil production. In the study of Gao et al.[50], pore and throat parameters in tight oil reservoir were quantitatively measured using constant mercury intrusion technique. They found that the average throat radius, main flow throat radius and throat quantity were independent from the porosity but show a good relationship with permeability. The low oil production in tight oil reservoir should be linked to the existence of larger pore throat ratio. Dianshi et al.[51] measured the pore to throat size ratio in the range of 7.5-64 by using the rate-controlled porosimeter and nuclear magnetic resonance technique for the tight sandstone. Cao et al.[52] performed mercury injection capillary pressure (MICP) and N_2 gas adsorption (N_2GA) to determine pore structure of Chang-7 tight sandstone. Their measurement yielded pore-to-throat size ratio results between 2 and 10.

1.2. Objective of the Thesis

The present study performs pore-scale analyses of gas dynamics and calculates volume-averaged properties of the corresponding micro/nano-scale porous systems.

Kozeny-Carman theory will be employed to model equilibrium gas dynamics, while nonequilibrium will be incorporated using Klinkenberg theory in the slip flow regime. For such a case, Klinkenberg constants will be described based on the pore properties (and H_{eq} is calculated from Hagen-Poiseuille and Darcy formulations for the first time in the literature.

This dissertation has been divided into six chapters. In the first chapter, a brief introduction of gas flow in slip region is presented. Next, Klinkenberg's theory is introduced, and a short literature review on this theory and the effect of pore connectivity is given.

In Chapter 2, basic transport concepts of porous media and the theoretical background of pore-scale and volume-average methods are given. The definition of permeability based on Darcy and Forchheimer's law is given. Lastly, the representative porous medium is defined, and accordingly the governing equations and boundary conditions employed on this system are given.

In Chapter 3, an extended Kozeny-Carman Klinkenberg model is proposed for the homogenous porous medium. The correct form of Kn number is proposed to include all the geometrical properties into one linear relation. Finally, the empirical model to predict permeability with high accuracy is proposed.

In Chapter 4, a two-dimensional system with an intraparticle porous medium is considered as the representative domain. The results were compared with mono-scale two-dimensional flow. It has been shown that the Kn definition based on permeability calculation is also valid for this type of structure.

Chapter 5 consists of the numerical methods used for determination of permeability in three-dimensional flow. Similar to previous sections, computational details and the results are presented in this chapter as well.

Finally, in Chapter 6, a pressure-driven gas flow through metal foams with Kelvin cell geometry at different rarefaction levels is studied. Permeability and convective heat transfer coefficient were calculated, and the required discussions on the results were made. At the final step, a mathematical relation is proposed to calculate the Nu number with high accuracy.

CHAPTER 2

THEORETICAL BACKGROUND AND MATHEMATICAL MODEL

Characterization of transport in porous medium is a complicated task since existence of heterogeneities within the porous structures makes the transport phenomena estimation difficult. To overcome the difficulties of characterizing flow in porous medium more appropriate techniques are required to investigate and solve the transport in porous media. .Mainly two major approaches known as microscopic and macroscopic approaches[53,54] are addressed in the literature. By selecting the proper approach one can determine the velocity, pressure, and temperature distribution of porous medium more easily.

2.1. Pore Scale Method

In an open porous medium, where the void space and solid particles are interconnected, flow takes place in the pores (or voids) between the particles. In microscopic approach methodology, three-dimensional form of governing equations is solved in the voids between solid structures. This method generates an accurate result for velocity, pressure, and temperature distributions. For a Newtonian fluid under incompressible flow conditions with constant thermo-physical properties, conservation of mass, momentum, and energy for fluid phase can be written as below:

$$\nabla.\vec{V} = 0 \tag{2.1}$$

$$\rho_f \frac{D\vec{V}}{Dt} = -\nabla p + \mu_f \nabla^2 \vec{V} + \vec{F} \tag{2.2}$$

$$\left(\rho c_p\right)_f \left[\frac{\partial T_f}{\partial t} + \vec{V}.\nabla T_f\right] = k_f \left(\nabla^2 T_f\right) \tag{2.3}$$

Since the microscopic approach study the fluid motions in the pores between particles entirely, it provides very sensitive results. However, application of such model

for porous medium with disordered or random geometry is very difficult and time consuming.

2.2. Volume Average Method

Since the application of microscopic methods (or pore-scale method) in a porous medium consisting of many pores is very complex, other practical solutions were described in the literature. Such methods as macroscopic approaches are frequently used to analyze transport through porous medium by volume averaging. In this technique, the governing equations are solved with respect to representative elementary volume of porous structure. Thereafter, volume-averaged governing equations (i.e., macroscopic governing equations) are determined by excluding the discontinuity of any phase. Due to integration, additional terms appear in governing equations that involves volume averaged transport parameters (i.e., macroscopic transport parameters). As a result of this, the obtained governing equations can be estimated for all single-phase space.

Application of VAM should start with a selection of representative elementary volume (REV)[55,56]. A control volume within porous media should be taken larger than the microscopic characteristic length and smaller than the control volume, as shown in Figure 2.1.

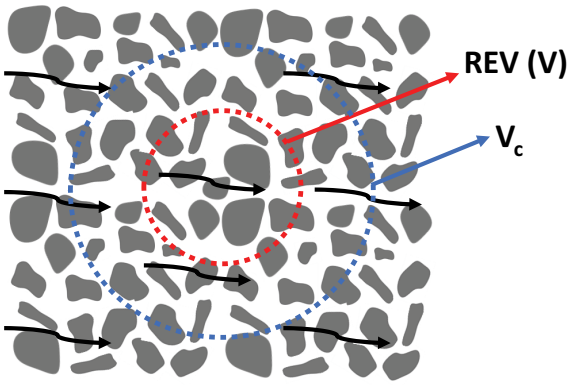

Figure 2.1. A microscopic control volume in a porous medium.

Applying volume average to any quantity over a control volume is computed as follows:

$$\langle \varphi \rangle = \frac{1}{V} \int_V \varphi \, dV \tag{2.4}$$

where V is the volume of a corresponding control volume. For instance, by using Equation (2.4) the macroscopic velocity in x direction (u velocity) is described as below,

$$\langle \vec{u} \rangle = \frac{1}{V} \int_V \vec{u}\, dV \tag{2.5}$$

If an average value of any parameter for one phase is required intrinsic averaging is employed. For example, the average velocity of fluid phase, which is called pore or interfacial velocity, can be calculated from (2.6),

$$\langle \vec{u} \rangle^f = \frac{1}{V_f} \int_{V_f} \vec{u}\, dV \tag{2.6}$$

where V_f is pore volume. The relation between macroscopic and pore velocities is shown by Equation (2.7) which is known as Dupuit-Forchheimer[57] relation,

$$\langle u \rangle^f = \langle u \rangle / \varepsilon \tag{2.7}$$

2.2.1. Darcy-Forchheimer Theory

In 1856 Henry Darcy[58] found that the macroscopic (Darcian) fluid velocity through a column of sand beds is proportional to the pressure gradient and adversely proportional to the viscosity of fluid. He found that mass flow rate and pressure gradient are linearly coupled parameters with another parameter, which was later called as permeability. This relation is named as Darcy's Law, and in one-dimensional form is shown by Equation (2.8),

$$\langle u_f \rangle = -\frac{K_{xx}}{\mu} \frac{d\langle p \rangle^f}{dx} \tag{2.8}$$

in which K is known as permeability. The permeability is known as tensor quantity that the terms in diagonal row represent the permeability of the porous medium in principal directions. Permeability refers to the flow resistance inside porous medium. It depends on the micro-structure of the solid phase and is independent of the properties of the fluid[59]. Darcy's Law can be accurately utilized to attain average velocity in a porous medium for low Reynolds number flows (Re < 10) since it states a relation between viscous and pressure forces.

Starting with Darcy's definition, different techniques have been employed to calculate the permeability of porous medium. For instance, at a higher Reynolds number, an additional quadratic term that includes inertial effects was suggested by Dupuit[60] and Forchheimer[61]. This equation is called as Forchheimer extended Darcy's Law[62,63], and in one-dimensional form is calculated by the following equation:

$$-\frac{d\langle p\rangle^f}{dx}=\frac{\mu_f}{K}\langle u\rangle+\frac{C}{K^{1/2}}\rho_f\left(\langle u\rangle\right)^2 \tag{2.9}$$

where C is the Forchheimer coefficient. The first term on the right-hand side represents the frictional drag (Darcy term), while the second term (Forchheimer) refers to the drag. Hence, in order to estimate macroscopic velocity correctly, permeability and Forchheimer coefficients should be known exactly.

2.2.2. Kozeny-Carman Equation

Generally, porous material's permeability is measured by experiments. Modeling the variation of permeability by porous characteristics has been attempted by many[29,64–66]. The most well-known one, the Kozeny-Carman theory[67], aims to calculate the permeability as a function of porosity (ε) and hydraulic diameter (d_h) of the corresponding porous system with an empirically determined constant C_{KC}.

As a starting point, Kozeny performed his study for a system with a bundle of capillary tubes of an equal radius. First, the mean velocity for Hagen-Poiseuille flow in a channel with a diameter of d_t was calculated (Equation (2.10)):

$$\langle u\rangle^f=-\frac{1}{32\mu}\frac{d\langle p\rangle^f}{dx}d_t^2 \tag{2.10}$$

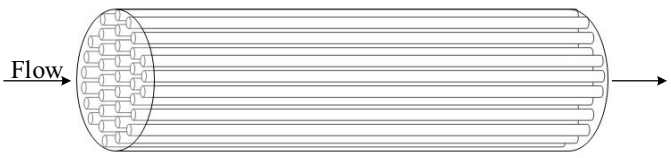

Figure 2.2. Flow through a bundle of capillary tubes.

Later, Kozeny integrated Hagen-Poiseuille equation and Darcy's theory together with the idea of tortuosity and proposed the following equation to calculate the permeability:

$$K = \frac{d_t^2 \varepsilon}{32\tau} \tag{2.11}$$

where the term τ is tortuosity[68] which can be explained as the ratio between real length of flow path in the porous medium to the length of flow path without porous medium (i.e., in clear fluid).

Kozeny's proposed equation for the estimation of permeability was then revised by Carman. Later called Kozeny-Carman equation, it has been widely used in the literature for laminar flow. Kozeny-Carman equation predicts the intrinsic permeability of media with high accuracy. For the packed bed of spheres, the relation is given as:

$$K = \frac{d_h^2 \varepsilon}{16 C_{KC}} \tag{2.12}$$

here, d_h is the pore hydraulic diameter, and A_0 is the ratio of the fluid-solid interfacial area to the solid volume. The term denoted as C_{KC} in equation (2.12) is called Kozeny-Carman constant, that add the effects of the flow path, pore structure, and connectivity (i.e., tortuosity and shape effects).

Although the KC equation is widely accepted and used extensively, the Kozeny-Carman constant should be properly determined. Since, this equation is a semi-empirical relation, and the KC constant is an empirical constant, which was proved to be not a specified constant (varied value for different media). Accurate evaluation of C_{KC} is an important aspect for applying KC equation to different transport process. There are many studies in the literature dedicated to the numerical and experimental determination of C_{KC}. In the original study of Carman, C_{KC} was given as 4.8 ± 0.3 for packed beds with homogenous spheres and is usually taken to be equal to 5[69]. There are many other studies from the literature also suggesting a constant value for C_{KC}[70–75]. For instance, different C_{KC} values were found as 2.79, 3.62, and 3.80 for the different sphere radius of 2.5, 3.5, and 4.5, respectively, while the corresponding permeability values were validated by the experimental measurements[76]. Similarly, different C_{KC} values were calculated at different porosity values for the staggered arranged porous systems; an inverse relationship between C_{KC} and porosity varying between 0.4 and 0.88 was observed[77]. The literature related to the field of transport in porous media and examination of Kozeny–Carman equation is vast, and here only some of representative one was presented. Details and various forms of proposed models for C_{KC} can be found elsewhere[78–82].

2.3. Representative Porous System

Porosity and pore to throat size ratio are frequently used to quantify the structure of the porous medium. The voids of the porous media may be connected to each other (open-cell porous media) or may not have any connection with each other (closed-cell porous media). Generally, the thermal and hydrodynamic behavior of flow is investigated in open-cell porous media. For this reason, porosity (ε) which is the ratio of void volume with respect to total volume of the porous media is frequently used.

$$\varepsilon = \frac{Void\ volume}{Total\ volume} \tag{2.13}$$

In order to establish a given porous medium's properties, Representative Elementary Volume (REV) concept is commonly employed in the literature which is shown in Figure 2.3 (b). In such cases, the volume over which a measurement is performed yield a value, representative of the whole system. Most of explanations related to flow resistance in porous media are concerned that pores and fractures can be simplified into regular models, such as a spherical, capillary tube, matchstick, and cube model. However, the ideal square model is accepted by many researchers[20,38,83,84].

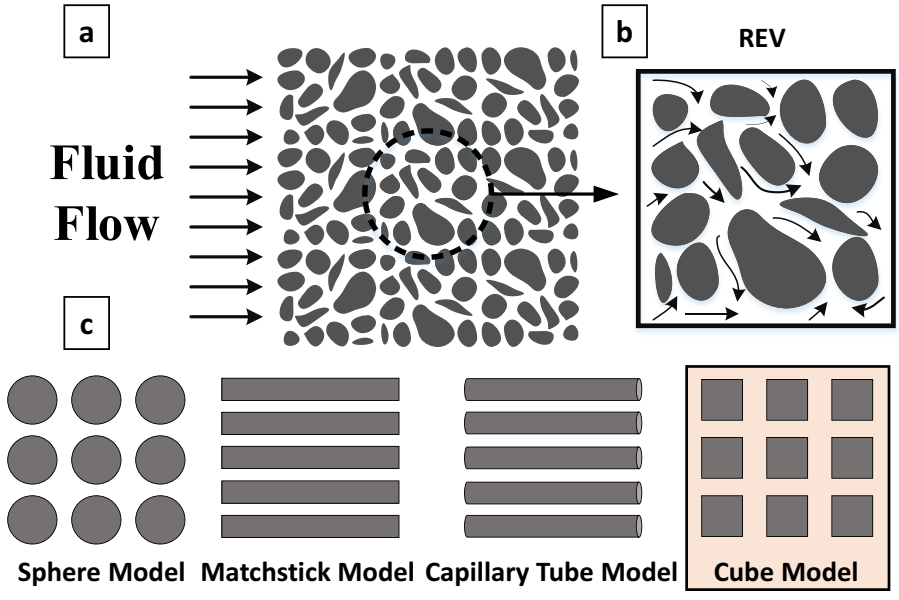

Figure 2.3. a) The illustration of a porous medium, b) Representative Elementary Volume (REV) c) Different REV Models.

As discussed earlier, the structure and array of a random porous medium cannot be considered by porosity variations only. Changes in grain shape, particle distribution,

and size alter the connectivity and tortuosity of the pore space, and therefore, the collective behavior of porous medium. In this study, pore connectivity (R_{pt}) of the REV presented in the cubic model as shown in Figure 2.4 is calculated as:

$$R_{pt} = \frac{Pore\,size}{Throat\,size} = \frac{H_{Darcy}}{a} \tag{2.14}$$

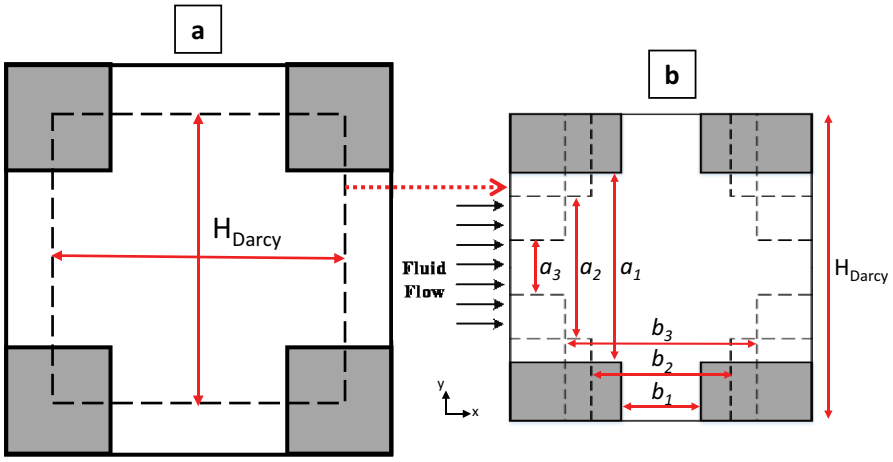

Figure 2.4. a) Representation of a porous system and b) throat size (a) variation at a given pore size (H_{Darcy}) and porosity (ε).

Here, a shows the throat size, which can be changeable. Therefore, R_{pt} can obtain different values.

2.4. Governing Equations and Boundary Conditions

Permeability of considered porous media can be evaluated by investigating the microscopic governing equations. Velocity, pressure, and temperature distributions in the pores can be obtained via the solution of continuity, momentum, and energy equations, while slip velocity and temperature jump were applied on solid surfaces with a unity momentum accommodation coefficient, assuming diffuse reflections.

For the incompressible and steady flow assumptions, the equations and corresponding boundary conditions required to solve the transport in the rectangular coordinates can be written as follows:

$$\nabla.\vec{V} = 0 \tag{2.15}$$

$$\rho\left(\vec{V}.\nabla\vec{V}\right)=-\nabla P+\mu\left(\nabla^2\vec{V}\right) \tag{2.16}$$

$$\left(\rho c_p\right)_f\left(\vec{V}.\nabla T\right)=k_f\left(\nabla^2 T\right) \tag{2.17}$$

$$\overrightarrow{V_s}=-\frac{2-\sigma_m}{\sigma_m}\lambda\frac{\partial\vec{V}}{\partial n}\Big|_w \tag{2.18}$$

$$T_f-T_w=-\frac{2-\sigma_t}{\sigma_t}\frac{2\gamma}{\gamma+1}\frac{\lambda}{\Pr}\frac{\partial T}{\partial n}\Big|_w \tag{2.19}$$

For fully developed velocity profiles in the main flow direction (x+) through the REV, the Darcy velocity and pressure gradient is calculated by the following relation:

$$\langle u\rangle^f=\frac{1}{H_{Darcy}^2}\int_0^{H_{Darcy}}\int_0^{H_{Darcy}}u\,dx\,dy \tag{2.20}$$

$$\frac{d\langle p\rangle^f}{dx}=-\frac{1}{H_{Darcy}^2}\left[\int_0^{H_{Darcy}}p\big|_{x=0}-p\big|_{x=H_{Darcy}}\,dy\right] \tag{2.21}$$

Permeability is a tensor quantity and with respect to Darcy's Law for a two-dimensional flow in Cartesian coordinate can be expressed as:

$$\begin{pmatrix}\langle u\rangle\\ \langle v\rangle\end{pmatrix}=\frac{1}{\mu}\begin{pmatrix}K_{xx} & K_{yx}\\ K_{xy} & K_{yy}\end{pmatrix}\begin{pmatrix}\frac{\partial p}{\partial x}\\ \frac{\partial p}{\partial y}\end{pmatrix} \tag{2.22}$$

where K_{xx}, K_{yx}, K_{xy} and K_{yy} are components of permeability tensor. In this study, the permeability is computed solely in one direction (x+ or z+) since the structure of considered porous medium is symmetrical in all directions. The permeability is calculated with respect to velocity and pressure fields by solving continuity and momentum equations. Darcy Law can also be converted into the non-dimensional form[18] as follows:

$$\Pi=\Lambda+\Gamma\,\mathrm{Re} \tag{2.23}$$

where the corresponding non-dimensional parameters are,

$$\Pi=\frac{L^2}{\langle V\rangle\mu}\frac{\Delta P}{L},\quad \Lambda=\frac{L^2}{K},\quad \Gamma=C_F\sqrt{\left(\frac{L^2}{K}\right)} \tag{2.24}$$

The left-hand side of Equation (2.23) represents the macroscopic pressure drop, while the right-hand side is the reciprocal of the dimensionless permeability. It is clear

that there is a linear relationship between the inverse of the non-dimensional permeability and pressure drop.

The heat transfer between the solid surfaces and the fluid was calculated using the interfacial convective heat transfer concept. The convective heat transfer coefficient was calculated based on the difference between the surface average temperature of solid and the upstream inlet temperature of fluid (T_{in}) as:

$$h = \frac{q_w}{\langle T_w \rangle - T_{in}} \tag{2.25}$$

Characterization of convection based on the upstream inlet temperature of fluid has been found useful for practical applications with a given inlet fluid temperature and frequently utilized by literature[85,86,87]. Correspondingly, the Nusselt (Nu), Reynolds (Re), and Knudsen (Kn) numbers are calculated as follows:

$$\mathrm{Nu} = \frac{hL}{k_f} \tag{2.26}$$

$$\mathrm{Re} = \frac{\rho \langle \vec{V} \rangle L}{\mu} \tag{2.27}$$

$$\mathrm{Kn} = \frac{\lambda}{L} \tag{2.28}$$

L is the characteristic length scale which in this study, the REV dimension (H_{Darcy} or L_c) is used to define the corresponding dimensionless parameters.

CHAPTER 3

KOZENY-CARMAN-KLINKENBERG MODEL FOR GAS PERMEABILITY IN MICRO/NANO-SCALE POROUS MEDIA

Volume Average Methods (VAM) are frequently used to describe the transport in porous systems composed of complex flow patterns based on permeability from a more superficial perspective. Permeability is a material property usually determined through experiments and/or pore level fluid dynamic analysis. Due to the limited availability of permeability, there are numerous modeling attempts to provide simpler empirical prediction tools correlating permeability with the porous system parameters. Various forms of extended Kozeny-Carman (KC) models have created successful results as presented in literature[80–82]. However, these models fail to describe gas transport through micro/nano-scale systems. Unlike liquid flows, with decreasing system size, non-continuum effects develop in gas dynamics due to (i) molecular surface force field and (ii) rarefaction. While the first one is negligible mainly for confinement sizes larger than 20 nm, the latter is dominant when the surface-gas collisions become comparable to gas-gas collisions in case of low gas pressures and/or small confinements[9,88–91]. Characterized by the Knudsen number ($Kn = \lambda / H$), rarefaction effects result in the divergence of gas permeability from its classical literature values. This discrepancy was first observed by Klinkenberg and later studied by many others as a function of Kn in various forms. Although many of these studies have been found accurate at various rarefaction levels, there is a discrepancy in the definition of the Kn in a porous system. Most of these studies employed characteristic height definition from Darcy, while some used classical hydraulic diameter calculations; neither can characterize a complex porous network consisting of pore throats and pore voids in between.

Alternatively, a characteristic flow dimension can be defined by calculating the size of a regularly placed bundle of tubes or plates, allowing an equivalent flow rate at the corresponding pressure gradient. Called as equivalent H (H_{eq}), this was first defined by Kozeny and Carman decades ago but did not grab any attention until its capability to directly represent flow characteristics. However, there is still open discussion about such a concept since the calculation of H_{eq} requires the permeability value of the corresponding

porous system, which is unknown and expected to be estimated based on the H_{eq} in the first place. For such a case, modeling gas permeability based on the Kn number calculated from H_{eq} is not a trivial task.

In this part of the study, pore-scale analyses of gas dynamics were performed to calculate volume-averaged properties of the corresponding micro/nano-scale porous systems. The Kozeny-Carman theory will be employed to model equilibrium gas dynamics, while non-equilibrium will be incorporated using Klinkenberg's theory in the slip flow regime. For such a case, Klinkenberg constants will be described based on the pore properties (porosity and pore connectivity), and H_{eq} is calculated from Hagen-Poiseuille and Darcy formulations first time in literature[92].

3.1. Simulation Details

A porous medium consisting of solids and voids is considered by a representative volume, as shown in Figure 3.1. The size of REV is defined as H_{Darcy} while the size of square solid parts is denoted as D. The ratio of pore size (H_{Darcy}) to throat size between solid parts (a) is given as R_{pt} (H_{Darcy}/a), defining the pore connectivity inside the REV.

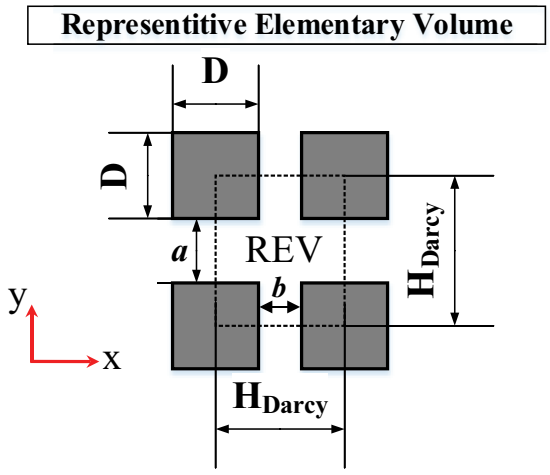

Figure 3.1. Representation of elementary volume for calculation of transport properties.

Air flows through the porous media with a dynamic viscosity equal to 18.21×10^{-6} kg/ms. For different rarefaction levels, air density was varied to obtain different Kn values. Low Re flows were studied to remain in the Darcy flow region with negligible inertial effects. Steady and incompressible form of flow is considered in the voids between the particles. Air is assumed to have constant thermo-physical properties. Steady

forms of the continuity and momentum equations given in Equations (2.15), (2.16), and (2.17) are solved to determine the velocity and pressure fields for the fluid flow using the Fluent finite volume code. Symmetry boundary conditions were considered on top and bottom, and periodicity conditions were applied on left and right boundaries of REV. Slip velocity given in Equations (2.18) and (2.19) were applied on solid surfaces with a unity momentum accommodation coefficient, assuming diffuse reflections.

The validation of the numerical procedure is performed by comparing the result with the literature. As shown in Figure 3.2, there is a good agreement between the computational result for dimensionless pressure drop and dimensionless permeability (Darcy number) between the present work and selected studies in the literature.

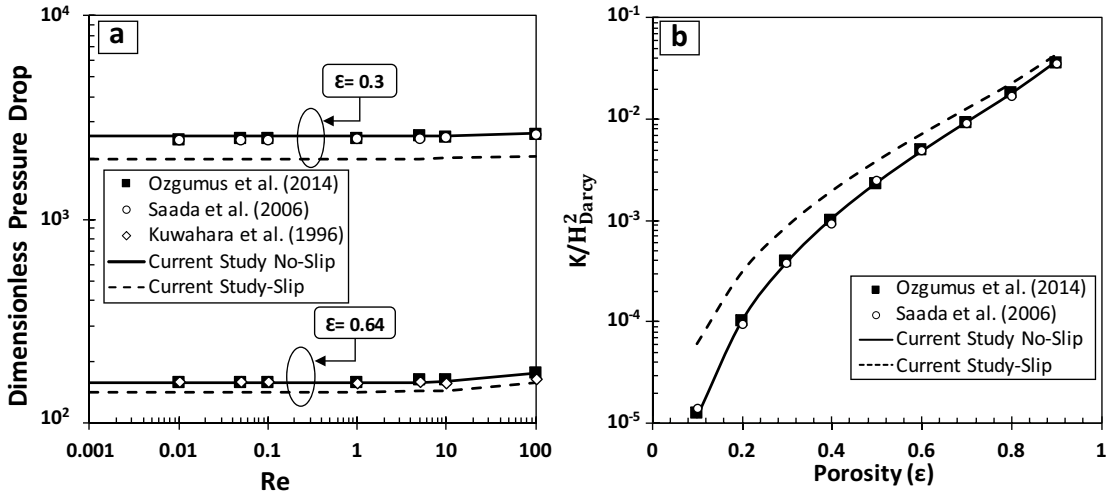

Figure 3.2. (a) Variation of dimensionless pressure drop by increasing Re and (b) resulted permeability values at different porosities. Current results were compared with the values from the literature[59,93,94].

In order to calculate the numerical results with high accuracy, the mesh independency test is performed to discover the optimum grid size for the present study. Several mesh sizes were employed, through which optimum mesh sizes were selected when the error between consecutive mesh results becomes negligible. As shown in Figure 3.3, it has been found that the results converged and stopped changing at the mesh density of 2.3×10^{11} # nodes per m^2, which was selected to be used for all computations in this study. All results are evaluated with Re less than 1 in Darcy's Law applicable range, where a linear relation between non-dimensional pressure drop and inverse of non-dimensional permeability value develops. Typically, any flow with a Reynolds number less than unity is clearly in laminar region. Moreover, experimental tests have shown that flow regimes with Reynolds numbers up to 10 may still be Darcian.

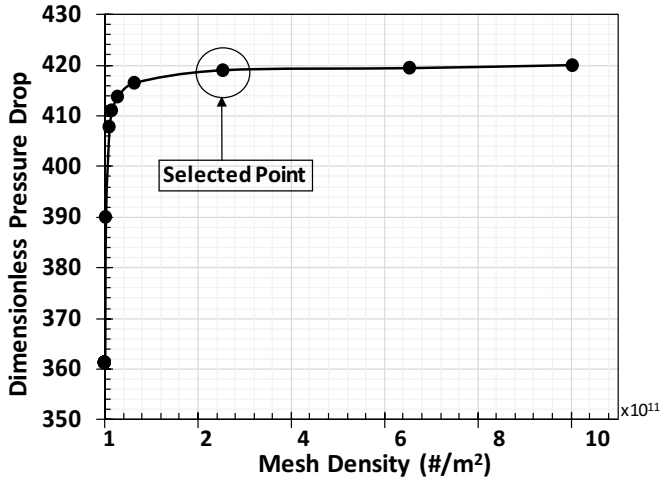

Figure 3.3. Evaluated pressure drop values with different mesh densities.

3.2. Results and Discussions

The study was initiated by calculating permeability values at different porosities, pore to throat size ratios, and rarefaction levels. Results normalized with the area of REV (H^2_{Darcy}) were given in Figure 3.4(a). Depending on the porosity, R_{pt} varies between 2 and 11. At a constant R_{pt}, throat size denoted by *a* was kept constant while different porosities were obtained by varying connectivity size *b*.

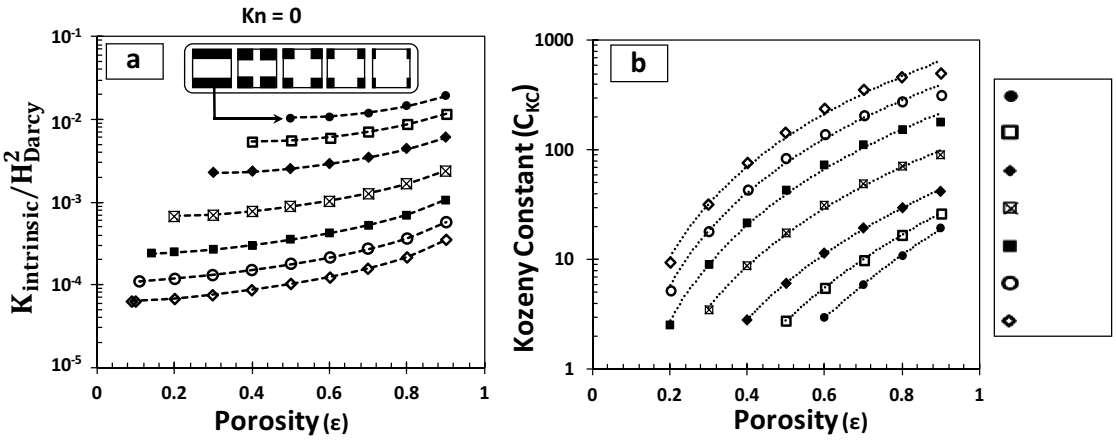

Figure 3.4. (a) Variations of permeability by porosity at different pore to throat size ratio values. (b) Kozeny-Carman constants calculated for the corresponding intrinsic permeability values.

As illustrated in the inset figure of Figure 3.4(a), low R_{pt} cases cannot go below certain porosity values that possible porosity range for each R_{pt} is listed in Table 3.1. The lowest porosity value for each R_{pt} represents the case where *b* becomes zero and REV

becomes a straight channel. Overall, a decrease of R_{pt} increases the permeability due to the decreased tortuosity effects. At a constant R_{pt}, permeability increases by the increase in porosity.

Table 3.1. Lower and upper limits of porosity values at a certain pore to throat size ratio.

Pore to throat size ratio (R_{pt})	Porosity range
11	0.09-0.9
9	0.11-0.9
7	0.14-0.9
5	0.2-0.9
3.33	0.3-0.9
2.5	0.4-0.9
2	0.5-0.9

Next, Kozeny-Carman's theory was used to devise a model to predict the calculated no-slip permeabilities, so-called intrinsic permeability, or liquid permeability. Kozeny-Carman equation relating permeability to porosity (ε) and hydraulic diameter (d_h) is given in Equation (3.1) as,

$$K_{intrinsic} = \frac{\varepsilon d_h^2}{16 C_{KC}} \tag{3.1}$$

where C_{KC} is the proportionality factor known as Kozeny Constant. C_{KC} values for each case were calculated and plotted in Figure 3.4(b). Multiple studies suggest various forms of equations to describe the variation of C_{KC} as a function of porous systems' parameters. Detailed discussions can be found in Reference 81. Similar to earlier experiences, a power-law relation with porosity combined with the constants defined by the pore to throat size ratio (given in Equation (3.2)) was found best to describe the behavior observed in Figure 3.4(b).

$$C_{KC} = A\varepsilon^B \tag{3.2}$$

while the constants were determined as,

$$A = 6.56 R_{pt}^{1.98} \quad \text{and} \quad B = 5.56 R_{pt}^{-1.6} \tag{3.3}$$

starting from the original definition of hydraulic diameter as,

$$d_h = \frac{4 \times \text{Internal Cross Section Area}}{\text{Internal Perimeter}} = \frac{4A_c}{P} \tag{3.4}$$

where A_c is the cross-sectional area of flow and P is the wetted perimeter of the cross-section. Kozeny simplified d_h for a porous system as,

$$d_h = \frac{4\varepsilon}{(1-\varepsilon)A_0} \tag{3.5}$$

here ε is the porosity, and A_0 is the ratio of the interfacial area between fluid and solid phases (A_{fs}) to solid volume (V_s) as $\left(A_0 = \frac{A_{fs}}{V_s}\right)$. In terms of currently defined porous system parameters, A_0 can be calculated as,

$$A_0 = \frac{2(H_{Darcy} - a) + 2(H_{Darcy} - b)}{(H_{Darcy} - a)(H_{Darcy} - b)} = \frac{4H_{Darcy} - 2(a+b)}{(1-\varepsilon)H_{Darcy}^2} \tag{3.6}$$

Equation (3.6) is simplified by describing *a* and *b* in terms of porosity and Darcy height as,

$$a = \frac{H_{Darcy}}{R_{pt}} \text{ and } b = \frac{H_{Darcy}\left(\varepsilon - \frac{1}{R_{pt}}\right)}{\left(1 - \frac{1}{R_{pt}}\right)} \tag{3.7}$$

while the definition of *b* comes from the definition of porosity for the REV model as,

$$\varepsilon = \frac{V_{void}}{V_{total}} = \frac{V_{total} - V_{solid}}{V_{total}} = \frac{H_{Darcy}^2 - \left[(H_{Darcy} - a)(H_{Darcy} - b)\right]}{H_{Darcy}^2} \tag{3.8}$$

By combining Equations (3.7) and (3.8), the final form of A_0 becomes as,

$$A_0 = \frac{2\left[2 - \frac{1}{R_{pt}} - \left(\frac{\varepsilon R_{pt} - 1}{R_{pt} - 1}\right)\right]}{H_{Darcy}(1-\varepsilon)} \tag{3.9}$$

By substituting Equation (3.9) into Equation (3.5), hydraulic diameter can be obtained as,

$$d_h = \frac{2\varepsilon H_{Darcy}}{\left(2 - \frac{1}{R_{pt}} - \frac{\varepsilon R_{pt} - 1}{R_{pt} - 1}\right)} \tag{3.10}$$

By using the description of d_h with ε, R_{pt}, and H_{Darcy} (Equation (3.10)), the Kozeny-Carman equation extended to calculate intrinsic permeability as a function of porosity, and R_{pt} reaches the final form given in Equation (3.11),

$$\frac{K_{intrinsic}}{H_{Darcy}^2} = \frac{\varepsilon^{\left(3-6.56R_{pt}^{-1.98}\right)}}{26.24\times R_{pt}^{1.98}\times\left(2-\frac{1}{R_{pt}}-\frac{\varepsilon R_{pt}-1}{R_{pt}-1}\right)} \tag{3.11}$$

Equation (3.11) can successfully predict the intrinsic permeability values presented in Figure 3.4(a) with an error of less than %5. Next, the similar ε and R_{pt} set at various levels of rarefaction to extend the devised Kozeny-Carman based model using Klinkenberg theory in slip flow regime was investigated. First, local Kn numbers at the pore throat and pore connectivity (Kn_a and Kn_b) were calculated based on the corresponding size of pore throat and pore connection (*a* and *b*) of each R_{pt} and porosity case. If any of the local Kn values exceeds the applicability limit of slip velocity boundary conditions given in Equations (2.18) and (2.19) (Kn ~ 0.3 ± 0.1), corresponding REV geometry is removed from considerations. It should also be mentioned here that the velocity slip boundary condition is calculated based on local velocity gradient and gas mean free path only. For a beginning, Kn numbers were defined using H_{Darcy} similar to existing literature and denoted these as Kn_{Darcy} ($Kn_{Darcy} = \lambda/H_{Darcy}$). Keeping the porosity constant at ε = 0.5, the rarefaction level at different R_{pt} values were varied. Velocity contours measured through two-dimensional REVs are shown in Figure 3.5.

Velocity values were normalized by the average velocity measured at the corresponding case. First, low R_{pt} cases develop straight streamlines similar to a straight channel case. With the increase of R_{pt}, secondary flow patterns increase as the pore voids grow in these constant porosity cases. These secondary flows disturb the main flow pattern, which becomes more diffused into pore voids by increasing R_{pt}. High R_{pt} values representing tight porous systems undergo significant velocity differences between pore throats and voids. This effect becomes more profound for tighter pores by increasing R_{pt}. Results clearly show that very different flows develop regardless of the constant porosity, that the flow characterization solely based on the porosity is incomplete. Next, rarefaction effects growing with the increasing Kn yields smaller velocity gradients and more uniform velocity distributions in pore throats. Due to the gas slippage on the pore surfaces, gas velocity at pore throat center increases while the secondary flows in the voids lessen.

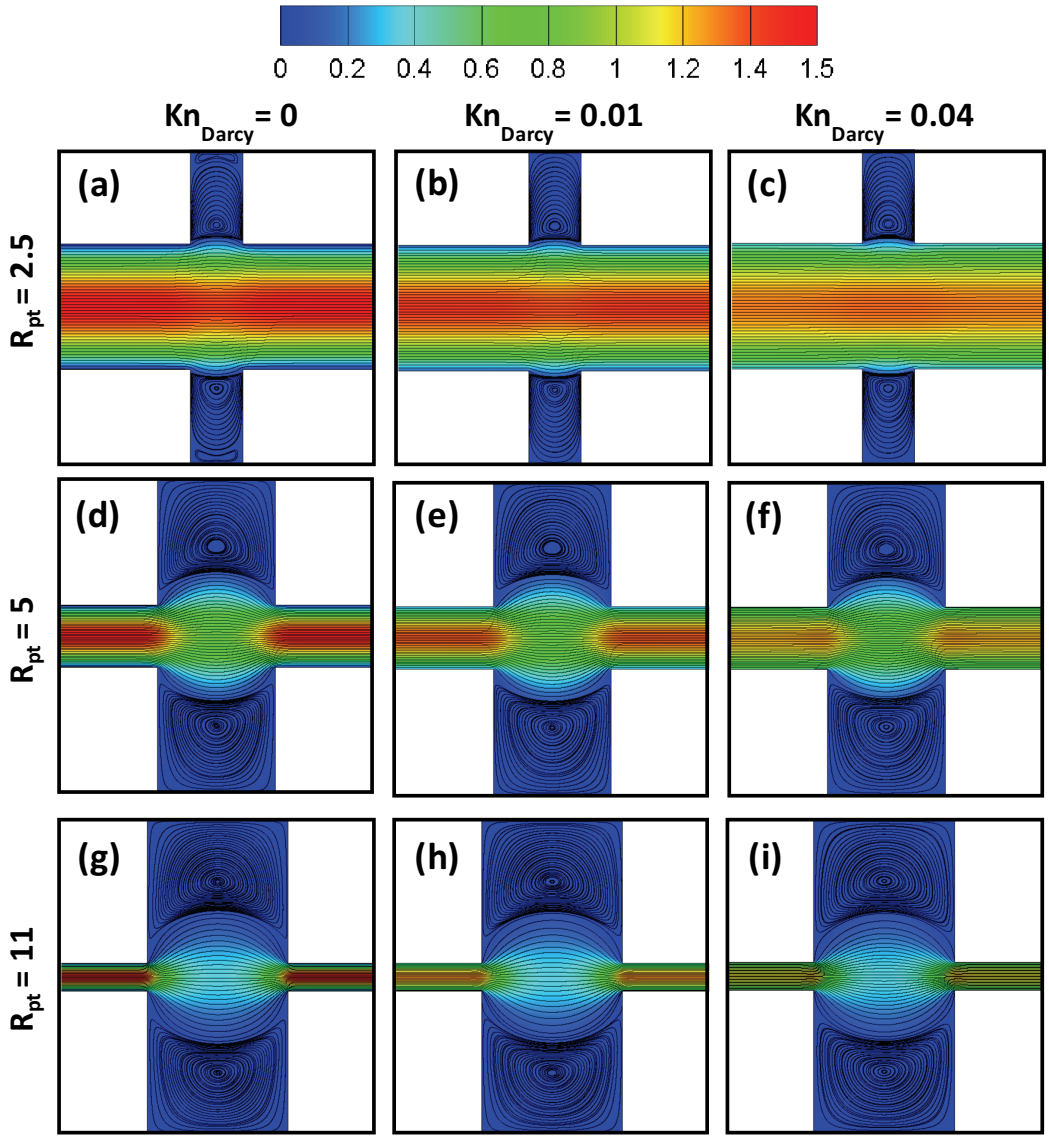

Figure 3.5. Velocity contours and streamlines of the 0.5 porosity cases at different pore to throat size ratios and rarefaction levels.

The permeability values calculated from Darcy's Law Equation (2.8) were normalized by H_{Darcy} and plotted in Figure 3.6. Figure 3.6 is a combination of nine figures of nine porosity values ranging from 0.1 to 0.9. At a constant porosity, Kn was varied for the different pore to throat size ratios. At first glance, permeability values increase by increasing Kn. Overall, an increase in porosity yields higher permeabilities, while an increase in R_{pt} decreases permeability values in every case. For instance, if comparing the specific case of $R_{pt} = 5$, $\varepsilon = 0.5$ at two rarefaction levels ($Kn_{Darcy} = 0$ and $Kn_{Darcy} = 0.04$), 87% of increase in permeability was observed, which shows the significance of slip effects in gas flows.

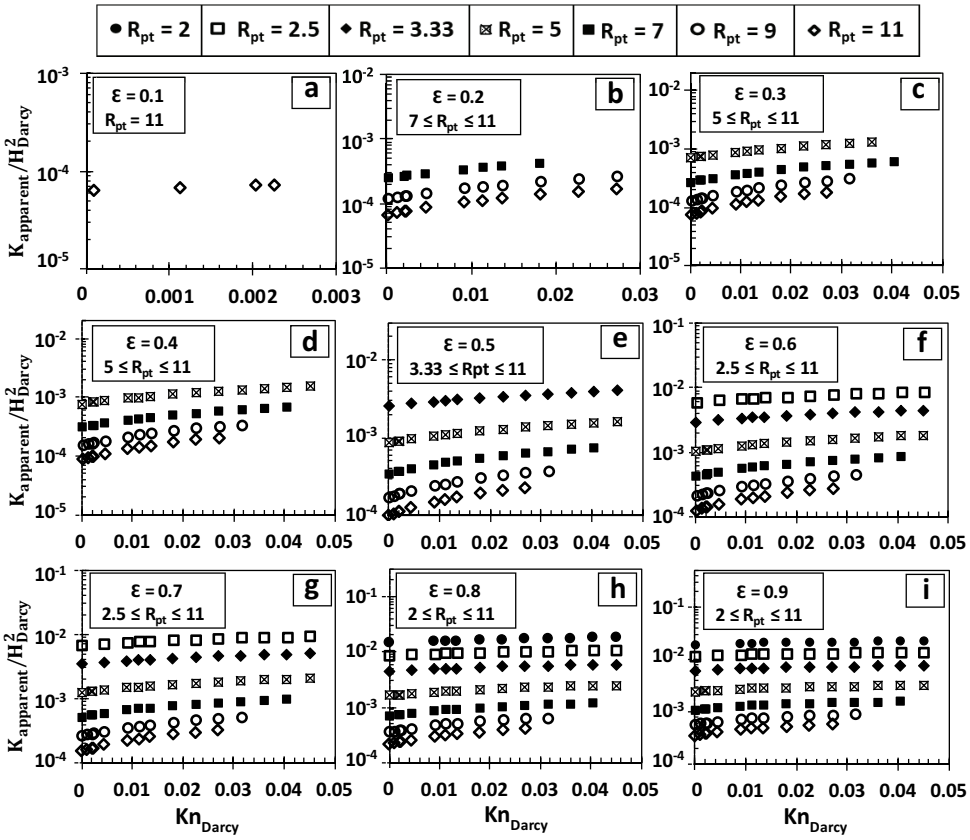

Figure 3.6. Permeability values of different porosity and pore to throat size ratio values at different rarefaction levels described by Kn calculated from Darcy height.

In order to see the comparable behavior, normalized K values were normalized with the intrinsic K value of the corresponding case at the given ε and R_{pt}. Figure 3.7 presents these results. On the order of the Kn_{Darcy}, higher Kn effects develop at higher R_{pt} cases representing tighter systems. This outcome is very similar to the conclusions of the existing studies; however, it is questionable since Darcy height is an average representative size for a porous system and cannot describe the confinement size as a measure for rarefaction. Instead, a proper Kn calculation for the correct characterization of rarefaction effects on permeability was tried. First, another well-known concept, hydraulic diameter was implemented.

Figure 3.8 presents the same results as a function of Kn_{d_h} calculated from the corresponding d_h of each case. Even though Kn_{d_h} provided successful rarefaction characterization for the case of straight tubes in complex shapes (square, triangular, etc.), such definition could not create a general normalization for rarefied flow data.

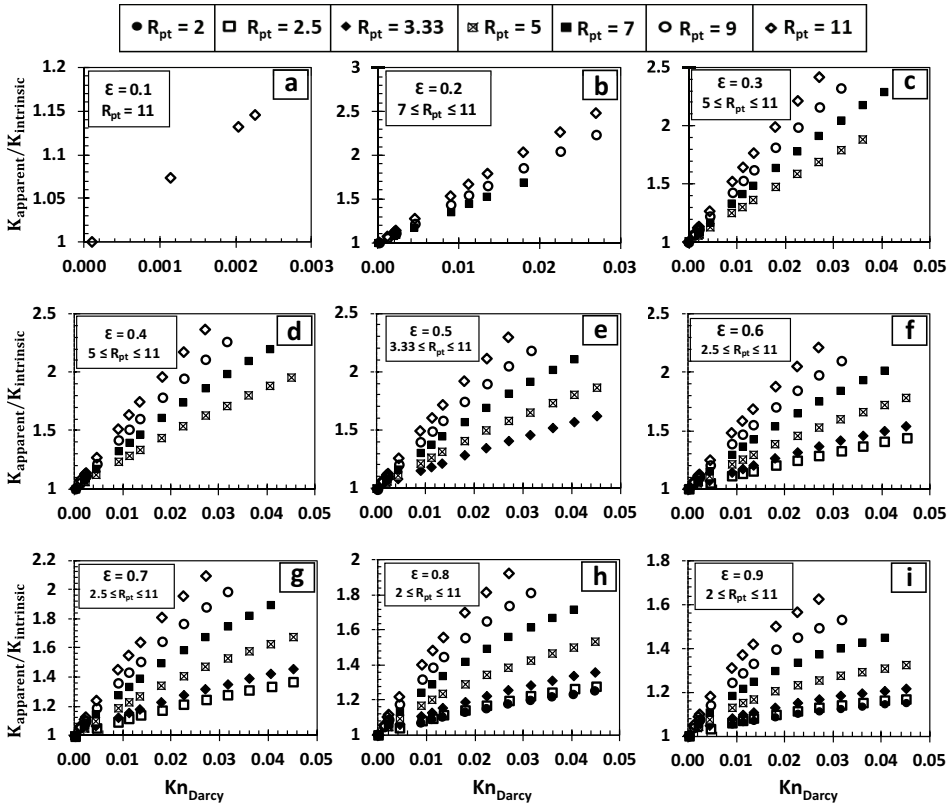

Figure 3.7. Permeability values of different porosity and pore to throat size ratio values at different rarefaction levels based on H_{Darcy}.

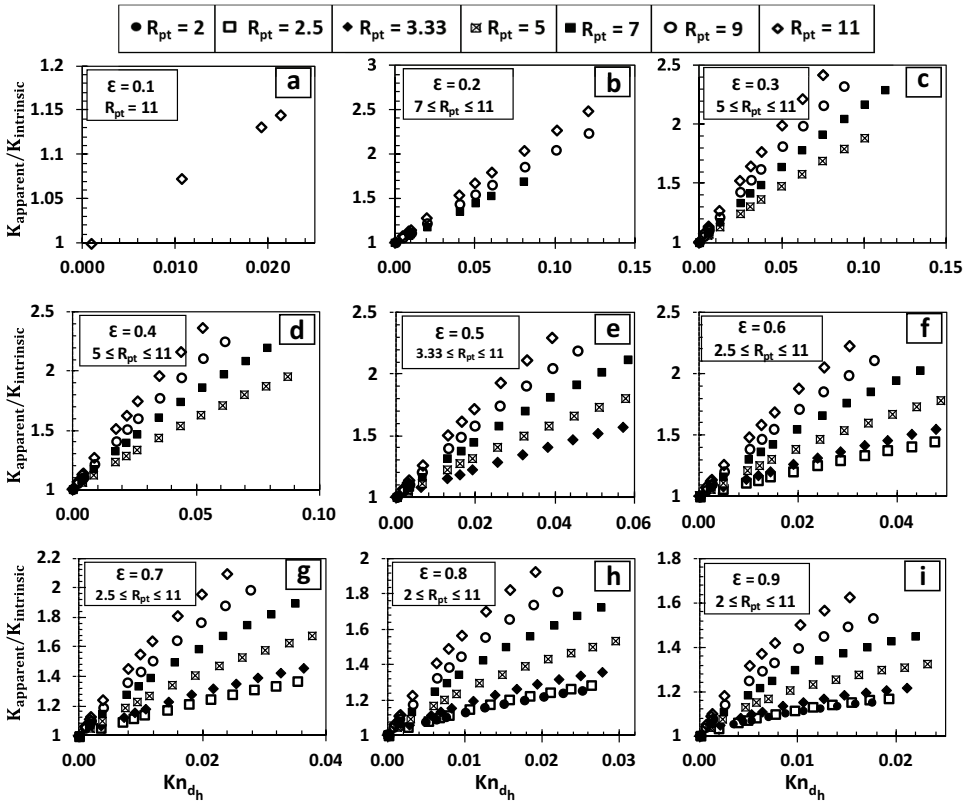

Figure 3.8. Permeability values of different porosity and pore to throat size ratio values at different rarefaction levels based on d_h.

In Figure 3.7 and Figure 3.8, Kn number is normalized by H_{Darcy} and d_h respectively. The trend of normalized permeability is similar in both graphs. However, they are case-specific for each porosity and R_{pt} value. It is observed that this type of definition for Kn number could not provide a general relationship, and another definition should be proposed. Instead, porous confinement requires the characterization of secondary flow sites such as pore voids between pore throats. This can only be possible by defining an equivalent diameter from the corresponding permeability value. For such a case, equalizing the velocity calculated from the Hagen-Poiseuille equation for the bundle of tubes at the corresponding porosity (ε) to the velocity from Darcy's equation as given in Equation (3.12), an equivalent diameter of the porous system can be defined by Equation (3.13),

$$\varepsilon \frac{d_{eq}^2}{32\mu}\frac{dP}{dx} = \frac{K_{apparent}}{\mu}\frac{dP}{dx} \tag{3.12}$$

$$H_{eq}\ or\ d_{eq} = \sqrt{32\frac{K_{apparent}}{\varepsilon}} \tag{3.13}$$

By using above Equation, Kn can be calculated as,

$$Kn_{Eq} = \frac{\lambda}{d_{eq}} \tag{3.14}$$

Permeability results of Figure 3.6 normalized with the corresponding intrinsic permeability values calculated from the KC relation were lined in Figure 3.9 as a function of newly defined Kn_{Eq}. Different from the other two failed Kn-based normalization attempts using H_{Darcy} and d_h, this time results of various R_{pt} structures of a certain porosity were lined up and showed a collective behavior. Basically, permeability showed an almost universal linear variation by the change of Kn_{Eq} independent of R_{pt}. Next, linear mathematical fit in which the relationship between an independent variable and the dependent variable is constant for all values of the independent variable, were applied to the results to characterize the variation. Resulted functions were given on each figure with the corresponding R-squared value for regression. Linear fits showed a perfect match with data except for the very high porosity case of ε = 0.9. In this porosity the deviation of the results from linearity specially at high Kn values may be related to the existence of large void space. Probably, in this case due to the lack of sensitivity or imprecise mesh the Computational fluid dynamics (CFD) results developed an unexpected numerical error.

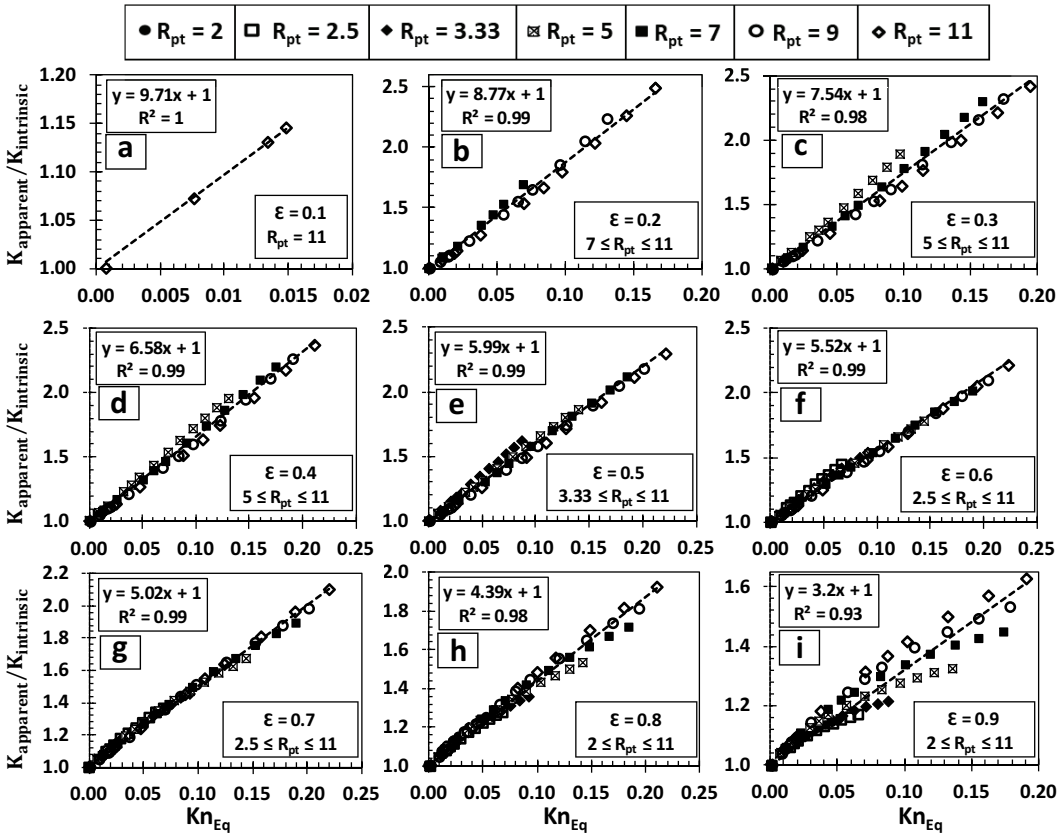

Figure 3.9. Normalized Permeability values of different porosity and pore to throat size ratio values at different rarefaction levels described by Kn calculated from an equivalent diameter.

The current observed behavior is very similar to linear Kn dependence estimated by Klinkenberg. Hence, the following form of Klinkenberg equation as the combination of Equations (1.1), (1.2), and (3.12) was employed to model observed behavior,

$$K_{apparent} = K_{intrinsic}\left(1 + C_K Kn_{Eq}\right) \tag{3.15}$$

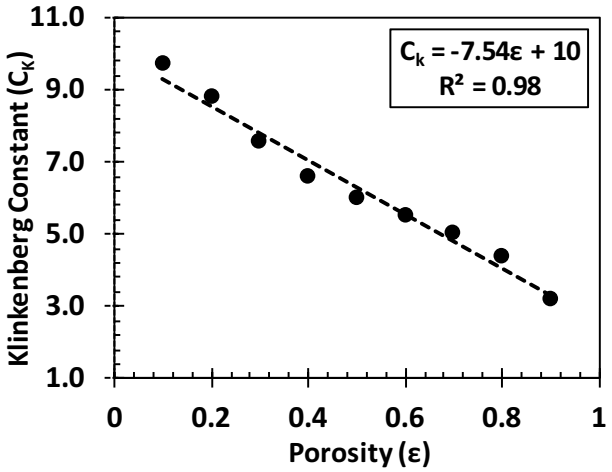

Figure 3.10. Klinkenberg constants at different porosities

Unlike Klinkenberg's original assumption ($C_K = 4c \approx 4$), Klinkenberg constant (C_K) variation from the linear fits was calculated in Figure 3.9. The slopes of the linear fits showed variation by porosity, independent from the R_{pt}. For such a case, variation of C_K by porosity was plotted in Figure 3.10. C_K was found to decrease almost linearly by increased porosity. A second-order fit showed a perfect match with the C_K variation, a linear fit but was employed to keep the model simple. Linear fit created good results with an R-square value of 0.98.

By combining the linear C_K model and Equation (3.13) into Equation (3.15), Klinkenberg model became,

$$K_{apparent} = K_{intrinsic}\left(1+\left(10-7.54\varepsilon\right)\frac{\lambda}{\sqrt{\frac{32\,K_{apparent}}{\varepsilon}}}\right) \tag{3.16}$$

while the $K_{intrinsic}$ is a known quantity from Equation (3.11), $K_{apparent}$ can be predicted by solving the above equation. For such a case, Equation (3.16) can be rearranged as

$$K_{apparent}^{3/2} - K_{intrinsic}\times K_{apparent}^{1/2} - \frac{\sqrt{\varepsilon}\left(10-7.54\varepsilon\right)\lambda}{\sqrt{32}}\times K_{intrinsic} = 0 \tag{3.17}$$

In order to link the model with the current practices, Equation (3.17) was divided with H_{Darcy}^3. In this way, the general definition of the Kn in porous media was also created as Kn_{Darcy},

$$\frac{K_{apparent}^{3/2}}{H_{Darcy}^3} - \frac{K_{intrinsic}}{H_{Darcy}^2}\times\frac{K_{apparent}^{1/2}}{H_{Darcy}} - \frac{\sqrt{\varepsilon}\left(10-7.54\varepsilon\right)Kn_{Darcy}}{\sqrt{32}}\times\frac{K_{intrinsic}}{H_{Darcy}^2} = 0 \tag{3.18}$$

Equation (3.18) is in the form of a third-degree polynomial function of the unknown $K^{1/2}_{apparent,}$ while the $K_{intrinsic}$ is a known quantity from Equation (3.11). For the solution of this cubic polynomial, two cases exist depending on the below criteria:

if,

$$\frac{\left[-\frac{K_{intrinsic}}{H_{Darcy}^2}\left(\frac{\sqrt{\varepsilon}\left(10-7.54\varepsilon\right)Kn_{Darcy}}{\sqrt{32}}\right)\right]^2}{4} + \frac{\left(-\frac{K_{intrinsic}}{H_{Darcy}^2}\right)^3}{27} > 0 \tag{3.19}$$

then,

$$\frac{K_{apparent}}{H_{Darcy}^2} =$$

$$\left(\sqrt[3]{-\frac{\left[-\frac{K_{intrinsic}}{H_{Darcy}^2}\left(\frac{\sqrt{\varepsilon}(10-7.54\varepsilon)Kn_{Darcy}}{\sqrt{32}}\right)\right]}{2}+\sqrt{\frac{\left[-\frac{K_{intrinsic}}{H_{Darcy}^2}\left(\frac{\sqrt{\varepsilon}(10-7.54\varepsilon)Kn_{Darcy}}{\sqrt{32}}\right)\right]^2}{4}+\frac{\left(-\frac{K_{intrinsic}}{H_{Darcy}^2}\right)^3}{27}}} + \sqrt[3]{-\frac{\left[-\frac{K_{intrinsic}}{H_{Darcy}^2}\left(\frac{\sqrt{\varepsilon}(10-7.54\varepsilon)Kn_{Darcy}}{\sqrt{32}}\right)\right]}{2}-\sqrt{\frac{\left[-\frac{K_{intrinsic}}{H_{Darcy}^2}\left(\frac{\sqrt{\varepsilon}(10-7.54\varepsilon)Kn_{Darcy}}{\sqrt{32}}\right)\right]^2}{4}+\frac{\left(-\frac{K_{intrinsic}}{H_{Darcy}^2}\right)^3}{27}}} \right)^2 \tag{3.20}$$

while the second root develops if,

$$\frac{\left[-\frac{K_{intrinsic}}{H_{Darcy}^2}\left(\frac{\sqrt{\varepsilon}(10-7.54\varepsilon)Kn_{Darcy}}{\sqrt{32}}\right)\right]^2}{4}+\frac{\left(-\frac{K_{intrinsic}}{H_{Darcy}^2}\right)^3}{27}<0 \tag{3.21}$$

then,

$$\frac{K_{apparent}}{H_{Darcy}^2}=\frac{4}{3}\frac{K_{intrinsic}}{H_{Darcy}^2}\left(\cos\left(\frac{1}{3}arccos\left(\sqrt{\frac{\frac{\left[-\frac{K_{intrinsic}}{H_{Darcy}^2}\left(\frac{\sqrt{\varepsilon}(10-7.54\varepsilon)Kn_{Darcy}}{\sqrt{32}}\right)\right]^2}{4}}{\frac{\left(\frac{K_{intrinsic}}{H_{Darcy}^2}\right)^3}{27}}}\right)\right)\right)^2 \tag{3.22}$$

Equation (3.22) can be simplified into an algebraic description of cos(3x) trigonometric function,

Let, $x=\frac{1}{3}\cos^{-1}\left(H_{Darcy}\left|\sqrt{\varepsilon}C_K Kn_{Darcy}\right|\right)\sqrt{\frac{0.221}{K_{\text{int}rinsic}}}$

$$\cos x=\frac{3}{4}\frac{K_{apparent}}{K_{\text{int}rinsic}}=\cos\left(\frac{1}{3}\cos^{-1}\left(\left(\left|H_{Darcy}\sqrt{\varepsilon}C_K Kn_{Darcy}\right|\right)\sqrt{\frac{0.221}{K_{\text{int}rinsic}}}\right)\right) \tag{3.23}$$

Using $\cos 3x=4\cos^3 x-3\cos x$

$$\cos(3x)=\left(H_{Darcy}\sqrt{\varepsilon}C_K Kn_{Darcy}\right)\sqrt{\frac{0.221}{K_{\text{int}rinsic}}}=\frac{27}{16}\left(\frac{K_{apparent}}{K_{\text{int}rinsic}}\right)^3-\frac{9}{4}\frac{K_{apparent}}{K_{\text{int}rinsic}} \tag{3.24}$$

The final simplified version can be written as,

$$\frac{27}{16}\left(\frac{K_{apparent}}{K_{\text{int}rinsic}}\right)^3-\frac{9}{4}\frac{K_{apparent}}{K_{\text{int}rinsic}}=\left(H_{Darcy}\sqrt{\varepsilon}C_K Kn_{Darcy}\right)\sqrt{\frac{0.221}{K_{\text{int}rinsic}}} \tag{3.25}$$

Finally, to find the apparent permeability as a function of the intrinsic permeability in the normalized form, there can be some simplifications of Equation (3.22) as,

$$\frac{K_{apparent}}{H_{Darcy}^2} = \frac{4}{3}\frac{K_{\text{int}rinsic}}{H_{Darcy}^2}\cos\left(\frac{1}{3}\cos^{-1}\sqrt{\frac{-0.221(\sqrt{\varepsilon}C_K Kn_{Darcy})^2}{-\frac{K_{\text{int}rinsic}}{H_{Darcy}^2}}}\right) \tag{3.26}$$

As a result, the solution of Equation (3.18) as Equation (3.20) and (3.22) provide the apparent gas permeability in terms of porosity, Darcy length of the porous system, intrinsic permeability (liquid permeability), and Kn_{Darcy} as an extension of Klinkenberg model. The final model was tested on the current results. Comparison presented in Figure 3.11 shows good agreement between the numerical results and the apparent permeability predictions of extended Klinkenberg model combined with the extended Kozeny-Carman model calculating intrinsic permeability (Equation (3.11)).

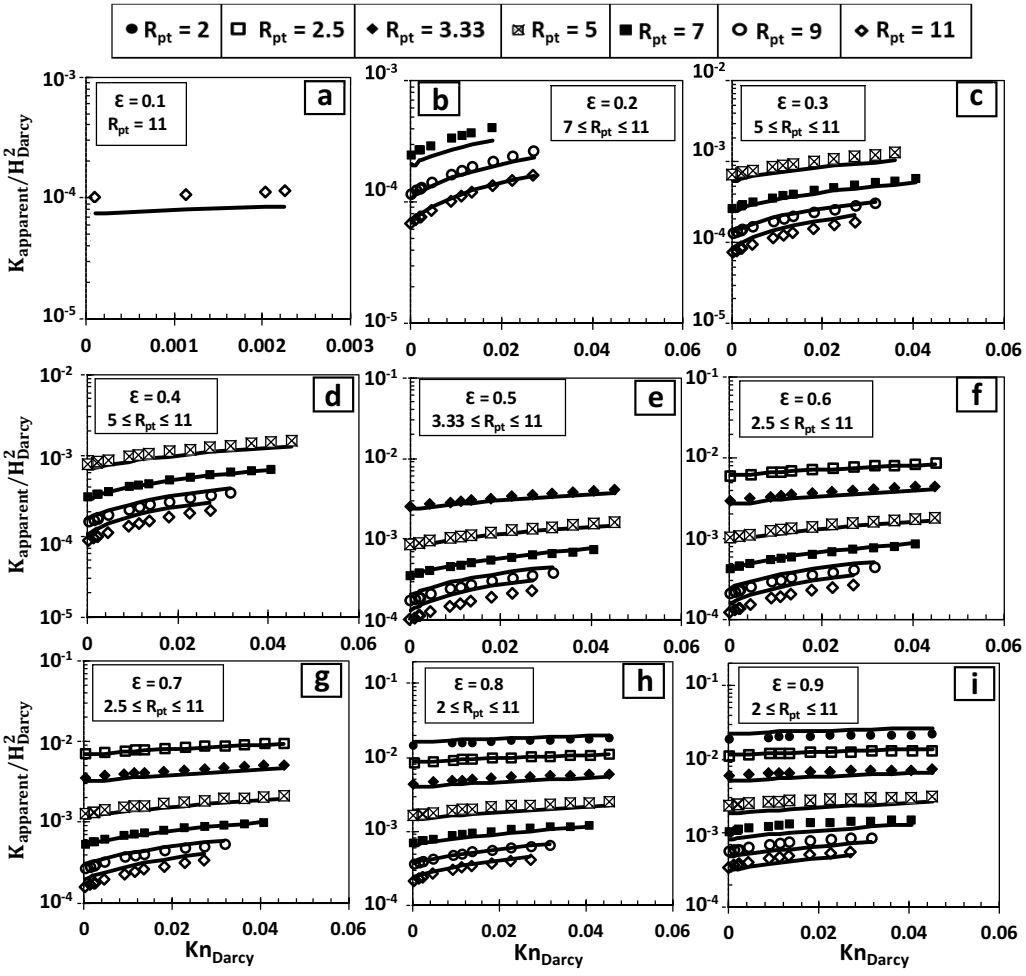

Figure 3.11. Comparison of the permeability predictions of the current model with the numerical calculations.

3.3. Conclusion

Gas transport through micro/nano porous systems differs from conventional calculations due to non-equilibrium in gas dynamics at small confinements. The extended Kozeny-Carman theories and their alternatives estimating permeabilities as a function of pore parameters need to be corrected to consider gas rarefaction effects. This was widely practiced using various forms of Klinkenberg and similar theories, but a general characterization is missing. One of the problems is about the accurate definition of Kn number to characterize rarefaction level. In Kn calculations, existing theories frequently use Darcy defined pore size or hydraulic dimeter, which does not consider pore connectivity and the related secondary flow dynamics of a porous system. For such case, pore-level gas dynamic calculations were performed for different pore dimensions, porosities, pore to throat size ratios, and rarefaction levels. Overall, permeability values increased by increasing porosity and reduced by increment of pore to throat size ratio. First, Kozeny-Carman based model for intrinsic permeability calculations as a function of porosity and pore to throat size ratio was developed. Next, it is observed that gas rarefaction also increased permeability at different flow rates referring to variable pores. The change of permeability as a function of Kn number calculated from Darcy Height or Hydraulic diameter showed dependence on both porosity and pore to throat size ratio. Instead, an equivalent diameter was calculated as a function of the apparent permeability of the corresponding system. Permeability variation by Kn from equivalent diameter became a simple function of porosity, independent from pore connectivity. For such a case, the Klinkenberg model was employed by only estimating the Klinkenberg constant as a linear function of porosity. However, such representation of Kn in terms of the unknown permeability creates an implicit equation. First time in literature, the equivalent diameter based Klinkenberg equation was solved and devised an extended model based on standard Darcy height. A new model combined with Kozeny-Carman and Klinkenberg was tested on the existing data set, where good agreements were observed.

CHAPTER 4

RAREFACTION EFFECTS ON GAS PERMEABILITY IN DUAL-SCALE POROUS MEDIA

Basically, porous medium is defined as a solid with holes. The space within a porous domain is formed by a solid matrix and void space. This space may alter over time as a result of natural or artificial processes[95–97]. For instance, precipitation reactions[98] or swelling of minerals[99] create multiple pore regions within a porous structure. This distribution of pores throughout the system may be divided into major and minor (inter-intra) types generally observed in dual-scale porous media[100]. In this porous media type, the main flow occurs in major porosity, which is the region between pores.

On the other hand, the minor porosity is the interior parts of solid which may be dead-end or channels with only a narrow single connection like a fracture[101,102]. For example, hydraulic fracturing is a common practice method to extract gas from the shale layer in deep ground. In this method, a large amount of water gallons, sand, and chemical mixtures are injected at very high pressures in underground to crate fractures inside porous layers[103,104]. Such porous systems were created and studied in laboratory experiments in a very similar form as the "reservoir-on-a-chip" (Figure 4.1)[105] to characterize the flow behavior in tight dual-scale porous media.

There are many modeling relations available in the literature for estimating intrinsic permeability in porous media, and one of the well-known relationships is Kozeny-Carmen (KC) equation. By using this equation, one can measure the intrinsic permeability as a function of porosity and hydraulic diameter. However, predicting permeability value based on these parameters is not sufficient to characterize the transport in the porous medium. Since the shape and connectivity of solid particles are composed of various forms of hydraulically resistive path (throats), secondary pores (intraparticle) can significantly impact transport in porous medium.

Yu and Cheng[106] proposed a model based on fractal theory to estimate permeability of bi-dispersed porous medium. They showed that at the same porosity the value of permeability in mono-scale porous medium is greater than the bi-dispersed one. Chastanet et al.[107] used homogenization theory to describe a macroscopic model for gas

flow in low-pressure dual-porosity porous medium. They found that effective permeability is mainly relies on the size of pore and local flow regime in a fractured porous medium based on Klinkenberg's or Knudsen's diffusion models. Zheng and Yu[108] investigated permeability of gas through a matrix of porous medium embedded with randomly shape of fractal-like tree networks. They concluded that the gas permeability decreases due to longer flow pathways and higher resistance by increasing the branching levels. A model corresponding with fractal gas diffusion model is recommended to predict permeability of micro/macro porous membranes by Zhang[109]. The effect of fractal dimension was calculated on permeability variations. Lower permeability is observed by increasing the fractal dimension because of high tortuosity effects, increasing the diffusion path and resistances. In the work of Xu and Yu[106] a new analytical approach is suggested to describe permeability and the Kozeny-constant constant related to the fractal geometry for homogenous porous medium. In T de. Vries et al.[110] work on several dual-porosity systems by connecting many aggregates into the macropore structure. They analyzed the effects of pore-scale properties like permeability and porosity on macroscopic transport parameters in dual-porosity porous medium.

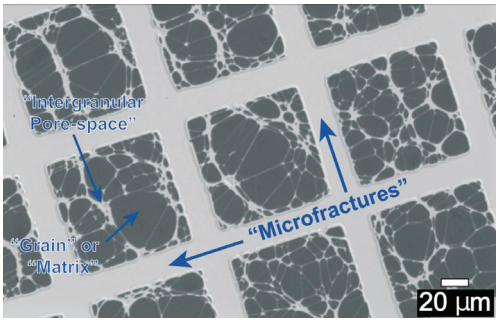

Figure 4.1. Dual porous system built in a "reservoir-on-a-chip"[105] due to its easy to control porous system parameters.

In this part of the study, the focus is to find the apparent gas permeability in the porous system with dual-scale pores. Darcy equation was used to calculate the gas permeability values of a porous structure with different pore to throat size ratios (R_{pt}) and intraparticle dimensions (t). The results were compared with the previous section, which holds results for mono-scale results. Unlike other studies that use Darcy length or hydraulic diameter for calculating Kn number, the new Kn definition was employed based on gas permeability for dual-scale porous medium. It is observed that the empirical model developed for the mono-scale porous medium can also be extended to be valid for porous structure with multi pores providing high accuracy results.

4.1. Simulation Details

Similar to the previous section, a Representative Elementary Volume (REV) concept is used to discretize porous medium structure. The schematic of the porous medium selected for this study is shown in Figure 4.2, where square rods with intraparticle pores inside are in-line arrangements with uniform geometry. As discussed before, the ratio of pore size (H_{Darcy}) to throat size between solid parts (a) is given as R_{pt} (H_{Darcy}/a). Likewise, H_{Darcy} is chosen for the size of REV, while the solid particle and secondary pore dimensions are denoted as D and t, respectively. R_{pt} characterizes the pore connectivity inside the REV and as its value increases the throat size decreases, making the structure tighter. It is possible to have a porous structure with different R_{pt} while keeping the porosity value constant.

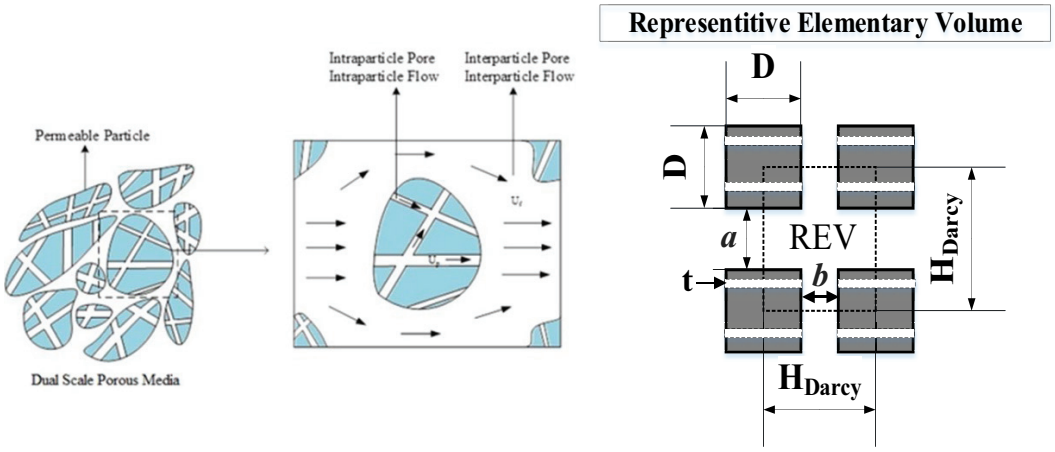

Figure 4.2. REV with intraparticle pores.

Air is used as the working fluid inside the REV with constant thermo-physical properties. Air density and pressure were changed to obtain different Kn values while the dynamic viscosity was maintained at a constant value of 18.21×10^{-6} kg/ms. The flow in the voids between the particles is assumed incompressible and steady. Pressure and velocity fields are estimated by solving continuity and Navier-Stokes formulation given in Equations (2.15), (2.16), and (2.17). Slip velocity given in Equations (2.18) and (2.19) were applied on solid surfaces with a unity momentum accommodation coefficient, assuming diffuse reflections. Simulations were carried on Darcy region with low Re values to dismiss inertial effects. In this region, non-dimensional pressure drop does not change and has a constant value.

In the previous part of the study, intrinsic permeability values were calculated using the Kozeny-Carman theory, considering both porosity and pore to throat size ratio. Figure 4.3 shows the comparison between the mathematical model, which is given in Equation (4.1), with numerical results for dimensionless permeability values. The figure clearly shows that the mathematical model fits the values very well at different porosity and pore connectivity scales. This equation can be used to find intrinsic permeability in a mono-scale porous medium with less than 5% error.

$$\frac{K_{intrinsic}}{H_{Darcy}^2} = \frac{\varepsilon^{\left(3-6.56R_{pt}^{-1.98}\right)}}{26.24\times R_{pt}^{1.98}\times\left(2-\frac{1}{R_{pt}}-\frac{\varepsilon R_{pt}-1}{R_{pt}-1}\right)} \tag{4.1}$$

The intraparticle dimension is evaluated based on R_{pt} values for a given porosity such that its value does not exceed 1/3 of throat size (a) inside the REV. This limitation is considered regarding available studies[111–113] discussing the intraparticle size criteria inside the porous medium. To generate the intraparticle region for the system b (Figure 4.2) value is modified. The current study performed the calculation for four different porosities with values equal to 0.2, 0.4, 0.6, and 0.8 and three different intraparticle sizes. At the same time, the total porosity, R_{pt}, and mass flow rate were kept constant for proper comparison with mono-scale porous system.

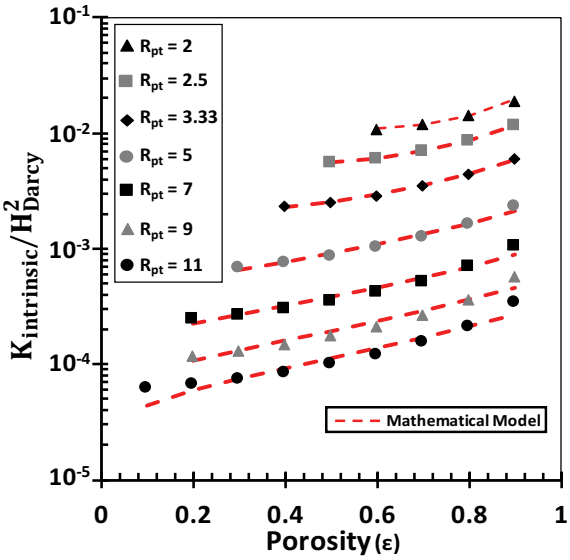

Figure 4.3. Variations of permeability inside the REV by porosity at different pore to throat size ratios.

4.2. Results and Discussions

One set of configurations created for the simulation in this study can be seen in Figure 4.4. The figure represents the normalized velocity contours and streamlines at different R_{pt} and rarefaction levels for $\varepsilon = 0.4$. The mean velocity of each corresponding case, normalized velocity values. As can be seen from the figure, particularly for R_{pt} values below 3.33, the streamlines are smooth, and flow resembles channel flow. However, as the throat becomes tighter (R_{pt} increases), the space between two solid particles in the horizontal direction gets larger, yields more fluid particles to penetrate in this region and create substantial secondary flows. These secondary flows disturb the main flow patterns and significantly impact the velocity distribution and transmissibility inside the REV. Adding intra pores to the system changes the shape of these secondary flows due to the tortuosity effect in the porous medium. The most different form of secondary flows is observed when the dimension of the intraparticle region becomes comparable with throat size. In these cases, the secondary flows are suppressed between two pores due to a significant stream passing through intraparticle pores. Next, the rarefaction effect was applied by changing the density and pressure inside the REV. As the Kn number increases, velocity gradients decrease, and more uniform velocity distribution was obtained as a result of gas slippage effect on pore surfaces. Additionally, in Figure 4.4, different values of Kn number inside the REV based on throat size (Kn_a), pore space between particles in the longitudinal direction (Kn_b), and finally intraparticle thickness (Kn_t) are also shown. Still, for this simple geometry, it is possible to define three different Kn values. However, determination of a characteristic height to quantify rarefaction effects of a such dual porous system is very challenging for a real porous medium with its complex shape. Thus, it is essential to establish a general concept to define proper Kn value for this type of porous system. Moreover, it should be mentioned here that the local Kn values which exceed the slip flow limit were not considered and excluded from simulation in all cases. Furthermore, it should be noted here that there are almost four times more data in the current results such that there are four different cases at different intra pore throat sizes at a given R_{pt} and porosity.

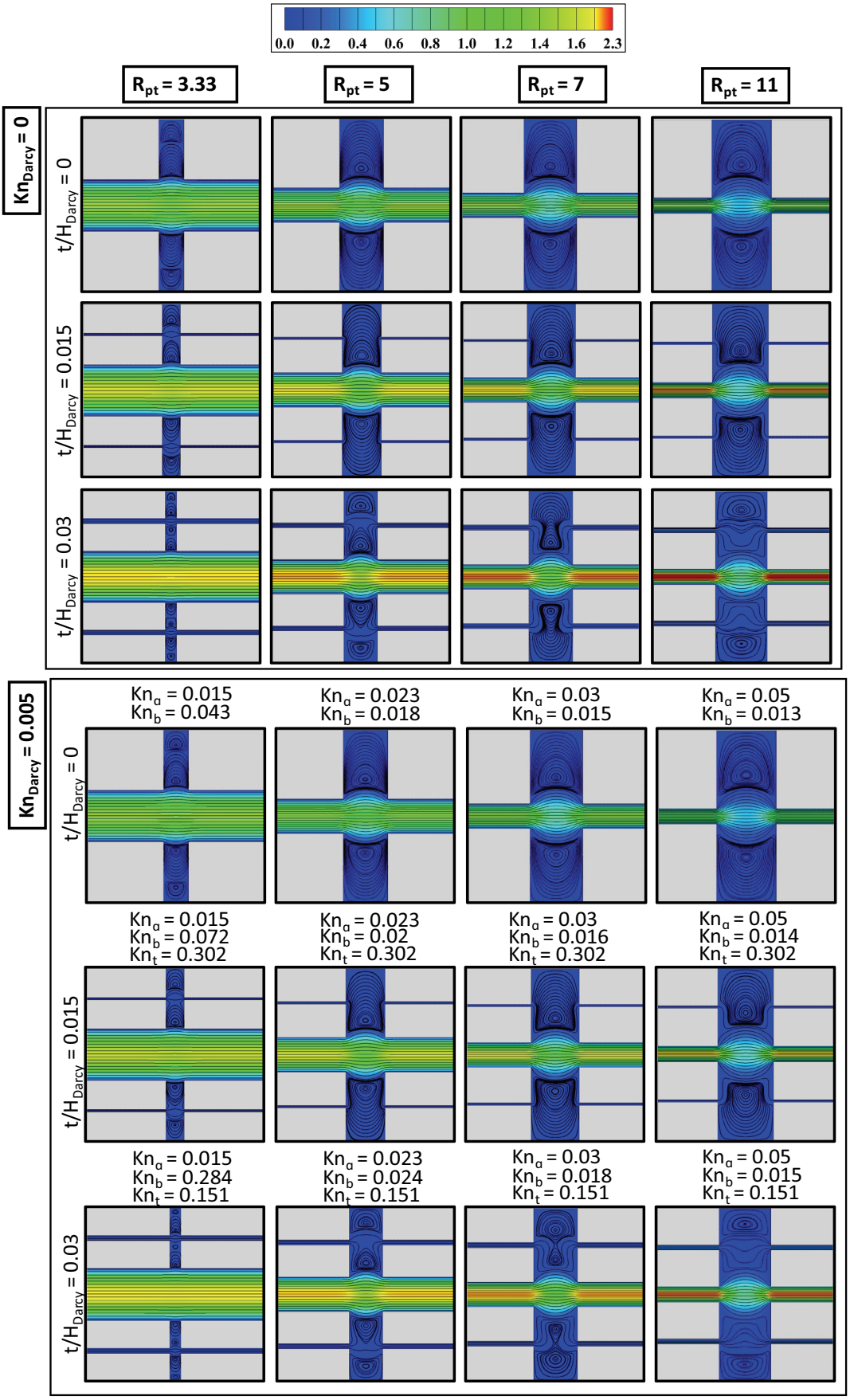

Figure 4.4. Velocity contours and streamlines for ε = 0.4 at different pore to throat size ratios and two different intra-pore thicknesses.

Figure 4.5 illustrates the intrinsic permeability results calculated from Darcy Equation for porous medium with different intraparticle sizes, normalized by the corresponding mono-scale results. The results represent the ratio of intraparticle dimension in two ways: first, with respect to throat size (Figure 4.5 a-d) and latter with REV dimension (Figure 4.5 e-f). The figures clearly show that for most cases at different porosity and pore to throat size ratios (R_{pt}), the effect of intraparticle region on permeability values is adverse. As mentioned earlier total porosity, $R_{pt,}$ and mass flow rate through dual-scale porous system were kept exactly the same as mono-scale system. The only parameter changed inside the REV is the distance between two pores (*b*) to maintain these constraints. As the intraparticle size increases, the *b* value is decreased. Due to this reason, fluid particles passing through the REV in the main flow direction experience more frictional forces, which ultimately decrease the permeability values. The only exception is observed at R_{pt} = 11, in which the dimension of intraparticle becomes comparable with throat size and the amount of fluid passing through this region enhanced significantly. Next, calculated apparent permeability at one specific rarefaction level is plotted in Figure 4.6. In two cases with R_{pt} values higher than 9 the permeability values are greater than mono-scales, while the remaining results show a negative trend on permeability values. The increase of permeability at R_{pt} = 9 and 11 can be clarified because of velocity slip on the pore surface, decreasing the drag and enhancing the movement of the fluid particles through the REV with less friction.

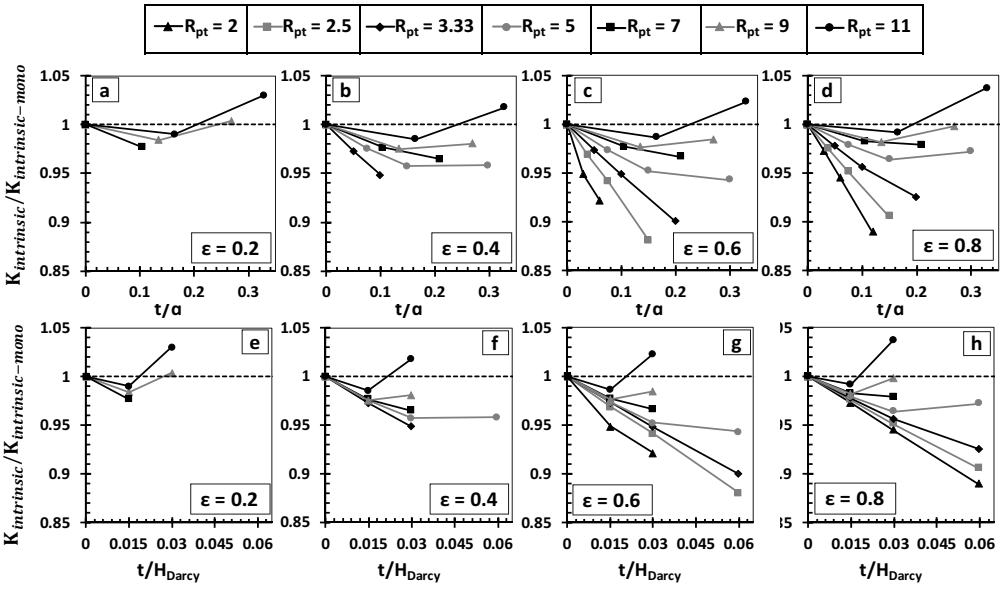

Figure 4.5. Intrinsic gas permeability calculation for dual-scale porous medium at different intraparticle, normalized by intrinsic mono-scale gas permeabilities, (a-d) with respect to throat size ratio, (e-h) with respect to REV dimension.

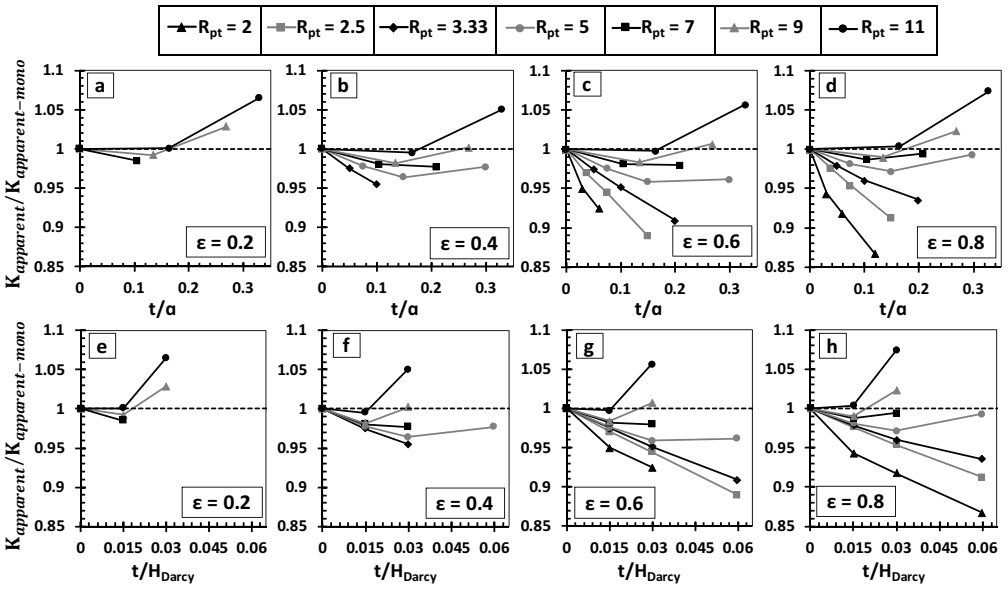

Figure 4.6. Apparent gas permeability calculation for dual-scale porous medium at different intraparticle, normalized by apparent mono-scale gas permeabilities (Kn_{Darcy} = 0.005), (a-d) with respect to throat size ratio, (e-h) with respect to REV dimension.

In Figure 4.7, the results for constant R_{pt} equal to 5 for different porosity and rarefaction levels are demonstrated. Three intraparticle pore sizes were selected, varying the dimensions based on throat size from 0.07 to 0.3. To obtain different rarefaction levels, the pressure inside the REV was changed. The resulted Kn numbers calculated based on pore size (H), pore throat size (*a*), and secondary pore throat size (t) are given below the figure. As can be seen from the figure, the increase of secondary pore size decreases the permeability up to t/α = 0.15 ratio, which increases due to the dominant slip effect. It is observed that the rarefaction in pore throats increases from bottom to top while rarefaction developing in secondary pores increases from right to left.

Similar to the previous part, further calculations to find apparent permeabilities at different pore to throat size ratios, secondary pore sizes, and porosities were performed. The results were normalized by intrinsic permeability and shown as a function of Kn_{Darcy} in Figure 4.8. These comprehensive results calculated based on characteristic height indicate that permeability values increase by increasing rarefactions. However, the definition of Kn_{Darcy} does not yield a uniform form of characterization for each porosity. Overall, Darcy height is an average description used for estimating porous medium dimensions and is not suitable for measuring rarefaction in all confinements.

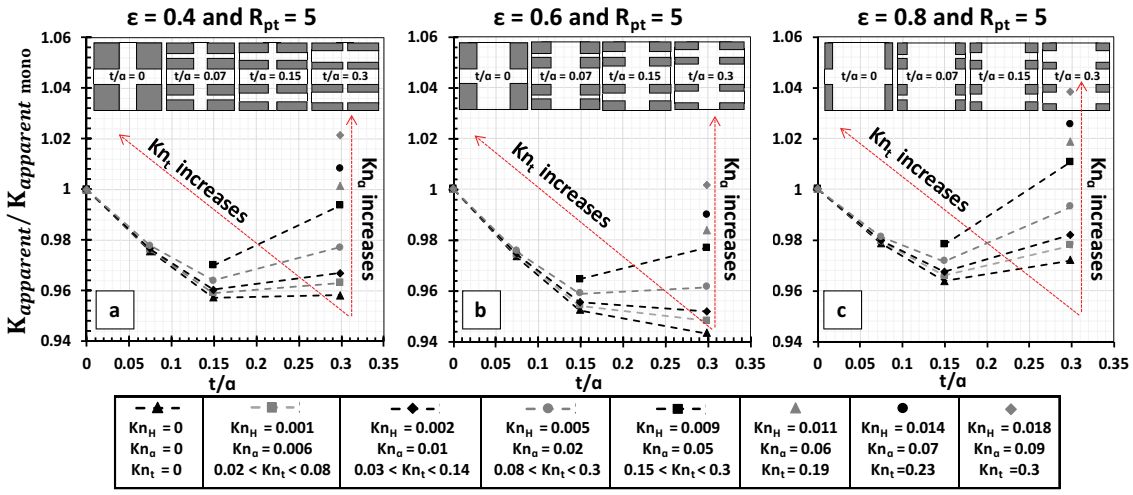

Figure 4.7. Permeabilities as a function of different secondary pore throat sizes (t) and rarefaction levels at overall porosity values of (a) 0.4, (b) 0.6, and (c) 0.8 with constant pore size (H) to pore throat size (α) ratio, R_{pt} = 5.

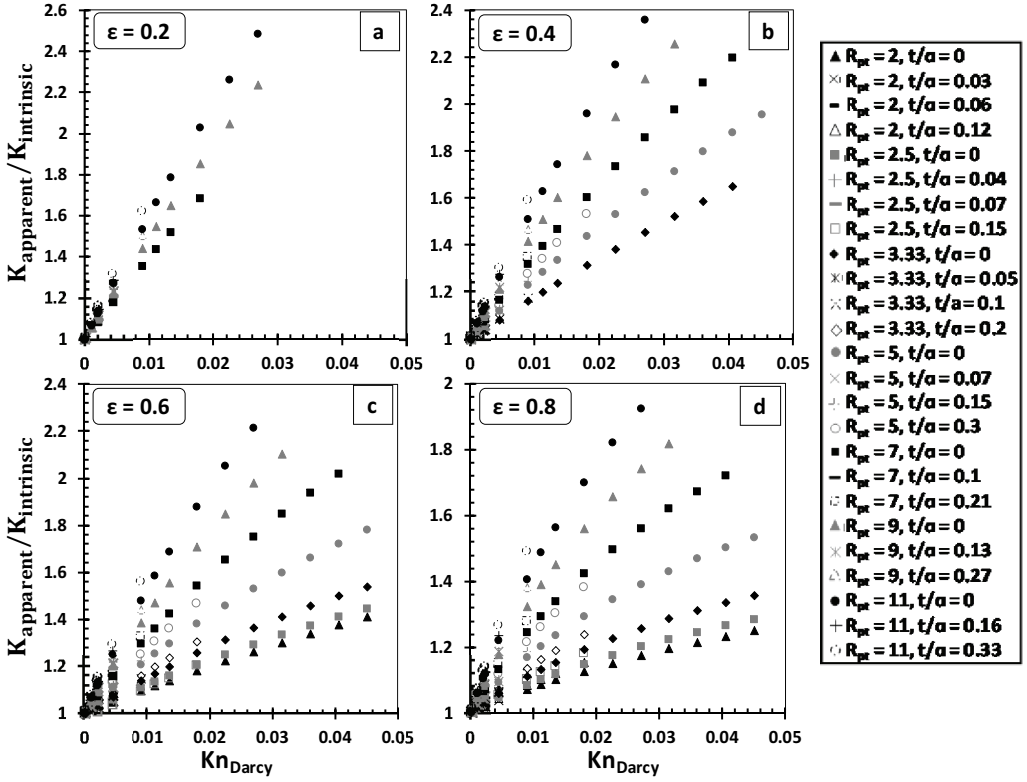

Figure 4.8. Permeability values at different rarefaction levels described by Kn calculated from Darcy height.

Alternatively, a proper Kn definition that can establish a general characterization without considering the pore connectivity effects or secondary pore sizes was described. It was realized that it is possible to define and calculate equivalent diameter in the porous media based on Hagen-Poiseuille and Darcy's equations. The equivalent diameter is

derived from the definition of Darcy velocity for low Reynold values and Hagen-Poiseuille for a bundle of tubes combined in the following form:

$$d_{eq} = \sqrt{32 \frac{K_{apparent}}{\varepsilon}} \tag{4.2}$$

by using the above Equation, Kn can be calculated as,

$$Kn_{Eq} = \frac{\lambda}{d_{eq}} \tag{4.3}$$

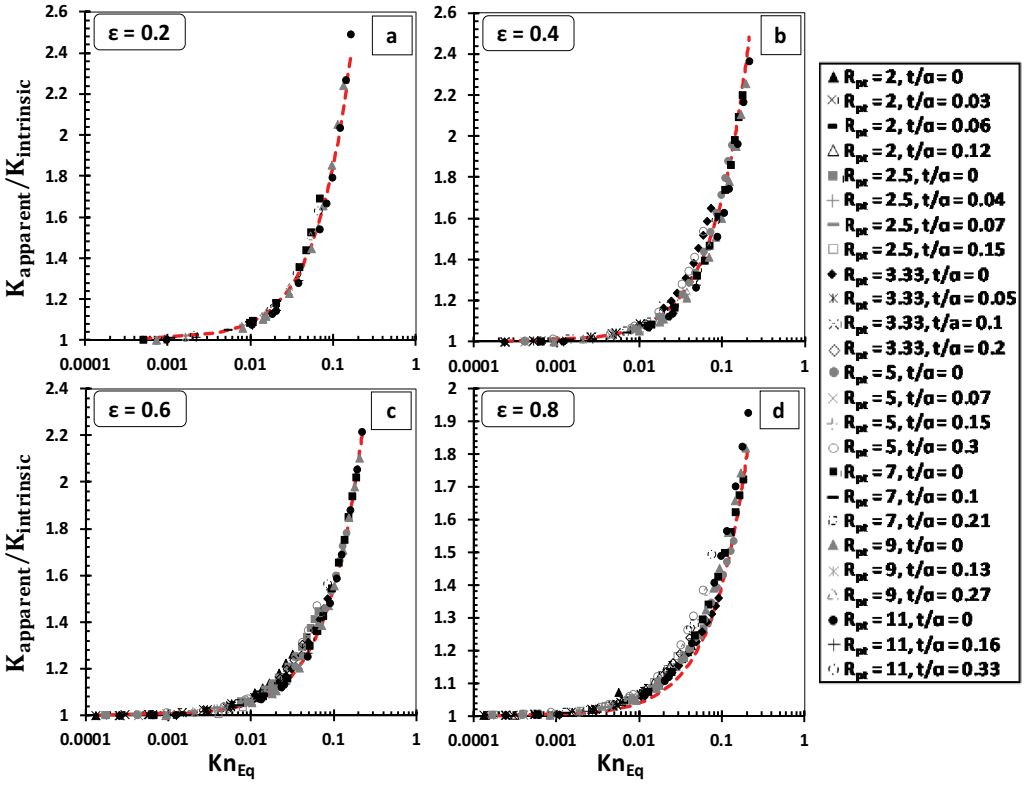

Figure 4.9. Normalized Permeability values of different porosity and pore to throat size ratio values at different rarefaction levels described by Kn calculated from equivalent diameter.

The normalized permeability values as a function of Kn_{Eq} are given in Figure 4.9. These results are in the form of Klinkenberg's suggested linear model. As Kn_{Eq} increases, permeability also increases in a linear variation. This is an important finding that the permeability values of dual porous systems lined up with the results of a mono porous system. Hence, it is possible to apply the extended phenomenological model given in the previous chapter to these results and observe a perfect match. The above results validate that the Kn_{Eq} defined and calculated from the permeability of the corresponding case can properly quantify rarefaction effects. The corresponding permeability values already

include the rarefaction effect and calculating the Knudsen number from this permeability provides a proper characteristic height for the gas flow. However, in the usual case, permeability values are unknown. In the calculation of apparent permeability using Klinkenberg model, the Knudsen number as a function of apparent permeability itself was included, and Klinkenberg constants were determined from numerical calculations. This developed a third-degree polynomial function which has been solved for apparent permeability calculation in the previous chapter.

4.3. Conclusion

Rarefied gas flows behaviors were investigated through multi pore structures. It is observed that, similar to the previous findings, the increases of slip velocity on surfaces resulted in lower pressure drops compared to continuum flow. Hence the permeability values increase. On the other hand, the existence of intraparticle pores through the main flow direction caused the reduction of permeability in most cases compared to mono-scale porous media. For such cases, intra pores created more friction forces towards the fluid path. However, there is a critical value of throat size where the permeability is higher than mono-scales. In these cases, it is observed that when the throat becomes comparable in size with intraparticle at high rarefaction levels, the permeabilities reach higher values. Next, the new definition of Kn number was tested on multi pore porous medium. In Kn calculations, porosity, pore connectivity, and intraparticle pore distribution were considered. The equivalent diameter-based solution showed that permeability variation is only a porosity function, independent of other structural parameters. In such cases, Klinkenberg constant becomes a linear function of porosity. By calculating the equivalent diameter from apparent permeability, it is possible to apply the extended phenomenological model given in the previous chapter onto current results with an excellent agreement.

CHAPTER 5

GAS SLIP FLOW IN THREE-DIMENSIONAL POROUS MEDIA

Transport in porous media performs a vital role in numerous fields of science and engineering. Accordingly, quantitative pore-scale flow characterization of porous media has a fundamental importance in many areas such as composite materials[114,115], geophysics[116], petroleum engineering[117,118], soil science[119,120], and biotechnology[121]. Accurate estimation and prediction of such porous medium's single and multiscale transport properties is the concern of many research in these fields. Several theoretical, numerical, and experimental studies have been suggested and developed to investigate fluid flow in such complex and heterogeneous porous media. Since field experiments and studies including SEM, X-ray, TEM and etc.[122–126], are generally expensive and time-consuming, simulating multiscale fluid flows becomes highly reasonable. Pore-scale simulations necessity is due to the fact that they can generate relatively precise and cost-effective predictions. Meanwhile, they allow for systematic changes of the system's parameters, such as fluid properties, pore space geometries, and boundary conditions, which are complex tasks to achieve with experiments.

With the growth of available computer power and development of numerical methods, three-dimensional flow visualization has attracted much attention[127–130]. In many cases, creating a three-dimensional model is the fundamental step to characterize the porous medium's flow properties. In actual porous materials, fluid flow at the pore levels take place within a complex three-dimensional (3D) system of pores. However, due to the lack of reliable techniques to create models for complex real porous material, characterizing transport through heterogeneous porous medium has encountered many difficulties. For example, in shale-gas layers or coal beds, it is particularly needed to consider the presence of a complex micro/nano fracture network[83,131]. There are several models established in the literature to estimate the gas permeability in complex three-dimensional structures[132–135]. Warren and Root's (1963)[136] dual-porosity (or double-porosity) model is one of the methods which received much attention because of being practical and simple in use. This model showed the idealized system of inline combination

of cubic matrix blocks with fractures, as depicted in Figure 5.1. Several studies have shown that this simplified form of dual-porosity and homogeneous model can successfully explain many experimental observations in two- and three-dimensional of an actual heterogeneous naturally fractured system[137–140].

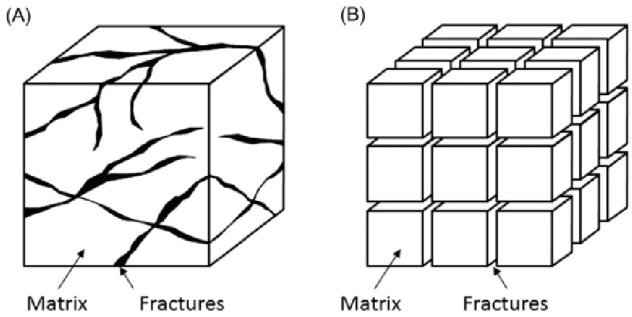

Figure 5.1. (a) Real reservoir system (b) idealized fracture model[141].

Flow in porous media occurs over a vast range of length scales. In micro/nano scales, gas flow deviates from the continuum approach, so different physics needs to be considered. New transport physics such as velocity slip, rarefaction and thermal jump at the solid-fluid boundaries are present in micro/nano-scale gas flows. When the Kn value becomes larger than 0.01, the gas permeability differs from its intrinsic value. In porous media at slip flow regime ($0.01 < Kn < 0.1$), this discrepancy was first observed by Klinkenberg and later studied by many others as a function of Kn in various forms.

Since it is easy to characterize gas dynamics using Kn, it is essential to properly describe the characteristic pore size for the complex structures of the porous systems. Previous efforts used REV size or hydraulic diameter as the characteristic length[142–144]. Additionally, these studies predict that gas permeability depends solely on porosity and pore size distribution, which fails to correct Kn values and gas dynamic characterization. However, in this study the Kn number is defined based on an equivalent diameter which depends on apparent gas permeability. In this way, besides porosity and REV size, pore connectivity effects were also involved in calculating the Kn number. Moreover, it is observed that the calculated Kn numbers were in the form of Klinkenberg's theory.

Following from chapter three, which described a new approach to make predictions of correct Kn number, the pore space was constructed in a three-dimensional structure in this part of the study. Pressure-driven incompressible gas flow through three-dimensional REV is numerically investigated by solving Navier–Stokes equations coupled with first-order slip boundary condition. Once again, it is observed that the

proposed model is also valid for the three-dimensional set of data with a very good agreement.

5.1. Simulation Details

A Representative Elementary Volume is considered a three-dimensional network of the porous system, as shown in Figure 5.2. The REV was measured with $H_{Darcy,}$ which has an equal dimension in all directions. The REV has shown in Figure 5.2(b) contains an eight-unit cell with a highly ordered packed structure. Here the size of solid particles was denoted by $D_{(xyz)}$ while the porosity (ε) is given as the ratio of void volume to total volume of structure. Another critical geometrical parameter that relates pore throat to pore size is also introduced. This parameter demonstrates the pore connectivity layout in the porous medium even if the porosity does not change. In this part of the study, simulations were conducted by varying two geometrical properties: porosity (ε) and pore size to throat size ratios (R_{pt}). Porosity was changed by modifying the length of the solids in three-dimensional as the size distributions of solid parts defined the pore to throat size. Since the main flow takes place only in the x-direction, the pore to throat size was equally changed in the y and z direction.

Air with a dynamic viscosity of 18.21×10^{-6} kg/ms is flowing through the porous media. For different rarefaction levels, the air density was varied to obtain different Kn values. Low-velocity flows were studied to remain in the Darcy flow region with negligible inertial effects. The gas flow is assumed to be in incompressible region while steady state condition is considered. For all simulations, temperature and other thermophysical properties were assumed to be constant. Steady forms of the continuity and momentum equations were solved to determine the velocity fields using the ANSYS Fluent finite volume code. Symmetry boundary conditions were applied on each side, and periodicity conditions were applied on REV's inlet and outlet boundaries. Since the flow is in the fully developed region, the “end effects” that might be developing in short channels were neglected. The slip velocity boundary condition was applied on solid surfaces with a unity momentum accommodation coefficient, assuming diffuse reflections.

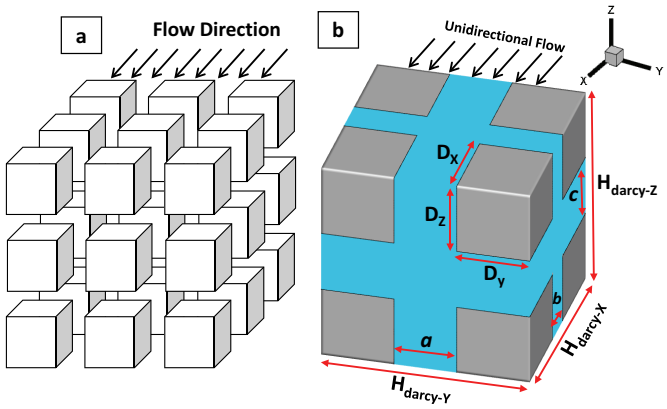

Figure 5.2. a) Schematic illustration of domain b) Simulation domain as a Representative Elementary Volume (REV).

The numerical simulation domain is one-fourth of the above figure since the remaining parts are in symmetry sides.

5.2. Results and Discussions

The study started by solving the velocity distributions for porosity values between 0.2 and 0.8 with a changing pore to throat size ratios. The domain shown in Figure 5.2 is studied where the throat size was varied between 2 to 11. The velocity contours presented in Figure 5.3 were shown at the constant porosity $\varepsilon = 0.6$. In Figure 5.3, each row has the same R_{pt} value with increasing rarefaction effects. To compare the velocity profile of different cases in the same range, the velocity profiles were normalized with their corresponding average values. A strong slip effect is clearly observed for all cases in the last column where $Kn_{Darcy} = 0.03$. Increasing R_{pt} at constant porosity creates tight pore throats in y and z directions while fixing up wider pore space in the axial direction. Therefore, penetration of flow between pores in the main flow direction at high R_{pt} cases generates secondary flows that substantially interrupt the main flow patterns. In this region, the secondary flows yielded different shapes and variations of streamlines, while at low R_{pt} cases, the streamlines were even more flattened resemble the straight channel flows. In these cases, it can clearly distinguish that characterization of flow based on porosity is not sufficient since different flow distributions developed regardless of constant porosity. Another factor that has an important effect on the velocity patterns is rarefaction. Due to the velocity slip developed on the surface as Kn increases, less

velocity gradients and more uniform velocity distributions in pore throats were observed. These flow enhancements are due to the gas slippage effect near pore surfaces resulting gas velocity along the throat center reaches to its maximum value.

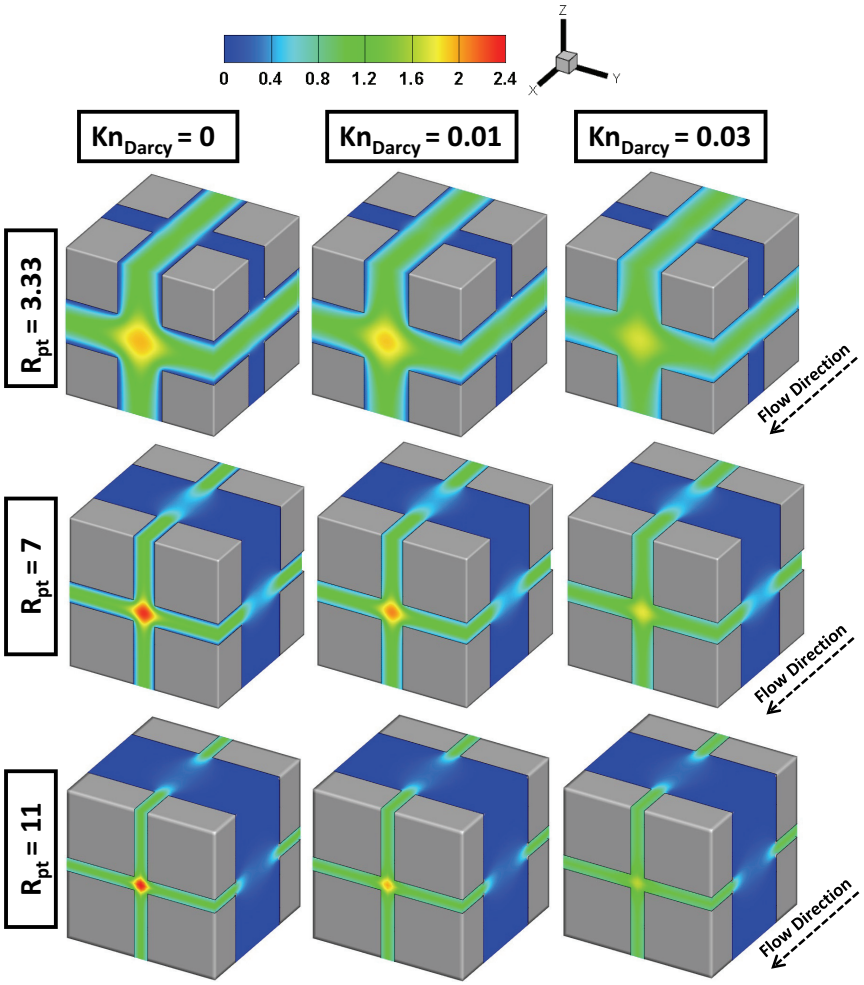

Figure 5.3. Velocity contours of ε = 0.6 porosity cases at different pore to throat size ratios and rarefaction levels.

In order to understand the pore connectivity and rarefaction effect on transport, the normalized permeability values were plotted in Figure 5.4. In all cases, the permeability values were calculated based on Darcy's law which is given in Equation (2.8). Two separate mechanisms have an essential effect on permeability variation for different porosities (ε = 0.2, 0.4, 0.6, 0.8). The first mechanism depends on geometry which is porosity and pore to throat size ratios. An increase in porosity resulted in higher permeability values, while an increase in R_{pt} decreases permeability values in every case. For instance, by comparing the specific case of ε = 0.6 at two R_{pt} values of 3.33 and 11, 22 times difference in permeability was observed. This shows that with increasing R_{pt}, the pore throat effect becomes more dominant on the flow parameters, while at low R_{pt}

values, the throat effect vanishes away from the main flow (x+) direction. The second mechanism is the rarefaction effects. By increasing the magnitude of Kn, permeability values increase. 153% increase in permeability at $Kn_{Darcy} = 0.03$ with $R_{pt} = 11$ and $\varepsilon = 0.4$ was observed, showing the importance of slip in gas flows. Overall, an increase in porosity and Kn with a decrease in R_{pt} yielded higher permeabilities.

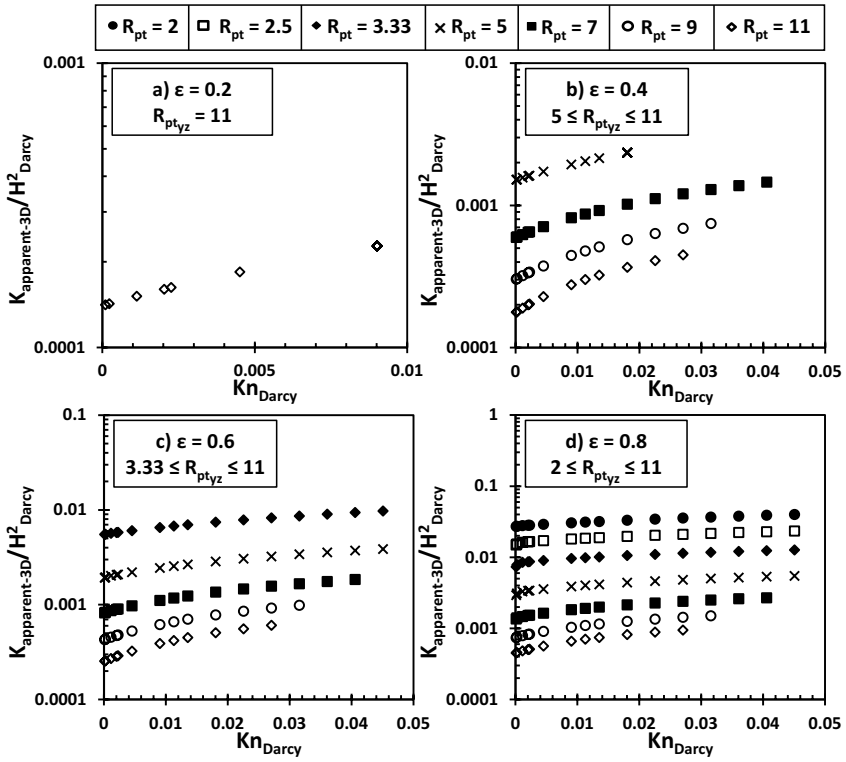

Figure 5.4. Non-dimensional Permeability values of different porosity and pore to throat size ratio values at different rarefaction levels described by Kn_{Darcy}

In Figure 5.5, apparent gas permeability normalized with corresponding intrinsic permeability is represented at given porosity and pore to throat size ratios. On the order of the Kn_{Darcy}, higher Kn effects develop at higher R_{pt} cases representing tighter systems. However, since Darcy length is an average representative size in the porous medium, this definition is not sufficient to characterize the rarefaction and pore connectivity together in one system. Hence the new description of Kn is required to capture these behaviors on permeability properly. Additionally, the impact of secondary flows take place between pore voids should be appropriately included. This can only be applicable in porous media by defining an equivalent diameter from the corresponding gas permeability value. More detailed analysis of equivalent diameter definition can be found in chapter 3. The main goal of the current study is to show that it is possible to characterize and combine the

effect of R_{pt} with rarefaction in three-dimensional flows, as depicted in Figures 5.6 and 5.7.

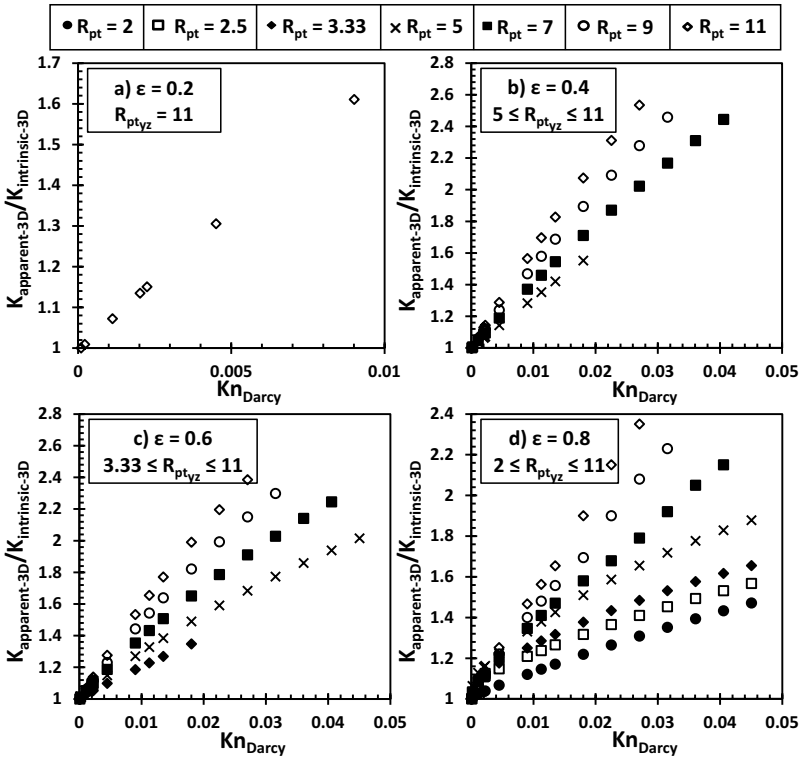

Figure 5.5. Permeability values of different porosity and pore to throat size ratio values normalized with corresponding intrinsic permeability at different rarefaction levels described by Kn calculated from Darcy height.

New defined Kn_{Eq} results were presented in Figure 5.6 as function of normalized permeability. Different than Kn_{Darcy} definition, calculation of equivalent length based on permeability showed that at specific porosity and various R_{pt} cases the results were lined up and appeared in a collective form. Thus, the R_{pt} can be ignored from results while the permeability showed quasi-linear change by the variation of Kn_{eq}. Additionally, the logarithmic form of the current results is shown in Figure 5.7. Particularly at low R_{pt} values, results were accumulated in a small Kn_{eq} region which, for better envision and scattering data along the x-axis, the logarithmic scale was selected. Next, the mathematical fits were applied individually for different cases. Resulted functions were given on each figure with the corresponding R-squared value for regression. Except in the high porosity case of $\varepsilon = 0.8$, linear fits showed a perfect match with numerical data. Deviation from linearity in $\varepsilon = 0.8$, especially at low R_{pt} values, can be explained by the fact that at this porosity, 80% of the total volume is occupied with fluid. Hence, the numerical errors and uncertainties in these regions were more likely to occur during the computational process.

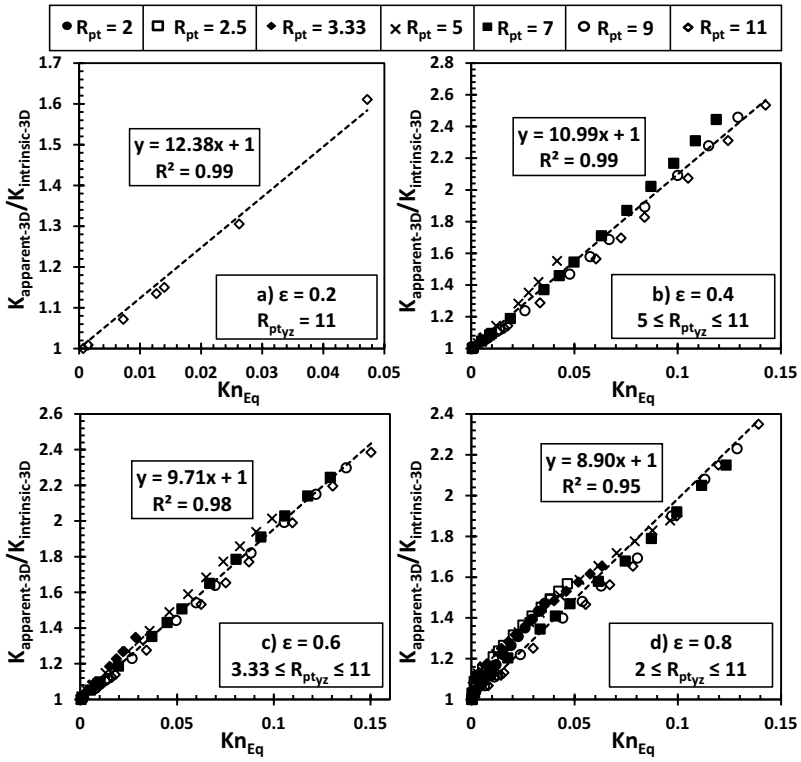

Figure 5.6. Normalized permeability values of different porosity and pore to throat size ratio values at different rarefaction levels described by Kn calculated from equivalent diameter.

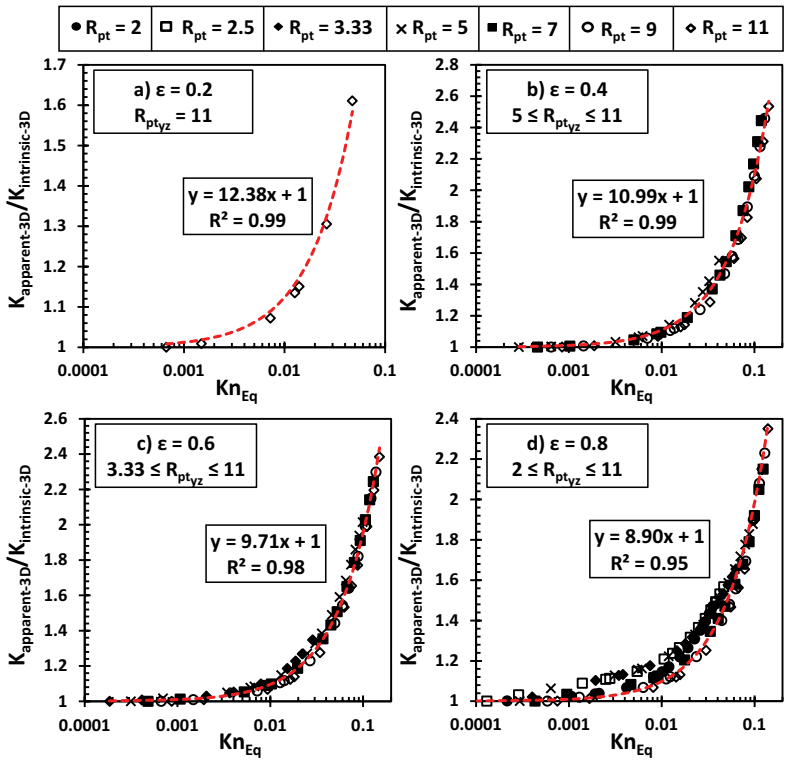

Figure 5.7. Normalized permeability values of different porosity and pore to throat size ratio values at different rarefaction levels described by $Kn_{Eq.}$ (Logarithmic format).

The linear form of equations found in Figure 5.6 is very similar to linear Kn dependence suggested by Klinkenberg. The slope of the linear fits only dependent on porosity and independent from R_{pt}. Thus, plotting these values related to porosity and applying an appropriate mathematical fit makes it possible to estimate the Klinkenberg constant. Different from Klinkenberg's original assumption, which predicted C_k as a constant value ($C_K \approx 4$), the Klinkenberg constant by porosity variation was plotted in Figure 5.8. Klinkenberg constants given in this figure were calculated by employing a linear fit with high accuracy of R-square value of 0.98. In these cases, by increasing the porosity, a decreasing linear trend is observed for C_k values.

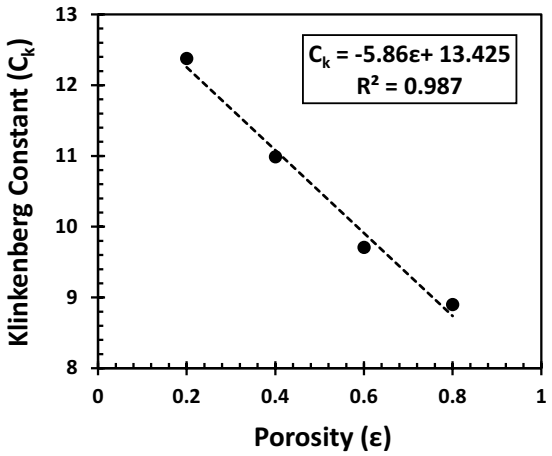

Figure 5.8. Klinkenberg constants at different porosities.

Current results showed that the model suggested in Equation (3.18) can successfully be employed on the three-dimensional porous system at various geometrical and slip conditions. By modifying the value of C_k for three-dimensional flow, the solution of Equations (3.19) and (3.22) provides the apparent gas permeability in terms of porosity, Darcy length of the porous system, intrinsic permeability (Kn = 0), and Kn_{Darcy} as an extension of the Klinkenberg model.

Finally, the model is validated with numerical results in Figure 5.9. The solid symbols show the simulation results where the red lines are the calculations from the mathematical equations. Hence, the proposed model can predict the results with a high accuracy between the numerical results and the apparent permeability solutions from the extended Klinkenberg model.

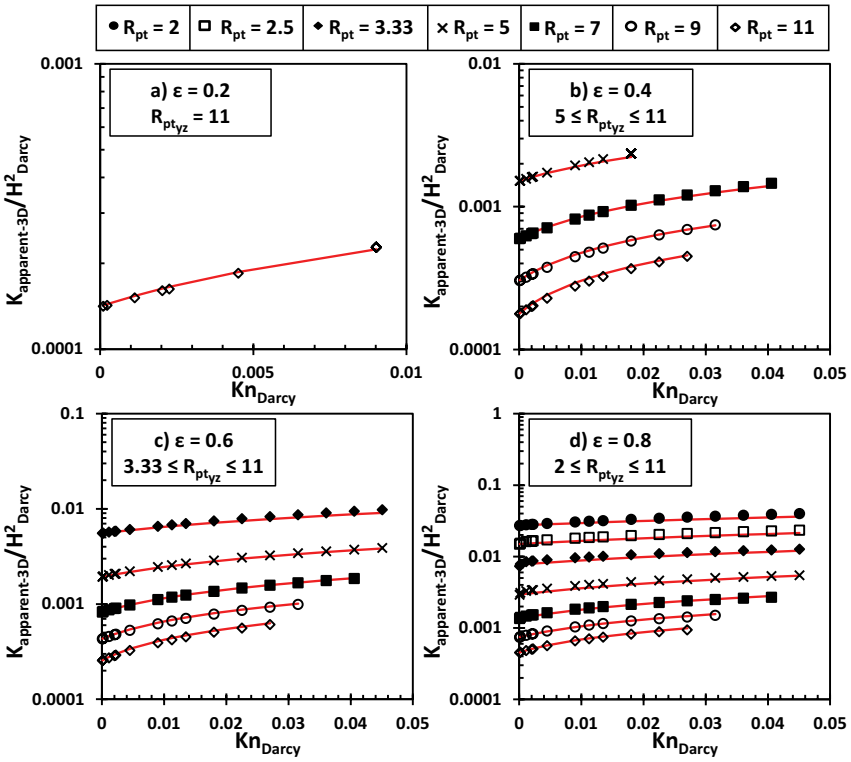

Figure 5.9. Comparison of the permeability predictions of mathematical model with the numerical calculations.

5.3. Conclusion

Three-dimensional simulations have been undertaken on gaseous slip flow through a set of orthogonal cubic blocks at different porosity, pore throat ratio, and various Knudsen numbers. Different geometrical dimensions and solutions conditions were studied. The enhancement of flow due to rarefaction was observed in terms of increased permeability values. The variation of permeability with respect to the Kn number calculated from the H_{Darcy} showed dependence on both porosity and pore to throat size ratio. Instead, an equivalent diameter as a function of the apparent gas permeability of the corresponding system was calculated. It is observed that the change of permeability became only the function of porosity when the Kn number calculated as a function of an equivalent diameter. The results calculate in this way were independent from pore connectivity or other geometrical effects and were in the form of Klinkenberg's linear model. Similar to previous findings, it is concluded that the mathematical model proposed based on Klinkenberg's theory for two-dimensional flow can be successfully adapted to three-dimensional flow where good agreements were observed in all cases.

CHAPTER 6

THERMAL AND HYDRODYNAMIC BEHAVIOR OF FORCED CONVECTION GAS SLIP FLOW IN A KELVIN CELL METAL FOAM

In recent years, open foam structural materials which belong to the class of porous medium were frequently used as reliable materials to enhance transport in thermal and hydrodynamic systems[145]. Application of these materials can be found in many fields such as chemical filtration[146], flame arresters[147] and renewable energy systems[148]. In addition, the high thermal conductivity of metal and the large contact surface area per unit volume between solid and fluid creates further advantages for heat transfer applications, mainly in thermal management of electronic components[149] and high-performance heat exchangers[150]. However, an accurate characterization of primary fluidic and thermal properties of gas transport through these functional materials is still missing.

Metal foams are synthesized in various pore sizes and porosities and work at various pressures. Gas rarefaction is characterized by the Knudsen number (Kn) as the ratio of molecular mean free path to characteristic length. With an increase in Kn, gas flow deviates from the continuum behavior at different levels. For moderate Kn values ($10^{-2} < Kn < 10^{-1}$), non-equilibrium mostly remains near the boundaries such that the non-continuum can be accounted for by temperature jump and velocity slip boundary conditions. Such gas rarefaction develops in the case of metal foam with ~6μm average pore size and smaller working at standard conditions (100kPa and 300K) or case of metal foam with ~0.3mm average pore size working at 2kPa and lower. The conventional conservation of momentum and energy equations are applicable in this rarefaction level called “slip flow regime” using the modified boundary conditions.

In literature, rarefaction effects on fluid flow and heat transfer are investigated widely for channels and tubes[91,151–154]. Specific for porous systems, hydrodynamic and thermal behavior of convective gas flows are characterized based on permeability values from the Darcy-Forchheimer model and interfacial heat transfer coefficient (h) through slip flow regime. Coupled momentum and energy equations are solved for micro-channels/tubes filled with a porous medium at various Kn values[155]. An increase in apparent gas permeability is observed for increasing Kn value[39], as described by

Klinkenberg correction. Researchers presented that the velocity slip developing on pore surfaces enhances the heat transfer while the temperature jump between solid and gas has a negative influence[156,157]. Depending on Kn values and system parameters, the overall effect of rarefaction reduces the total heat transfer[158]. Except for only a few studies[159–164], most of these studies were performed at a two-dimensional (2D) solution system. While a 2D system made of solid and fluid regions can represent a tube/channel bundle, the complex microstructures of a porous media and resulted flow features require a solution in a three-dimensional (3D) coordinate system.

In literature, the irregular and complex geometry of open-cell foams has been determined by micro-computed tomography (μCT) imaging to digitize the porous structures for pore-level computational fluid dynamic (CFD) analyses[165–167]. However, meshing the realistic open foam structure is very complicated, and the corresponding CFD simulations are computationally expensive[168,169]. Instead, researchers utilize idealized or simplified geometries of the samples as a representative elementary volume (REV) of the porous system. Ranging between a simple 3D cubic cell to a dodecahedron cell, literature studied various forms of unit structures[170,171]. Of these, the Kelvin cell model[172] with a tetrakaidecahedron cell shape with slightly curved faces was validated by numerous researchers as the most suitable idealized geometry to represent the real open-cell foam structure.

Kelvin cell model has been utilized for the understanding of heat and mass transport in metal foams. Researchers calculated pressure, velocity, and temperature distributions to calculate permeability and convective heat transfer coefficient of various foam systems with different pore sizes and porosities[173–176]. They validated that using metal foam enhances the heat transfer, but with an increase in the pressure drop[150]. However, no study characterizing the rarefaction in metal foams using the Kelvin cell model exists yet.

According to the comprehensive literature review, the novelty of the present study shows that there are no studies yet completely characterize the transport properties of gas flow in open-cell metal foams at slip flow regime. In this study, a numerical solution was performed to evaluate convective gas flows accurately through highly ordered metal foam structures at varying porosities and rarefaction levels. The results provided more accurate transport values such as permeability and heat transfer coefficient, two important parameters useful for many engineering applications. The main contributions of this study

by investigating the characteristics of slip flow and temperature jump in the system with ordered Kelvin cell metallic foam structure are as follows:

- characterize the effects of velocity slip, temperature jump, and structure of the porous media on the performance of flow and heat transfer
- Quantify the effect of geometrical and operating parameters on transport performance at the cell level
- Propose accurate correlation to find the thermal performance of foam structure for a specified range of porosity at slip flow regime.

6.1. Simulation Details

The open cell structure of the metal foam is described using the Kelvin cell geometry[177], as shown in Figure 6.1(a). The three-dimensional convection system is given by the Representative Elementary Volume (REV) presented in Figure 6.1 (b). The number of pores per inch (PPI) in this study was selected as 80 for six different porosity values. The geometrical description for the Kelvin cell structure is given in Figure 6.1 (c), where L_c is the cell length and d_s is the strut (fiber) diameter. The characteristics of the porous metal structures were obtained from the correlations given in the work of Lucci et. al.[178]. The Kelvin cell geometries were created using the Surface Evolver software[179].

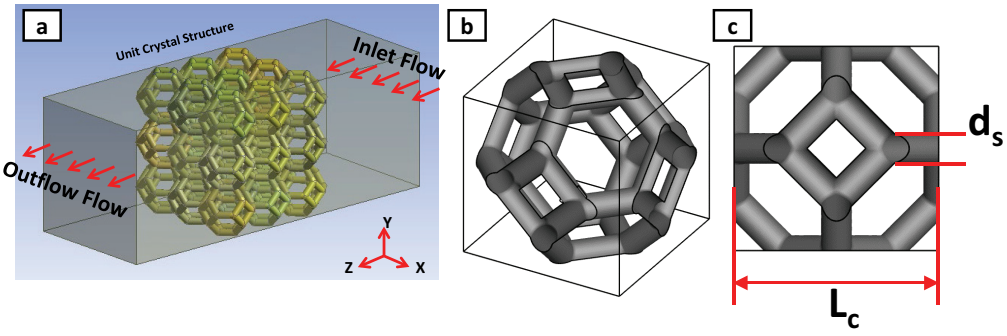

Figure 6.1. Illustration of (a) metal foam structure, (b) Representative Elementary Volume (REV) for Kelvin cell model, and (c) geometric parameters.

A steady-state, incompressible, and laminar flow with negligible buoyancy forces was considered. The periodic boundary condition was applied along the main flow direction (z-direction), while symmetric boundary conditions were considered for other

directions. Since the flow is in the thermally and hydrodynamically fully developed region, the effect of viscous dissipation on heat transfer is neglected.

An outflow condition was considered at the outlet while different pressure values at the inlet were applied to create flow in the z-direction at different velocities. First-order slip velocity and temperature jump given in Equations (2.18) and (2.19) were applied on solid surfaces. In these equations, σ_m is the tangential momentum accommodation coefficient, σ_t is the thermal accommodation coefficient, and γ is the specific heat ratio.

To calculate the numerical result with high accuracy, the mesh independency test is carried out. Several attempts to find an optimum mesh size were performed until the error between consecutive mesh results drops to less than 1%. In this study, the grid with 276685 elements is selected for all simulations, which represents the best solution for accuracy, computational time, and convergence.

Table 6.1. Mesh independency analysis

Grid	Total #Nodes	V_{Darcy} (m/s)	% error	h (W/m^{2}K)	% error
Mesh 1	53776	1.58	6.28%	688.90	4.64%
Mesh 2	108569	1.54	3.12%	675.86	2.66%
Mesh 3	***276685***	***1.50***	***0.75%***	***664.52***	***0.94%***
Mesh 4	582221	1.49	-	658.36	-

Next, the validation of the numerical procedure was done by comparing our results with the literature. As shown in Figure 6.2, there is a good agreement between the computational result for Nu as a function of Peclet number of the current work and selected studies in the literature[180,181].

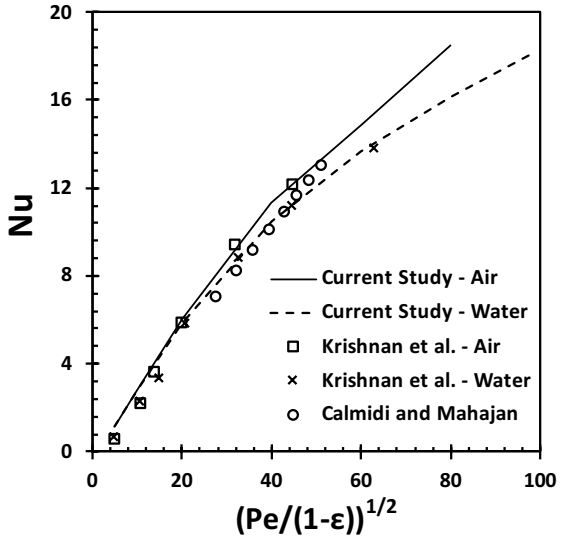

Figure 6.2. Current findings were compared with the values from the literature.

6.2. Results and Discussions

6.2.1. Constant Thermophysical Properties

Air is flowing through the porous media with a dynamic viscosity of 17.89×10^{-6} kg/ms. For different rarefaction levels, the air density was varied to obtain different Kn values. In this part of the study, air was assumed to have constant thermophysical properties while a constant low heat flux condition was applied on the boundaries.

Velocity contours in a single Kelvin cell are illustrated in Figure 6.3. The velocity profiles were normalized by average velocity measured at the corresponding case. The increasing effect of rarefaction as the increasing velocity slip on the strut surfaces can be observed for both highest and lowest porosity cases by increasing Kn value. In no-slip cases, the maximum velocity was developed in the center and corner of pores. The increase in rarefaction level led to decrease in core velocity and increase in surface slip. Therefore, lower velocity gradients and more uniform velocity distribution were developed inside the REV. In such cases, reduction in friction with increase in velocity yielded increase in permeability values.

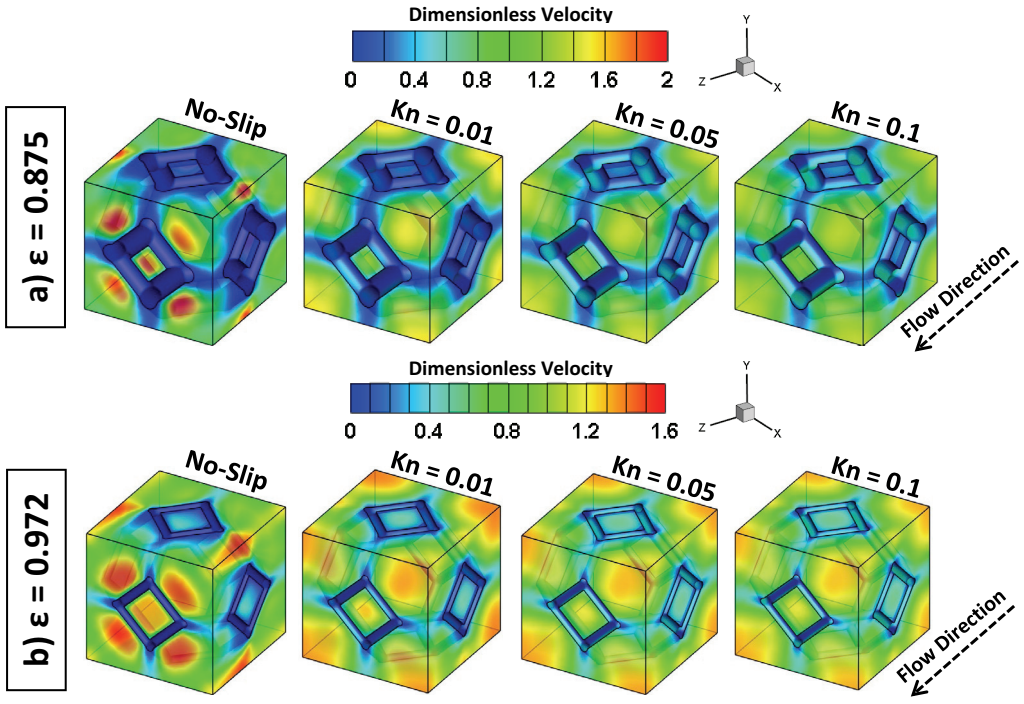

Figure 6.3. Dimensionless velocity contours of (a) ε = 0.875 and (b) ε = 0.972 cases at four different rarefaction levels.

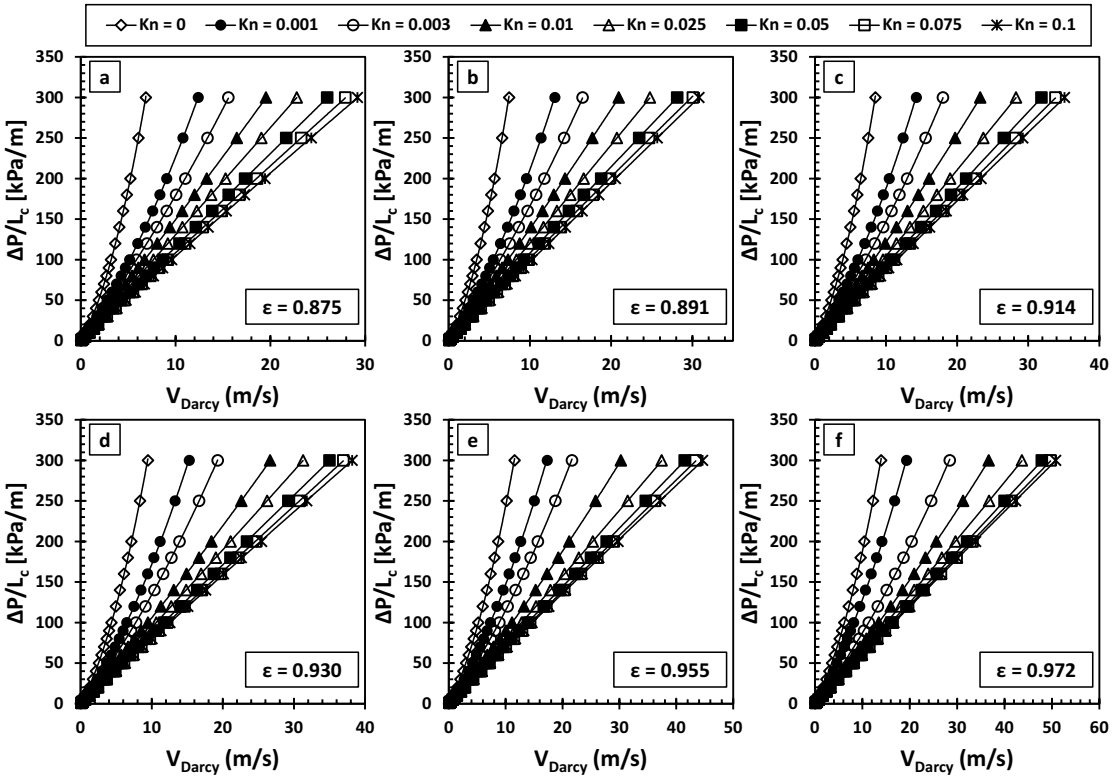

Figure 6.4. Pressure drops as a function of Darcy velocity at different Kn values.

Figure 6.4 shows the pressure drops through the porous systems with respect to resulted Darcy velocities. Each individual graph gives Kn = 0 results followed by increasing rarefaction up to Kn = 0.1. Herein, the Darcy velocities (average velocity) were computed with respect to average fluid velocity and porosity ($V_{Darcy} = V \times \varepsilon$). As expected, an increase in porosity, pressure drop, and Kn value resulted in a considerably higher velocity value in the Kelvin cell structures. As shown in Equation (2.9), the pressure drop develops as a function of the viscous (V) and inertial (V^2) terms. At Kn = 0 cases, increasing flow velocities developed a strong inertial effect generating nonlinearity between pressure drop and flow rate. However, by increasing the Kn value, the variation of velocity by pressure became more linear. This behavior was due to gas slippage on the strut surfaces, which created a decrease in drag forces. Hence, inertial forces' contribution to transport disappeared as the rarefaction level increased in this weak inertia regime. Generally, in porous systems, the effect of inertial forces is characterized with respect to Reynolds number, which is provided in Figure 6.5. In Figure 6.5, by applying an appropriate curve fitting of dimensionless pressure drops (Π) with respect to Re and utilizing the non-dimensional form of Forchheimer model [Equation (2.23)], permeability and inertia coefficient values were calculated at six different porosities. At negligible Re values, the dimensionless pressure term on the left side of Equation (2.23) simply leads

to the constant permeability of Darcy region represented by the first term on the right-hand side of the equation (Λ). The linear variation between velocity and pressure converges to this constant permeability. For finite Re values, inertial flow effects lead into non-linear variation of velocity under a given pressure drop as a function of Re number. For such a case, the formation of non-Darcy effects is not only determined by the Forchheimer coefficient but also by the corresponding permeability value, as described by the last term of the right-hand side (Γ).

For slip cases, the fit values were shown and extended up to Ma < 0.3. In this study, the speed of sound is approximately assumed to be 343 m/s. In this case, for Mach values smaller than 0.3 where the incompressible assumption will be valid, the maximum fluid velocity could reach up to 103 m/s. In all cases reported in this study, the corresponding maximum fluid velocity calculated in the structure is less than 70 m/s. Moreover, maximum Reynolds numbers in the incompressible region with the rarefied gas flow were calculated based on the following equation, which related Mach, Re, and Kn numbers:

$$Kn = \frac{Ma}{\mathrm{Re}} \sqrt{\left(\frac{\gamma \pi}{2} \right)} \tag{6.1}$$

At lower rarefactions, the flow characteristics were strongly governed by Darcy extended Forchheimer law. In this region, the dimensionless pressure drop was linearly increased since the Forchheimer effects developed rapidly in the flow. However, as the Kn increased, the rarefaction created lower inertial forces that so-called Darcy region extended. At high rarefaction levels, the studied velocities from incompressible flow regime (Ma < 0.3) remained in the Darcy region. Here the dimensionless pressure drop values were almost constant and did not change with increasing the Re values. It is possible to observe the separation of flow from Darcy to non-Darcy regions with respect to critical Reynolds number as the curves start to bend. It is clear from the graphs that in most cases, the linearity of curves is disrupted after Re values exceed 10. It should be underlined here that Figure 6.5 is plotted based on Equation (2.23), which is the linear form of Equation (2.9). In Figure 6.5, x-axes were plotted in logarithmic format for better envisaging and comparing all Kn values, particularly at low Re values.

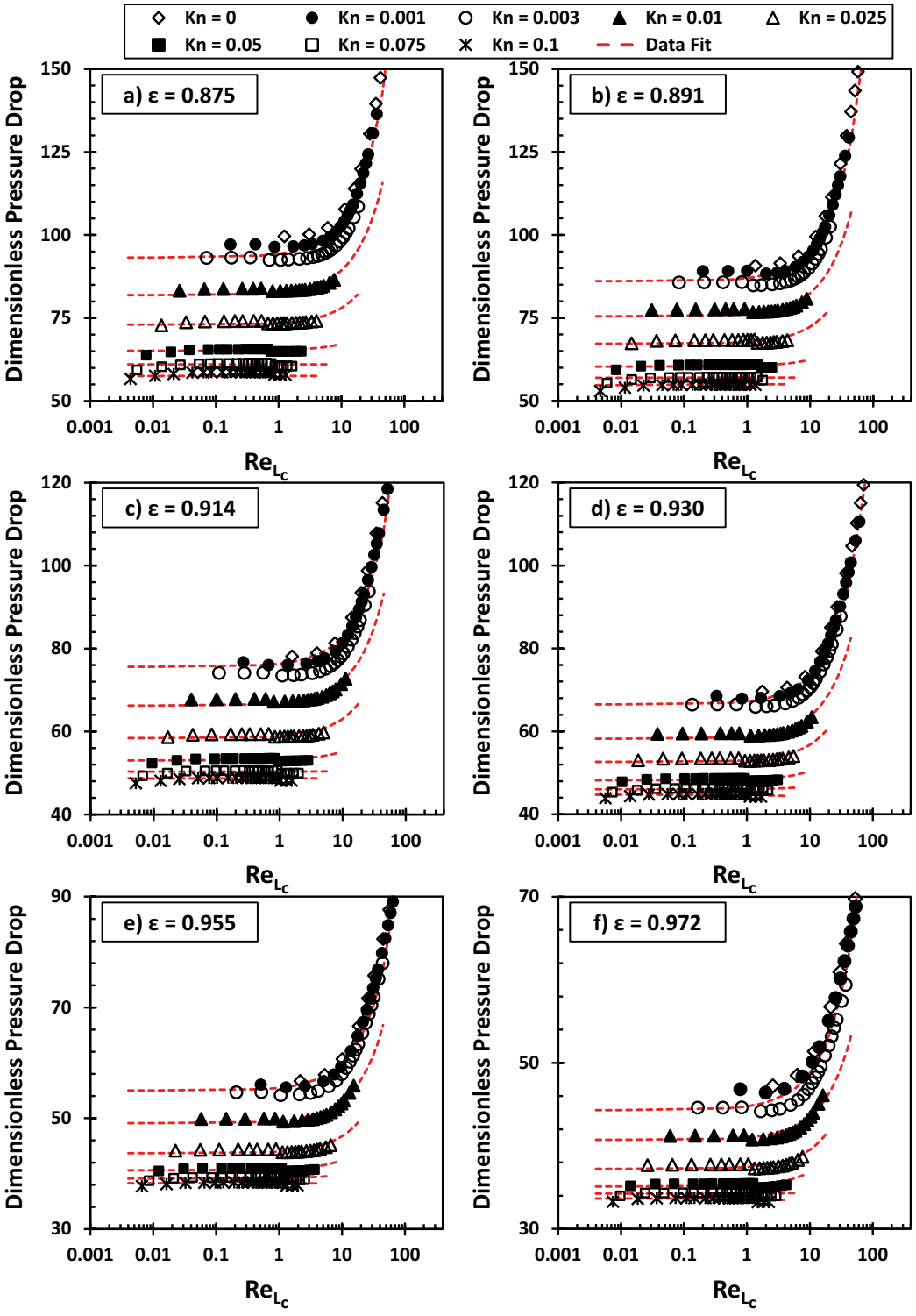

Figure 6.5. Dimensionless pressure drop as a function of Re at different Kn.

The normalized permeability values and Forchheimer coefficients calculated based on Darcy-Forchheimer equation are given in Figure 6.6. While permeability is the basic description of Darcy's theory, Forchheimer's coefficients include non-Darcian behaviors[182,183]. In Figure 6.6, the focus is on the effects of Kn number and porosity. The

cell size was used as the characteristic size of the system to normalize the permeability values in the Kelvin structure. As shown in Figure 6.6(a), a significant increase in permeability was observed for increasing porosity and Kn value. On the other hand, as shown in Figure 6.6(b), the increase in rarefaction reduced the inertial effects such that Forchheimer coefficients decreased substantially for all porosities. Specially at low porosity cases with high Kn number the inertial coefficients reach to the negligible value which can not be measured.

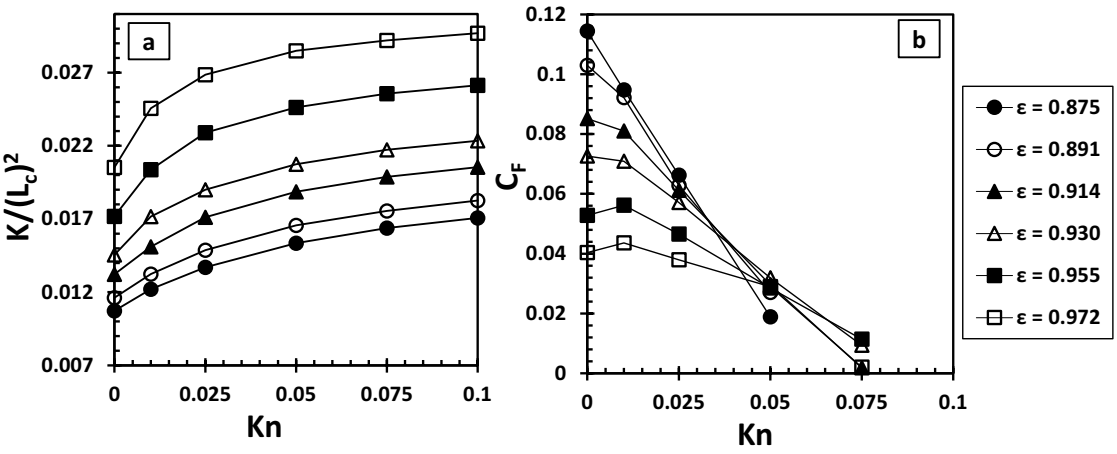

Figure 6.6. Calculated permeability and Forchheimer coefficients as a function of Kn number.

The permeability and Forchheimer coefficients normalized with the corresponding Kn = 0 values are given in Figure 6.7. As it was discussed earlier, permeability values increased by increasing Kn. This trend was observed for all porosity values. Specifically, at ε = 0.875 and Kn = 0.1, permeability reached to 60% of its Kn = 0 value. On the other hand, flow enhancement by rarefaction was lower at higher porosities. This was expected as the increase in porosity yielded less surface area that rarefaction had a lower influence. Figure 6.7(b) gives the normalized Forchheimer coefficients. Rarefaction yielded a substantial decrease in inertial effects, while its impact lessens by the increase in porosity. Under normal conditions, the tortuosity developing by increasing Re is the main source of inertial effects and drag forces, leading to a nonlinear increase in pressure drop by increasing flow rate. However, velocity slip due to rarefaction at metal foam surfaces created less distorted velocity fields and lower velocity gradients that the flow remained closer to the linear Darcy regime.

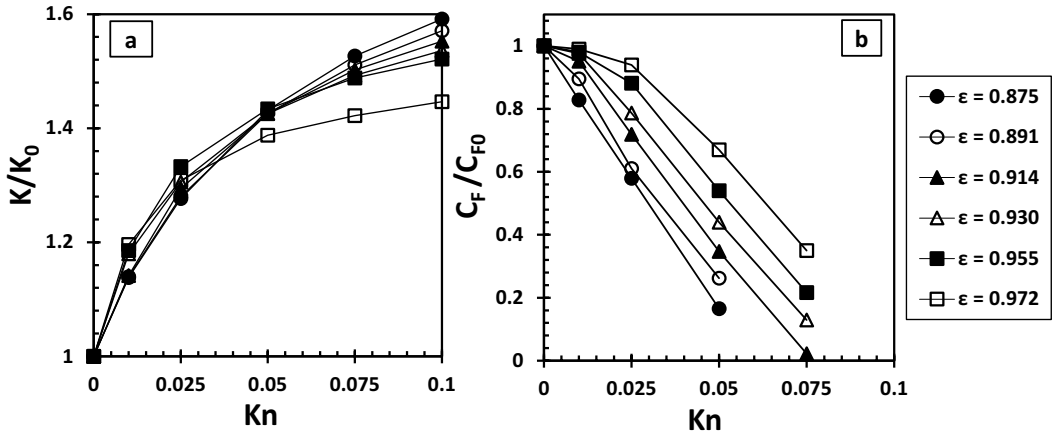

Figure 6.7. Normalized permeability and Forchheimer coefficients as a function of Kn at different porosities.

Next, temperature fields inside the metal foams are analyzed. The dimensionless temperature contour inside the highest and lowest porosities are given in Figure 6.8. The normalized temperature profiles were calculated with respect to the average wall gas temperature of each individual case based on the following equation:

$$\theta = \frac{T_f - T_{in}}{\left\langle T_{f-w} \right\rangle - T_{in}} \tag{6.2}$$

The dimensionless temperature in all cases was evaluated at the same mass flow rate and Re value. As expected, temperature increased from the inlet to exit uniformly through the structure. Due to the low heat flux regime, the temperature jumps were low, which created a slight decrease in convection by increasing rarefaction.

The Nusselt values for each porosity were calculated at different Re and Kn numbers. Due to rarefaction effects, the temperature jump between the strut surface and the bulk gas was developed. The variation of Nu values as a function of Re are given in Figure 6.9 for different porosity and Kn values. As expected, the Nusselt number increases with the growth of Reynolds number. While the increased permeability due to boundary slip had a positive effect on convection, temperature jump between the gas domain and the metal foam surfaces negatively affected heat transfer. This behavior resulted from a decrease in the interface temperature gradient as the temperature jump became more effective. The temperature jump is also known as thermal contact resistance between wall surface and gas. For the current application of highly conductive metal foam at low heat flux range, these two rarefaction effects almost canceled each other that Nusselt value became independent from Kn number.

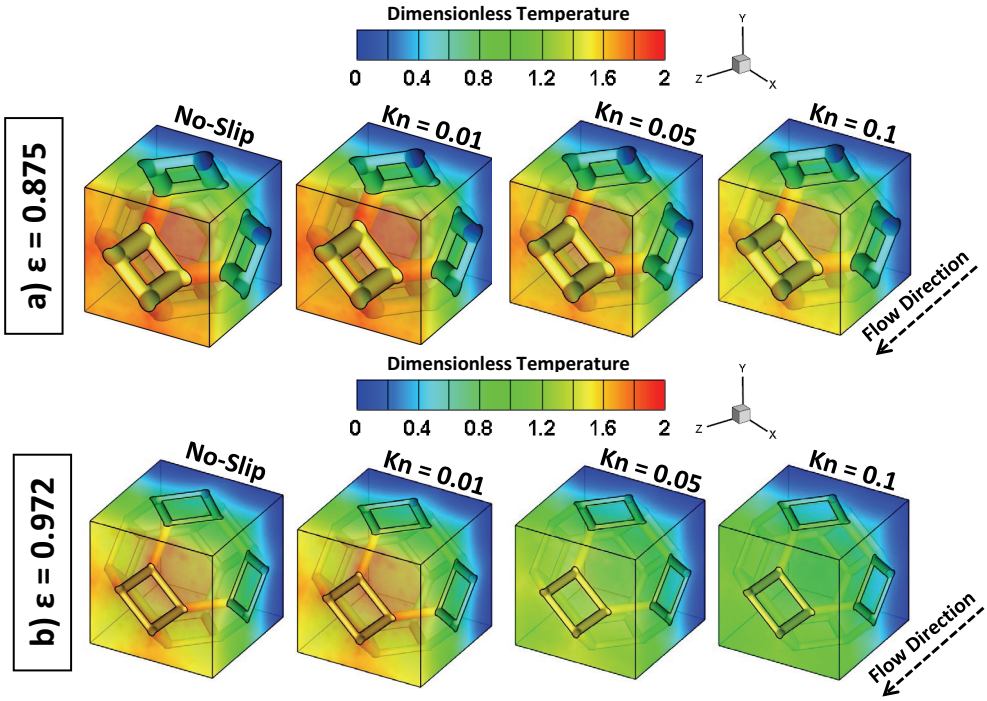

Figure 6.8. Dimensionless temperature contours of constant Re flows in (a) ε = 0.875 and (b) ε = 0.972 systems at different rarefaction levels.

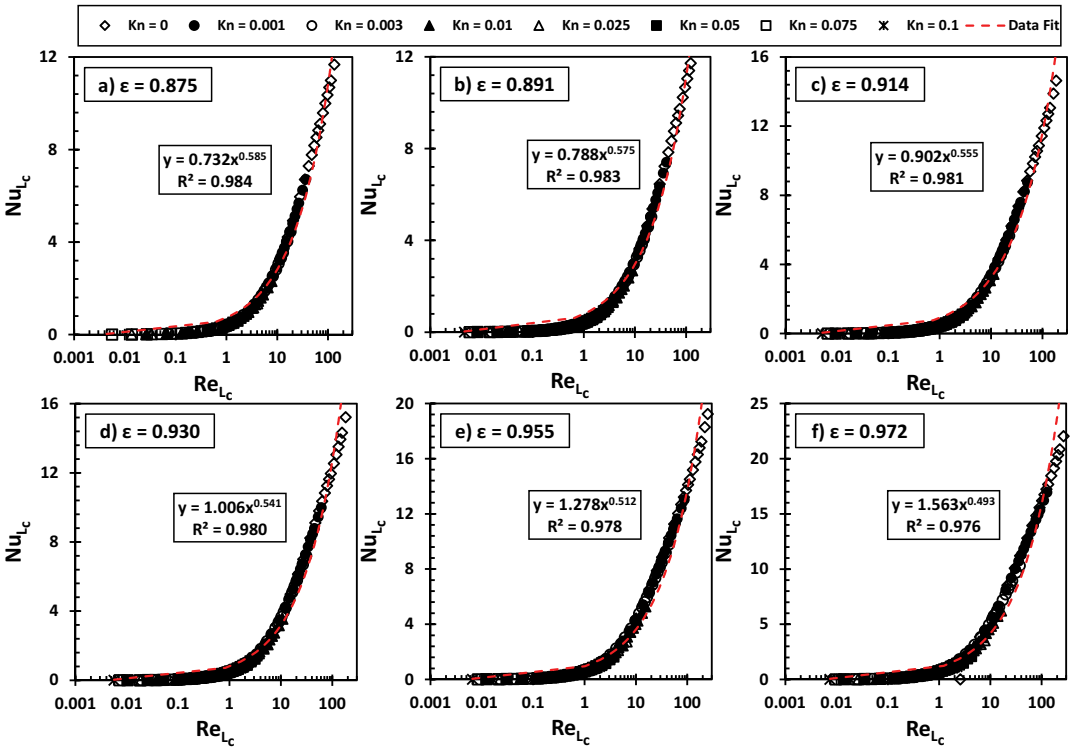

Figure 6.9. Nusselt values of Kelvin cells at different porosities and rarefaction levels as a function of Reynolds number.

Next, the variation of Nu number by the change in Re is considered. At higher porosity systems, Nu was found to increase stronger by increasing Re. Nu variation by

Re was described based on a power-law model ($Nu = A \times Re^B$) and applied mathematical fits on the results as shown in Figure 6.9. Mathematical models are given on each figure with the corresponding R-squared value for regression. Fits showed a perfect match with data for all porosity cases, while Nusselt numbers predicted by this method have an error value less than 5%.

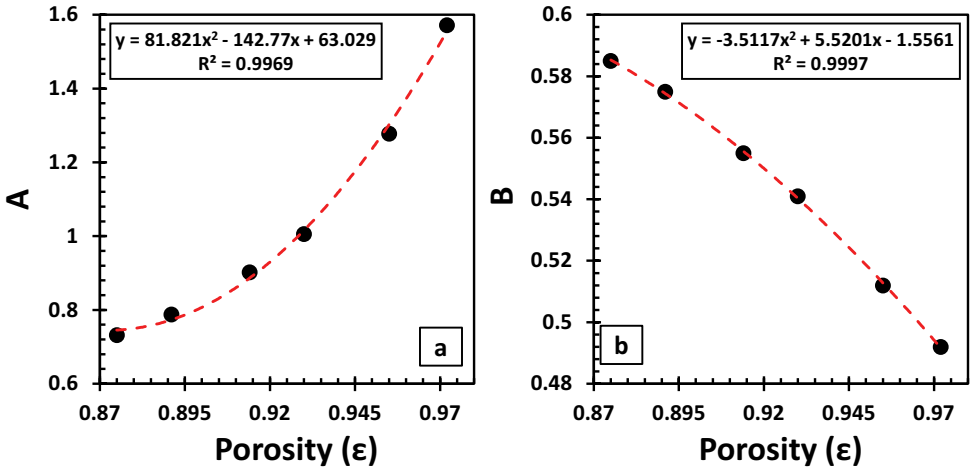

Figure 6.10. Constant coefficient at different porosities

Variation of mathematical model parameters by porosity was given in Figure 6.10. While the multiplier was increasing by porosity, the power over the Reynold decreased at higher porosities. Second-order polynomial fits are applied to these coefficients to characterize their variation with respect to porosity. Corresponding fits are shown in Figure 6.10. In the studied porosity range, the final form of the model describing the Nusselt number as a function of Reynolds and porosity became:

$$Nu = \left(81.821\varepsilon^2 - 142.77\varepsilon + 63.029\right) \mathrm{Re}^{\left(-3.5117\varepsilon^2 + 5.5201\varepsilon - 1.5561\right)} \qquad (6.3)$$

It was observed that for the low heat flux cases of highly conductive metal foam structures, the Nusselt numbers were primarily found related to Reynolds number independent of rarefaction. Hence, we were able to describe Nusselt number based on power-law model as a function of porosity and Reynolds number. Overall, the proposed model provides an accurate prediction for Nusselt number of all porosities.

6.2.2. Variable Thermophysical Properties with Different Heat Flux

In the last section, variable thermophysical gas properties dependent on temperature and pressure were studied. Second degree polynomial models given in Equations (6.4) and (6.5) were applied for calculations of viscosity and thermal conductivity while an incompressible ideal gas model was applied for density evaluations.

$$\mu(T) = 2.28797\times10^{-6} + 6.25979\times10^{-8}T - 3.13196\times10^{-11}T^2 \tag{6.4}$$

$$k(T) = 1.30030\times10^{-3} + 9.36766\times10^{-5}T - 4.44247\times10^{-8}T^2 \tag{6.5}$$

Since the temperature range is not reaching extremely high values, the variation of specific heat with temperature is assumed to be negligible, and a constant value of 1006.43 (J/kg.K) was considered. The numerical calculations were performed for two extreme porosity cases (ε = 0.875 and 0.972). In this study, only the results of Darcy region (low Reynolds) with Kn values between 0.001 to 0.1 were noted. To evaluate the variation of temperature, heat flux in the range of 10 to 6000 W/m^2 was applied at solid boundaries. Other boundary conditions were maintained similar to the previous section.

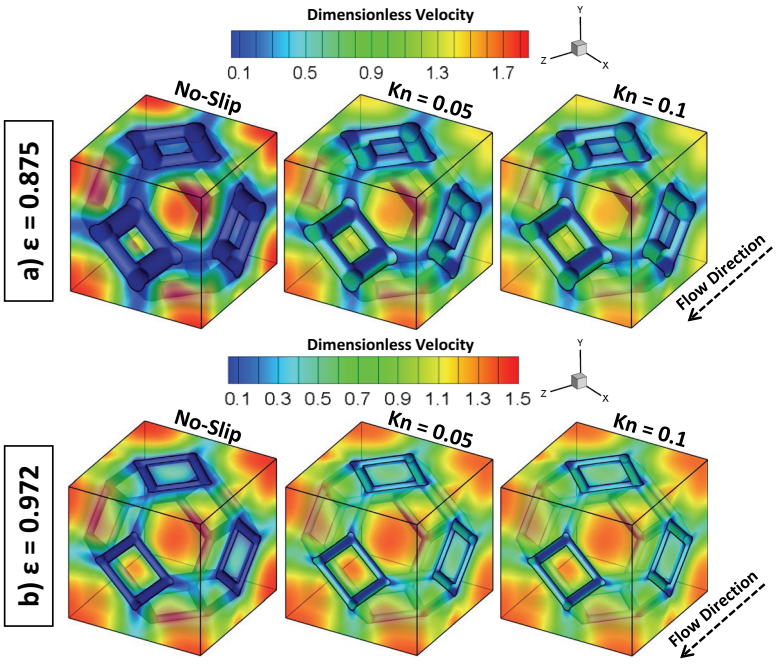

Figure 6.11. Dimensionless velocity contours at different rarefaction levels.

The investigations began by normalizing the velocity distribution shown in Figure 6.11 with each case's average fluid velocity values. The values were calculated at the same Re number in order to capture a similar behavior. As seen from the figure,

rarefaction led to a decrease in velocity gradient inside the REV. Therefore, friction coefficient decreases resulted in higher permeabilities.

Next, the dimensionless pressure drop with respect to Re is shown in Figure 6.12. It is observed that at different rarefaction levels by varying the heat flux and obtaining temperature gradient the dimensionless pressure drop is approximately remaining at the same values. These results are supported in Figure 6.12, where the permeability values are given as a function of average gas temperature.

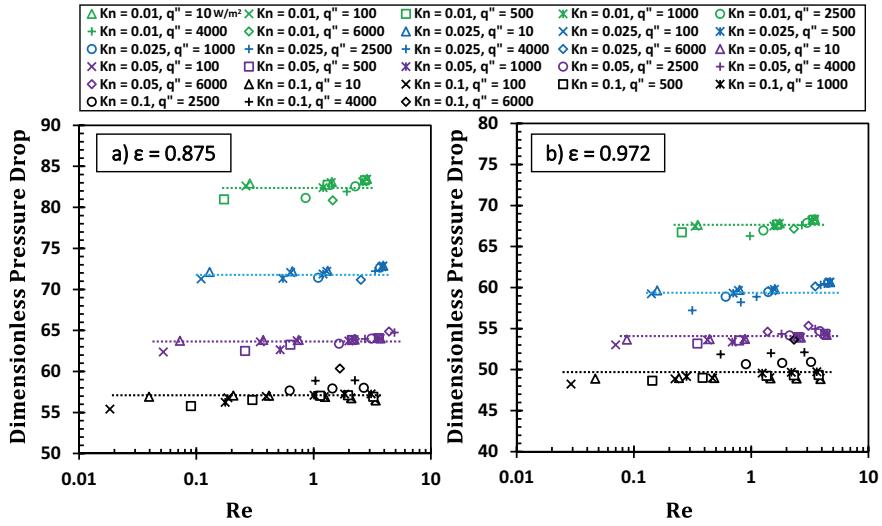

Figure 6.12. Dimensionless pressure drop as a function of Re, Kn, and heat flux (W/m^2).

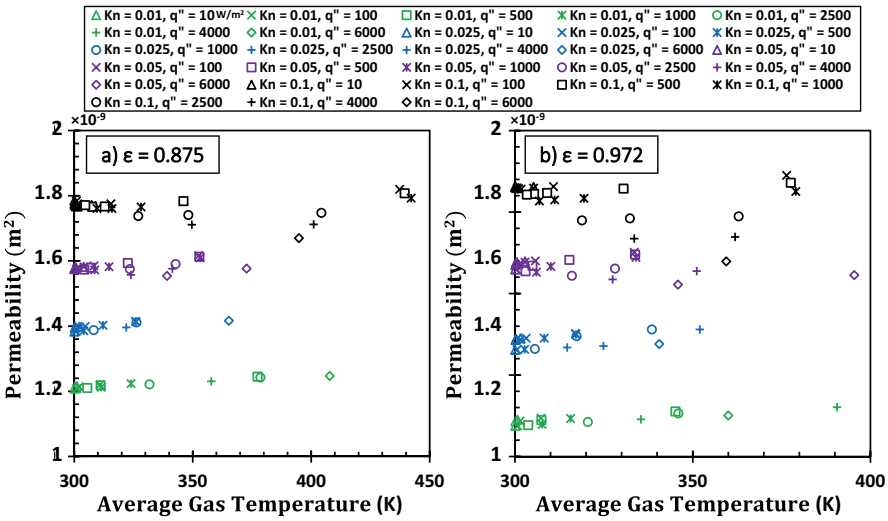

Figure 6.13. Permeability values based on variable heat fluxes (W/m^2) and Kn.

It is well known that in macro gas flows, permeability is an intrinsic property and independent from fluid properties in porous medium. However, in some cases, fluid properties such as viscosity, thermal conductivity, and density should also be included to characterize the porous transport. In such examples, permeability becomes inadequate to

describe the transport, so another parameter known as hydraulic conductivity is mainly utilized. Since the permeability of the system remains the same with temperature gradient, variation of hydraulic conductivity due to different flow conditions should be carefully investigated. The hydraulic conductivity is a material property that reflects the relative ease of fluid flow through porous media and is among the most variable material properties in engineering. In this regard, Hydraulic conductivity (h) can be obtained as follows,

$$\langle V \rangle = -\frac{h}{\rho_f g} \nabla P \tag{6.6}$$

where g is the gravity, ρ_f is the density of fluid, <V> is the volumetric velocity and ∇P is the pressure gradient.

As a next step, hydraulic conductivity values were estimated for considered porosity, rarefaction levels, and heat flux ranges by using Equation (6.6). Figure 6.14 shows the results of variations of hydraulic conductivity with respect to average gas temperature. It can be seen that hydraulic conductivity decreases linearly by increasing temperature. A general increase in the value of hydraulic conductivity is observed with increasing porosity. However, the decreasing trend is still maintained. Finally, Figure 6.15 is established by normalizing the hydraulic conductivity values with their value at T_f = 300K and corresponding Kn. This representation explains that hydraulic conductivity becomes independent of rarefaction effects and only as a function of temperature. The hydraulic conductivity decreases in all cases by increasing the temperature while the behavior remains almost linear.

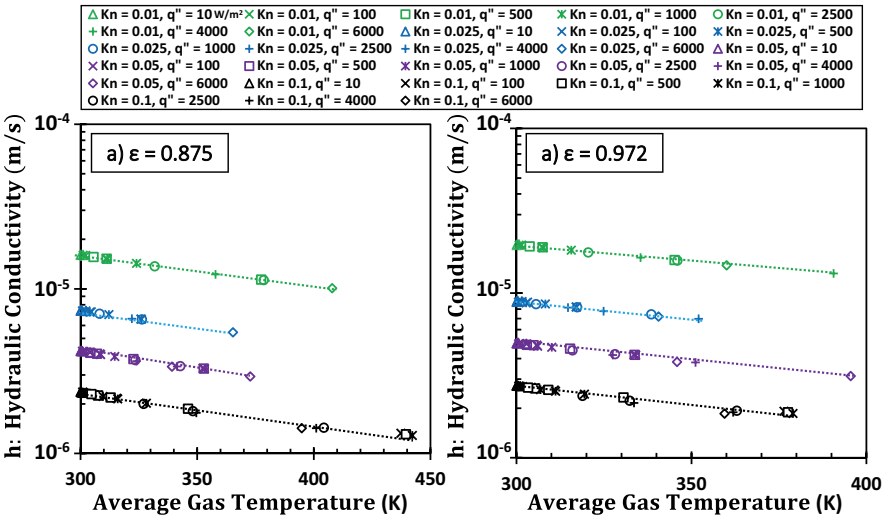

Figure 6.14. Change of hydraulic conductivity with temperature gradient at different heat fluxes and rarefaction levels.

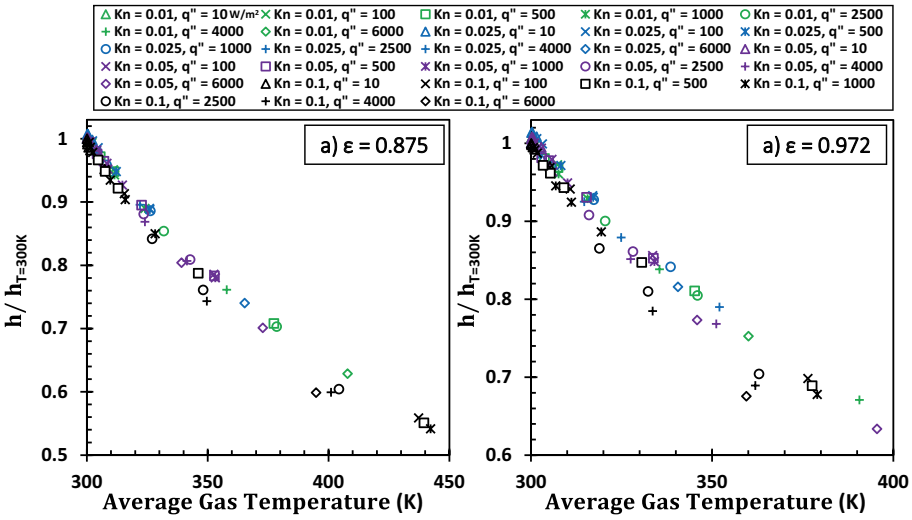

Figure 6.15. Hydraulic conductivity normalized by its value at 300K .

In Figure 6.16 the dimensionless form of temperature variations inside the metal foams is illustrated. In all cases the normalized temperature fields were calculated at the same mass flow rate and Re value. It is obvious that the temperature is at its minimum level at the inlet and then it is rising through the exist section. Since the rarefaction has a negative effect on convection, the result of high Kn values shows less contribution to enhancement of heat transfer.

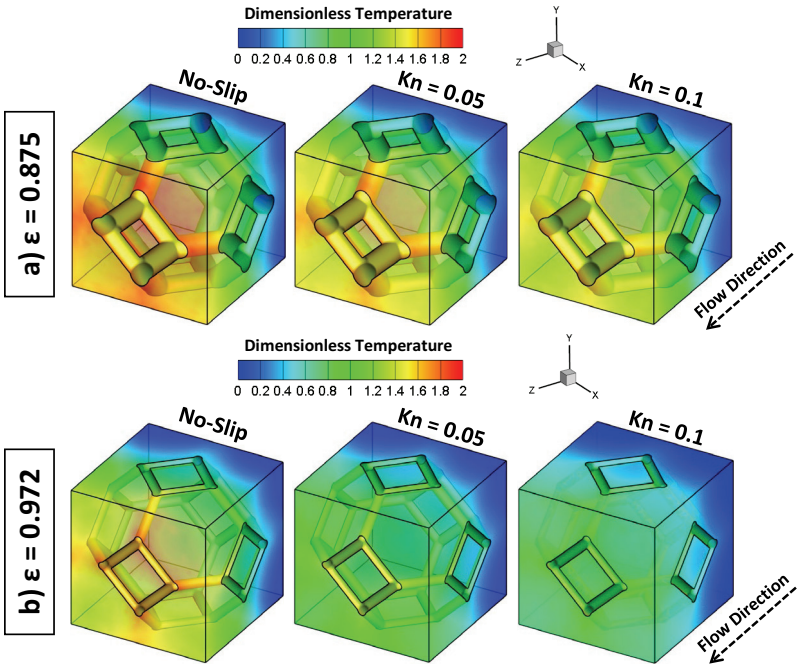

Figure 6.16. Dimensionless temperature contours at different rarefaction levels.

Lastly, the effect of temperature gradient on Nusselt number through a pressure driven fluid flow was analyzed. Interestingly, the variation of Nu when measured based

on reference temperature showed a collective behavior similar to the previous findings. The results for variable heat flux with different thermophysical properties shows that the Nu number is independent from Kn number. This is a very interesting behavior which should be properly investigated. Further assessment may be related by evaluation of entropy generation which measure of dissipated energy and degradation of the performance of systems.

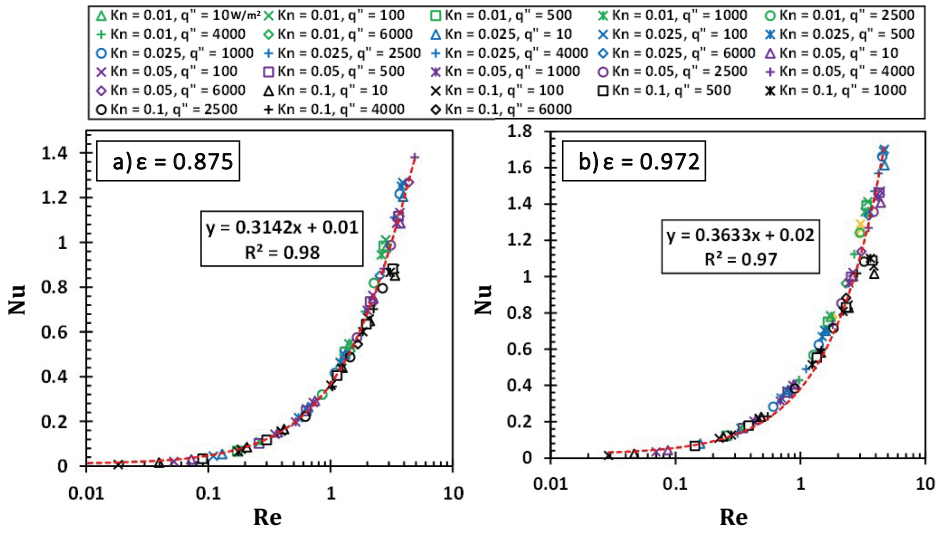

Figure 6.17. Variation of Nusselt values at different temperature and rarefaction levels.

6.3. Conclusion

Pore-level gas dynamic analysis in slip flow regime was performed through a metallic foam with kelvin cell structure. Non-equilibrium effects developed in gas dynamics due to microscale flow domain. Permeability values were calculated using Darcy-Forchheimer model for a wide range of Re values covering both Darcy and non-Darcy flows regimes. Rarefaction enhanced the transport and decreased the inertial effects. By increasing Kn number, permeability increased while the Forchheimer coefficients decreased. Rarefaction effects were stronger in lower porosity cases. At specific case $\varepsilon = 0.875$, 60% increase in permeability was observed at $Kn = 0.1$ compared to no-slip permeability. At high velocities where the inertial effects were expected to be dominant, an increase of Kn number results in a decrease of drag forces. Hence, less distorted, and mostly uniform velocity fields were formed through the porous structures by increasing rarefaction levels. For the characterization of heat transfer, convection

coefficients were calculated. At the low heat flux working condition, temperature jumps at the foam surfaces remained low yielding limited effects on Nusselt values. Nu number was found depending mostly on Re number, independent of rarefaction. Variation of Nu by Re was described based on a power-law model at different porosities. The proposed model can successfully predict the Nu values of different Re flows in a Kelvin cell at different porosities. Next, a variable heat fluxes were applied on strut surfaces for two different porosities. It is observed that by changing the temperature the variation of dimensionless pressure drops and permeability at different rarefaction levels remained constant. Hence, to characterize the transport and capture other effects due to change of fluid properties hydraulic conductivity were measured. The results showed that the hydraulic conductivity decreases as the temperature increased. It is also observed that the Nusselt number is still independent of rarefaction by applying variable heat flux. This behavior should be investigated further with help of other methos such as evaluation of entropy generation.

CHAPTER 7

SUMMARY

In this thesis, a pore level numerical simulation is performed to characterize transport at a moderate slip flow regime in micro/nano-scale porous medium. Since an accurate transport solution is a fundamental feature for many applications, the need to investigate flow characteristics in these systems becomes crucial. Although many studies have solved gas transport in micro/nano-scale porous media, they did not properly include all the geometrical parameters such as pore throat size ratio with rarefaction effects into porous fluid analysis. Hence, the current study aims to contribute to the community to fill the lack of knowledge on this aspect of transport in micro/nano-scale porous medium.

In Chapter 1, a broad introduction about gas transport at micro/nano-scale levels is described. The gas flow regime with their corresponding solution methods is given. In the next step, gas flows were estimates by Klinkenberg theory at micro/nano-scale porous media. The discussion about different literature on Klinkenberg theory is summarized and tabulated in the next part of this chapter. Finally, the importance of including pore connectivity and pore to throat size ratio definition on transport is supported by some examples from the literature.

In chapter 2, theoretical background on different methods to solve transport inside the porous medium is given. The difference between pore-scale method (PSM) and volume average method (VAM) is demonstrated and formulated. Next, Darcy law and Kozeny-Carman equation are addressed. After that, the representative porous model selected in this study and the geometrical parameter calculations used for the next three following chapters are explained in detail.

In chapter 3, the significant role of throat size together with rarefaction on the calculation of permeability was considered. Parametric study results showed that, by increasing porosity and rarefaction, permeability values increased. However, for a given porosity, permeability values decreased as the value of R_{pt} increased since the substantial existence of secondary flows influences the main flow. Next, it is observed that by calculating Kn number based on an equivalent diameter at different pore to throat size ratios, the results were achieved in the form of Klinkenberg suggested model. The model was then extended with Kozeny-Carman relation to calculate the intrinsic permeability.

Finally, for all cases, it is demonstrated that the computational outcomes and the results calculated from the model were in good conformity.

In Chapter 4, the effect of the intraparticle region on transport is investigated. The results showed that except for limited cases, the permeability values were lower with respect to mono-scale results. It is observed that only when the throat size ratios become comparable in size with intraparticle thickness the permeabilities reach higher values. Once again, by calculating the equivalent diameter from apparent permeability for such porous structure, the extended phenomenological model given in the chapter 3 onto current results match with an excellent agreement. Hence, the equivalent diameter-based solution showed that permeability variation is only a porosity function, independent of other structural parameters.

In Chapter 5, a pressure-driven flow in a representative elementary volume with a three-dimensional network of the porous system is considered. The permeability values were estimated at different rarefaction levels by changing the porosity and pore size ratio in the main flow direction. The results showed that the previous empirical model could successfully be employed on the three-dimensional porous system at various geometrical and slip conditions. By modifying the value of Klinkenberg constant for three-dimensional flow, the proposed relation provides the apparent gas permeability in terms of porosity, Darcy length of the porous system, intrinsic permeability (Kn = 0), and Kn_{Darcy} as an extension of the Klinkenberg model.

In Chapter 6, gas transport in metal foams which belongs to the class of porous medium, is analyzed at slip flow regime. The current study performed a wide range of pore-level analyses of convective gas flows with constant and variable thermophysical properties in a Kelvin cell model through Darcy to Forchheimer flow regimes. It is observed that permeability increased up to 60% by increasing rarefaction while the rarefaction lessened the inertial effects such that Forchheimer coefficients decreased substantially. On the other hand, the positive influence of boundary slip and the negative effect of temperature jump developing between gas and solid almost canceled each other at variable heat flux regions. Hence, Nusselt numbers were found mostly related to Reynolds number independent from rarefaction. Additionally, it is found that the permeability of the system remains the same with temperature variation. In this situation, hydraulic conductivity is calculated. The normalized value of hydraulic conductivity shows that the results were independent of rarefaction effects and only as a function of temperature.

REFERENCES

1. Mulder, M. *Basic Principles of Membrane Technology*. *Basic Principles of Membrane Technology* (Springer Netherlands, 1991).
2. Wang, B. *et al.* Influence of intrinsic permeability of reservoir rocks on gas recovery from hydrate deposits via a combined depressurization and thermal stimulation approach. *Appl. Energy* **229**, 858–871 (2018).
3. Rebordão, G., Palma, S. I. C. J. & Roque, A. C. A. Microfluidics in gas sensing and artificial olfaction. *Sensors (Switzerland)* **20**, 1–22 (2020).
4. Yave, W., Car, A., Funari, S. S., Nunes, S. P. & Peinemann, K. V. CO2-Philic polymer membrane with extremely high separation performance. *Macromolecules* **43**, 326–333 (2010).
5. Shui, L., Pennathur, S., Pennathur, S., Eijkel, J. C. T. & Berg, A. van den. Multiphase flow in lab on chip devices: A real tool for the future?†. *Lab Chip* **8**, 1010–1014 (2008).
6. Karniadakis, G., Beşkök, A. & Aluru, N. R. *Microflows and nanoflows : fundamentals and simulation*. (Springer, 2005).
7. Barisik, M. & Beskok, A. Molecular dynamics simulations of shear-driven gas flows in nano-channels. *Microfluid. Nanofluidics* **11**, 611–622 (2011).
8. Barisik, M. & Beskok, A. MD Simulations of Nano-Scale Gas Flows: A Case Study of Couette Flow at Kn = 10. in 707–711 (2011).
9. Barisik, M. & Beskok, A. Surface–gas interaction effects on nanoscale gas flows. *Microfluid. Nanofluidics* **13**, 789–798 (2012).
10. Nazari Moghaddam, R. & Jamiolahmady, M. Slip flow in porous media. *Fuel* **173**, 298–310 (2016).
11. Zhang, P., Hu, L. & Meegoda, J. N. Pore-Scale Simulation and Sensitivity Analysis of Apparent Gas Permeability in Shale Matrix. *Mater. (Basel, Switzerland)* **10**, (2017).
12. Kampf, S. K. & Mirus, B. B. Subsurface and Surface Flow Leading to Channel Initiation. *Ref. Modul. Earth Syst. Environ. Sci.* (2021).
13. Hao, L. & Cheng, P. Pore-scale simulations on relative permeabilities of porous media by lattice Boltzmann method. *Int. J. Heat Mass Transf.* **53**, 1908–1913 (2010).

14. Zhao, B. *et al.* Comprehensive comparison of pore-scale models for multiphase flow in porous media. *Proc. Natl. Acad. Sci.* **116**, 13799–13806 (2019).
15. Wang, L., Wang, L. P., Guo, Z. & Mi, J. Volume-averaged macroscopic equation for fluid flow in moving porous media. *Int. J. Heat Mass Transf.* **82**, 357–368 (2015).
16. LAGE, J. L. The fundamental theory of flow through permeable media from darcy to turbulence. *Transp. Phenom. Porous Media* 1–30 (1998).
17. Whitaker, S. The Method of Volume Averaging. **13**, (1999).
18. Celik, H., Mobedi, M., Nakayama, A. & Ozkol, U. A study on numerical determination of permeability and inertia coefficient of aluminum foam using X-ray microtomography technique: Focus on inspection methods for reliability (permeability and inertia coefficient by tomography). *J. Porous Media* **22**, 511–529 (2019).
19. Wu, J. *et al.* Porous Polymers as Multifunctional Material Platforms toward Task-Specific Applications. *Adv. Mater.* **31**, 1802922 (2019).
20. Lu, S., Cheng, Y. & Li, W. Model development and analysis of the evolution of coal permeability under different boundary conditions. *J. Nat. Gas Sci. Eng.* **31**, 129–138 (2016).
21. Celik, H., Mobedi, M., Nakayama, A. & Ozkol, U. A numerical study on determination of volume averaged thermal transport properties of metal foam structures using X-ray microtomography technique. *Numer. Heat Transf. Part A Appl.* **74**, 1368–1386 (2018).
22. Habib, R., Karimi, N., Yadollahi, B., Doranehgard, M. H. & Li, L. K. B. A pore-scale assessment of the dynamic response of forced convection in porous media to inlet flow modulations. *Int. J. Heat Mass Transf.* **153**, (2020).
23. Kawagoe, Y. *et al.* A study on pressure-driven gas transport in porous media: from nanoscale to microscale. *Microfluid. Nanofluidics* **20**, 162 (2016).
24. Zhao, J. *et al.* REV-scale simulation of gas transport in shale matrix with lattice Boltzmann method. *J. Nat. Gas Sci. Eng.* **57**, 224–237 (2018).
25. Duan, Z. & Yovanovich, M. M. Models for Gaseous Slip Flow in Circular and Noncircular Microchannels. in *ASME 2010 8th International Conference on Nanochannels, Microchannels, and Minichannels: Parts A and B* 421–431 (2010).
26. Klinkenberg, L. J. The Permeability Of Porous Media To Liquids And Gases. (1941).

27. Heid, J. G., McMahon, J. J., Nielsen, R. F. & Yuster, S. T. Study of the permeability of rocks to homogeneous fluids. in *Drilling and Production Practice 1950* 230–246 (American Petroleum Institute, 1950).
28. Sampath, K. & Keighin, C. W. Factors affecting gas slippage in tight sandstones of cretaceous age in the uinta basin. *jpt j pet technol* **v 34**, (1982).
29. Florence, F. A., Rushing, J., Newsham, K. E. & Blasingame, T. A. Improved Permeability Prediction Relations for Low Permeability Sands. in *Rocky Mountain Oil & Gas Technology Symposium* (Society of Petroleum Engineers, 2007).
30. Jones, S. C. A Rapid Accurate Unsteady-State Klinkenberg Permeameter. *Soc. Pet. Eng. J.* **12**, 383–397 (1972).
31. Wu, Y. S., Pruess, K. & Persoff, P. Gas Flow in Porous Media with Klinkenberg Effects. *Transp. Porous Media* **32**, 117–137 (1998).
32. Tanikawa, W. & Shimamoto, T. Comparison of Klinkenberg-corrected gas permeability and water permeability in sedimentary rocks. *Int. J. Rock Mech. Min. Sci.* **46**, 229–238 (2009).
33. Darabi, H., Ettehad, A., Javadpour, F. & Sepehrnoori, K. Gas flow in ultra-tight shale strata. *J. Fluid Mech.* **710**, 641–658 (2012).
34. Duan, Q. B. & Yang, X. S. Experimental studies on gas and water permeability of fault rocks from the rupture of the 2008 Wenchuan earthquake, China. *Sci. China Earth Sci.* **57**, 2825–2834 (2014).
35. Civan, F. Effective correlation of apparent gas permeability in tight porous media. *Transp. Porous Media* **82**, 375–384 (2010).
36. Zheng, Q., Yu, B., Duan, Y. & Fang, Q. A fractal model for gas slippage factor in porous media in the slip flow regime. *Chem. Eng. Sci.* **87**, 209–215 (2013).
37. Ashrafi Moghadam, A. & Chalaturnyk, R. Expansion of the Klinkenberg's slippage equation to low permeability porous media. *Int. J. Coal Geol.* **123**, 2–9 (2014).
38. Wang, G., Ren, T., Wang, K. & Zhou, A. Improved apparent permeability models of gas flow in coal with Klinkenberg effect. *Fuel* **128**, 53–61 (2014).
39. Hooman, K. *et al.* A theoretical model to predict gas permeability for slip flow through a porous medium. *Appl. Therm. Eng.* **70**, 71–76 (2014).
40. Li, C., Xu, P., Qiu, S. & Zhou, Y. The gas effective permeability of porous media with Klinkenberg effect. *J. Nat. Gas Sci. Eng.* **34**, 534–540 (2016).
41. Zhu, W. C., Liu, J., Sheng, J. C. & Elsworth, D. Analysis of coupled gas flow and

deformation process with desorption and Klinkenberg effects in coal seams. *Int. J. Rock Mech. Min. Sci.* **44**, 971–980 (2007).

42. Tao, Y., Liu, D., Xu, J., Peng, S. & Nie, W. Investigation of the Klinkenberg effect on gas flow in coal matrices: A numerical study. *J. Nat. Gas Sci. Eng.* **30**, 237–247 (2016).
43. Li, J. & Sultan, A. S. Klinkenberg slippage effect in the permeability computations of shale gas by the pore-scale simulations. *J. Nat. Gas Sci. Eng.* **48**, 197–202 (2017).
44. Fundamentals of Well-log Interpretation: The Acquisition of Logging Data v. 1 : Oberto Serra : 9780444421326. https://www.bookdepository.com/Fundamentals-Well-log-Interpretation-Acquisition-Logging-Data-v-1-Oberto-Serra/9780444421326.
45. Huang, H. *et al.* Effects of pore-throat structure on gas permeability in the tight sandstone reservoirs of the Upper Triassic Yanchang formation in the Western Ordos Basin, China. *J. Pet. Sci. Eng.* **162**, 602–616 (2018).
46. Rezaee, M. R., Jafari, A. & Kazemzadeh, E. Relationships between permeability, porosity and pore throat size in carbonate rocks using regression analysis and neural networks. *J. Geophys. Eng.* **3**, 370–376 (2006).
47. Glover, P. W. & Déry, N. Streaming potential coupling coefficient of quartz glass bead packs: Dependence on grain diameter, pore size, and pore throat radius. *Geophysics* **75**, F225–F241 (2010).
48. Jin, Y., Liu, X., Liu, Z., Lu, S. & Xue, Q. Effect of interfacial layer on water flow in nanochannels: Lattice Boltzmann simulations. *Phys. B Condens. Matter* **487**, 18–24 (2016).
49. Zhang, Z., Shi, Y., Li, H. & Jin, W. Experimental study on the pore structure characteristics of tight sandstone reservoirs in Upper Triassic Ordos Basin China. **34**, 418–439 (2016).
50. Gao, H., Li, T. & Yang, L. Quantitative determination of pore and throat parameters in tight oil reservoir using constant rate mercury intrusion technique. *J. Pet. Explor. Prod. Technol. 2015 62* **6**, 309–318 (2015).
51. Xiao, D., Lu, S., Lu, Z., Huang, W. & Gu, M. Combining nuclear magnetic resonance and rate-controlled porosimetry to probe the pore-throat structure of tight sandstones. *Pet. Explor. Dev.* **43**, 1049–1059 (2016).
52. Cao, Z. *et al.* Pore structure characterization of Chang-7 tight sandstone using

MICP combined with N2GA techniques and its geological control factors. *Sci. Reports 2016 61* **6**, 1–13 (2016).

53. Massarotti, N., Nithiarasu, P. & Carotenuto, A. Microscopic and macroscopic approach for natural convection in enclosures filled with fluid saturated porous medium. *Int. J. Numer. Methods Heat Fluid Flow* **13**, 862–886 (2003).
54. Massarotti, N., Nithiarasu, P. & Carotenuto, A. Microscopic and macroscopic approach for natural convection in enclosures filled with fluid saturated porous medium. *Int. J. Numer. Methods Heat & Fluid Flow* **13**, 862–886 (2003).
55. Salvi Fernandes, J., Roberto Appoloni, C. & Peres Fernandes, C. Determination of the Representative Elementary Volume for the Study of Sandstones and Siltstones by X-Ray Microtomography. (2012).
56. Ukrainczyk, N. & Koenders, E. A. B. Representative elementary volumes for 3D modeling of mass transport in cementitious materials. *Model. Simul. Mater. Sci. Eng.* **22**, 035001 (2014).
57. Zerihun, Y. T. Extension of the dupuit-forchheimer model for non-hydrostatic flows in unconfined aquifers. *Fluids* **3**, (2018).
58. Darcy, H. *Les fontaines publiques de la ville de Dijon: exposition et application.* (1856).
59. Kuwahara, F., Nakayama, A. & Koyama, H. A Numerical Study of Thermal Dispersion in Porous Media. *J. Heat Transfer* **118**, 756 (1996).
60. Dupuit, J. *Etudes Théoriques et Pratiques sur le mouvement des Eaux dans les canaux découverts et à travers les terrains perméables*. (Dunod, 1863).
61. Forchheimer, P. Über die Ergiebigkeit von Brunnen-Anlagen und Sickerschlitzen. *Z. Archit. Ing.-Ver.* **32**, 539–563 (1886).
62. Sobieski, W. & Trykozko, A. Darcy's and forchheimer's laws in practice. part 1. the experiment. *Technical Sciences* vol. 17 (2014).
63. Knupp, P. M. & Lage, J. L. Generalization of the Forchheimer-extended Darcy flow model to the tensor premeability case via a variational principle. *J. Fluid Mech.* **299**, 97–104 (1995).
64. Buiting, J. J. M. & Clerke, E. A. Permeability from porosimetry measurements: Derivation for a tortuous and fractal tubular bundle. *J. Pet. Sci. Eng.* **108**, 267–278 (2013).
65. Zhong, W., Ji, X., Li, C., Fang, J. & Liu, F. Determination of Permeability and Inertial Coefficients of Sintered Metal Porous Media Using an Isothermal

Chamber. *Appl. Sci.* **8**, 1670 (2018).

66. Ma, J. Review of permeability evolution model for fractured porous media. *J. Rock Mech. Geotech. Eng.* **7**, 351–357 (2015).
67. Kozeny–Carman equation - Wikipedia. https://en.wikipedia.org/wiki/Kozeny–Carman_equation.
68. Ahmadi, M. M., Mohammadi, S. & Hayati, A. N. Analytical derivation of tortuosity and permeability of monosized spheres: A volume averaging approach. *Phys. Rev. E - Stat. Nonlinear, Soft Matter Phys.* **83**, (2011).
69. Carman, P. *L'Ecoulement des gaz à travers les milieux poreux*. (Institut national des sciences et techniques nucléaires ;;P.U.F., 1961).
70. Henderson, N., Brêttas, J. C. & Sacco, W. F. A three-parameter Kozeny–Carman generalized equation for fractal porous media. *Chem. Eng. Sci.* **65**, 4432–4442 (2010).
71. Brown, S. G. ., Spittle, J. ., Jarvis, D. . & Walden-Bevan, R. Numerical determination of liquid flow permeabilities for equiaxed dendritic structures. *Acta Mater.* **50**, 1559–1569 (2002).
72. Xiao, B., Tu, X., Ren, W. & Wang, Z. Modeling for hydraulic permeability and kozeny–carman constant of porous nanofibers using a fractal approach. *Fractals* **23**, 1550029 (2015).
73. Chen, X. & Papathanasiou, T. D. On the variability of the Kozeny constant for saturated flow across unidirectional disordered fiber arrays. *Compos. Part A Appl. Sci. Manuf.* **37**, 836–846 (2006).
74. Mavko, G. & Nur, A. The effect of a percolation threshold in the Kozeny-Carman relation. *GEOPHYSICS* **62**, 1480–1482 (1997).
75. Yang, S., Liang, M., Yu, B. & Zou, M. Permeability model for fractal porous media with rough surfaces. *Microfluid. Nanofluidics* **18**, 1085–1093 (2015).
76. Heijs, A. W. J. & Lowe, C. P. Numerical evaluation of the permeability and the Kozeny constant for two types of porous media. *Phys. Rev. E* **51**, 4346–4352 (1995).
77. Gamrat, G., Favre-Marinet, M. & Le Person, S. Numerical study of heat transfer over banks of rods in small Reynolds number cross-flow. *Int. J. Heat Mass Transf.* **51**, 853–864 (2008).
78. Latief, F. D. E. & Fauzi, U. Kozeny–Carman and empirical formula for the permeability of computer rock models. *Int. J. Rock Mech. Min. Sci.* **50**, 117–123

(2012).

79. Guo, B., Shan, L., Jiang, S., Li, G. & Lee, J. The maximum permissible fracturing pressure in shale gas wells for wellbore cement sheath integrity. *J. Nat. Gas Sci. Eng.* **56**, 324–332 (2018).
80. Costa, A. Permeability-porosity relationship: A reexamination of the Kozeny-Carman equation based on a fractal pore-space geometry assumption. *Geophys. Res. Lett.* **33**, L02318 (2006).
81. Xu, P. & Yu, B. Developing a new form of permeability and Kozeny-Carman constant for homogeneous porous media by means of fractal geometry. *Adv. Water Resour.* **31**, 74–81 (2008).
82. Shin, C. Tortuosity correction of Kozeny's hydraulic diameter of a porous medium. *Phys. Fluids* **29**, (2017).
83. Wang, K., Liu, A. & Zhou, A. Theoretical analysis of influencing factors on resistance in the process of gas migration in coal seams. *Int. J. Min. Sci. Technol.* **27**, 315–319 (2017).
84. Lee, K. S. & Kim, T. H. Petrophysical Characteristics of Shale Reservoirs. *Transp. Shale Reserv.* 7–34 (2019).
85. Kurtbas, I. & Celik, N. Experimental investigation of forced and mixed convection heat transfer in a foam-filled horizontal rectangular channel. *Int. J. Heat Mass Transf.* **52**, 1313–1325 (2009).
86. Calmidi, V. V. & Mahajan, R. L. Forced convection in high porosity metal foams. *J. Heat Transfer* **122**, 557–565 (2000).
87. Yang, K., Liu, K. & Wang, J. Pore-scale numerical simulation of convection heat transfer in high porosity open-cell metal foam under rotating conditions. *Appl. Therm. Eng.* **195**, 117168 (2021).
88. Barisik, M. & Beskok, A. "Law of the nano-wall" in nano-channel gas flows. *Microfluid. Nanofluidics* **20**, 46 (2016).
89. Beskok, A. & Barisik, M. Molecular Dynamics Studies on Nanoscale Gas Transport. in *Encyclopedia of Microfluidics and Nanofluidics* 2307–2315 (Springer New York, 2015).
90. Barisik, M., Kim, B. & Beskok, A. Smart Wall Model for Molecular Dynamics Simulations of Nanoscale Gas Flows. *Commun. Comput. Phys* (2010) doi:10.4208/cicp.2009.09.118.
91. Barisik, M. & Beskok, A. Molecular free paths in nanoscale gas flows. *Microfluid.*

Nanofluidics **18**, 1365–1371 (2015).

92. Sabet, S., Barisik, M., Mobedi, M. & Beskok, A. An extended Kozeny-Carman-Klinkenberg model for gas permeability in micro/nano-porous media. *Phys. Fluids* **31**, (2019).
93. Saada, M. A., Chikh, S. & Campo, A. Analysis of hydrodynamic and thermal dispersion in porous media by means of a local approach. *Heat Mass Transf.* **42**, 995–1006 (2006).
94. Ozgumus, T., Mobedi, M. & Ozkol, U. Determination of kozeny constant based on porosity and pore to throat size ratio in porous medium with rectangular rods. *Eng. Appl. Comput. Fluid Mech.* **8**, 308–318 (2014).
95. Hommel, J., Coltman, E. & Class, H. Porosity–Permeability Relations for Evolving Pore Space: A Review with a Focus on (Bio-)geochemically Altered Porous Media. *Transp. Porous Media 2018 1242* **124**, 589–629 (2018).
96. Vickerd, M. A., Thring, R. W., Arocena, J. M., Li, J. B. & Heck, R. J. Changes in Porosity Due to Acid Gas Injection As Determined by X-Ray Computed Tomography. *J. Can. Pet. Technol.* **45**, 17–22 (2006).
97. Ugur, I., Sengun, N., Demirdag, S. & Altindag, R. Analysis of the alterations in porosity features of some natural stones due to thermal effect. *Ultrasonics* **54**, 1332–1336 (2014).
98. Xie, M. *et al.* Implementation and evaluation of permeability-porosity and tortuosity-porosity relationships linked to mineral dissolution-precipitation. *Comput. Geosci. 2015 193* **19**, 655–671 (2014).
99. Jullien, M., Raynal, J., Kohler, É. & Bildstein, O. Physicochemical Reactivity in Clay-Rich Materials: Tools for Safety Assessment. *Oil Gas Sci. Technol.* **60**, 107–120 (2005).
100. Gerke, H. H. & van Genuchten, M. T. A dual-porosity model for simulating the preferential movement of water and solutes in structured porous media. *Water Resour. Res.* **29**, 305–319 (1993).
101. Adler, P. M. Transports in fractal porous media. *J. Hydrol.* **187**, 195–213 (1996).
102. Vogel, H. J. A numerical experiment on pore size, pore connectivity, water retention, permeability, and solute transport using network models. *Eur. J. Soil Sci.* **51**, 99–105 (2000).
103. Kuila, U. & Prasad, M. Surface area and pore-size distribution in clays and shales. *Proc. - SPE Annu. Tech. Conf. Exhib.* **4**, 2937–2949 (2011).

104. Heller, R., Vermylen, J. & Zoback, M. Experimental investigation of matrix permeability of gas shales. *Am. Assoc. Pet. Geol. Bull.* **98**, 975–995 (2014).
105. Kelly, S. A., Torres-Verdín, C. & Balhoff, M. T. Subsurface to substrate: dual-scale micro/nanofluidic networks for investigating transport anomalies in tight porous media. *Lab Chip* **16**, 2829–2839 (2016).
106. Yu, B. & Cheng, P. A fractal permeability model for bi-dispersed porous media. *Int. J. Heat Mass Transf.* **45**, 2983–2993 (2002).
107. Chastanet, J., Royer, P. & Auriault, J. L. Flow of low pressure gas through dual-porosity media. *Transp. Porous Media* **66**, 457–479 (2007).
108. Zheng, Q. & Yu, B. A fractal permeability model for gas flow through dual-porosity media. *J. Appl. Phys.* **111**, (2012).
109. Zhang, L. Z. A fractal model for gas permeation through porous membranes. *Int. J. Heat Mass Transf.* **51**, 5288–5295 (2008).
110. de Vries, E. T., Raoof, A. & van Genuchten, M. T. Multiscale modelling of dual-porosity porous media; a computational pore-scale study for flow and solute transport. *Adv. Water Resour.* **105**, 82–95 (2017).
111. Barrande, M., Bouchet, R. & Denoyel, R. Tortuosity of porous particles. *Anal. Chem.* **79**, 9115–9121 (2007).
112. H.J. Vogel, K. R. Quantitative morphology and network representation of soil pore structure. *Adv. Water Resour.* **24**, 233–242 (2001).
113. Marshall, T. J. A relation between permeability and size distribution of pores. *J. Soil Sci.* **9**, 1–8 (1958).
114. Dullien, F. A. L. Porous Media: Fluid Transport and Pore Structure. (1992).
115. Laakkonen, K. Method to model dryer fabrics in paper machine scale using small-scale simulations and porous media model. *Int. J. Heat Fluid Flow* **24**, 114–121 (2003).
116. Ball, B. C. Modeling of soil pores as tubes using gas permeabilities, gas diffusivities, and water release. *J. Soil Sci.* **32**, 465–481 (1981).
117. Liu, H., Wang, J., Xie, Y., Ma, D. & Shi, X. Flow characteristics of heavy oil through porous media. *Energy Sources, Part A Recover. Util. Environ. Eff.* **34**, 347–359 (2011).
118. Allen, M. B. Basic Mechanics of Oil Reservoir Flows. 1–86 (1988).
119. J.W. Crawford, N. M. I. M. Y. The relation between the moisture-release curve and the structure of soil. *Euro J. Soil Sci.* **46**, 369–375 (1995).

120. I.M. Young, J. W. C. C. R. New methods and models for characterising structural heterogeneity of soil. *Soil Till. Res.* **61**, 1–13 (2001).
121. O. Wanner, A. B. C. R. L. Modelling biofilm accumulation and mass transport in a porous medium under high substrate loading. *Biotechnol. Bioengrg.* **47**, 703–712 (1995).
122. P. Spanne, J. F. Thovert, C. J. Jacquin, W. B. Lindquist, K. W. Jones, P. M. Adler. Synchrotron computed microtomography of porous media: topology and transports. *Phys. Rev. Lett.* **73**, 2001–2004 (1994).
123. D.A. Coker, S. T. J. H. D. Morphology and physical properties of Fontainebleau sandstone via tomographic analysis. *J. Geophys. Res.* **101**, 497–506 (1996).
124. Hazlett, R. D. Statistical characterization and stochastic modeling of pore networks in relation to fluid flow. *Math. Geol.* **29**, 801–822 (1997).
125. W.B. Lindquist, A. V. J. D. T. F. W. Pore and throat size distributions measured from synchrotron X-ray tomographic images of Fontainbleau sandstones. *J. Geophys. Res.* **105B**, 21508 (2000).
126. C.H. Arns, M. A. K. W. V. P. N. S. M. Virtual permeametry on microtomographic images. *J. Pet. Sci. Eng.* **45**, 41–46 (2004).
127. Quiblier, J. A. A new three-dimensional modelling technique for studying porous media. *J. Colloid Interface Sci.* **98**, 84–102 (1984).
128. S. Bakke, P. E. Ø. 3D pore-scale modeling of sandstone and flow simulations in pore networks. *SPE J.* **2**, 136 (1997).
129. B. Biswal, C. M. R. H. Three-dimensional local porosity analysis of porous media. *Phys. A* **255**, 221–241 (1998).
130. Agrawal, A. & Agrawal, A. Three-dimensional simulation of gaseous slip flow in different aspect ratio microducts. *Phys. Fluids* **18**, 103604 (2006).
131. Farah, N., Ding, D. Y. & Wu, Y. S. Simulation of the impact of fracturing fluid induced formation damage in shale gas reservoirs. *Soc. Pet. Eng. - SPE Reserv. Simul. Symp. 2015* **2**, 1266–1284 (2015).
132. P.M. Adler, C. G. J. J. A. Q. Flow in simulated porous media. *Int. J. Multiph. Flow* **16**, 691–712 (1990).
133. Blunt, M. & King, P. Relative permeabilities from two- and three-dimensional pore-scale network modelling. *Transp. Porous Media 1991 64* **6**, 407–433 (1991).
134. Wu, K. *et al.* 3D Stochastic Modelling of Heterogeneous Porous Media – Applications to Reservoir Rocks. *Transp. Porous Media 2006 653* **65**, 443–467

(2006).

135. Marafini, E., La Rocca, M., Fiori, A., Battiato, I. & Prestininzi, P. Suitability of 2D modelling to evaluate flow properties in 3D porous media. *Transp. Porous Media 2020 1342* **134**, 315–329 (2020).
136. Warren, J. E. & Root, P. J. The Behavior of Naturally Fractured Reservoirs. *Soc. Pet. Eng. J.* **3**, 245–255 (1963).
137. Bahrami, H., Rezaee, R. & Hossain, M. Characterizing natural fractures productivity in tight gas reservoirs. *J. Pet. Explor. Prod. Technol.* **2**, 107–115 (2012).
138. Aguilera, R. Analysis of naturally fractured reservoirs from conventional well logs. *Jpt, J. Pet. Technol.* **28**, 764–772 (1976).
139. Wu, K. *et al.* 3D stochastic modelling of heterogeneous porous media - Applications to reservoir rocks. *Transp. Porous Media* **65**, 443–467 (2006).
140. Wang, H. Improved dual-porosity models for petrophysical analysis of vuggy reservoirs. *J. Geophys. Eng.* **14**, 758–768 (2017).
141. Warren, J. E. & Root, P. J. The Behavior of Naturally Fractured Reservoirs. *Soc. Pet. Eng. J.* **3**, 245–255 (1963).
142. Adler, P. M. Porous Media: Geometry and Transports. (1992).
143. A Koponen, M. K. J. T. Permeability and effective porosity of porous media. *Phys. Rev. E* **56**, 3319 (1997).
144. D Zhang, R. Z. S. C. W. S. Pore scale study of flow in porous media: scale dependency, REV, and statistical REV. *Geophys. Res. Lett.* **27**, 1195–1198 (2000).
145. Davies, G. J. & Zhen, S. *Review Metallic foams: their production, properties and applications*. *Journal of Materials Science* vol. 18 (1983).
146. Van Setten, B. A. A. L. *et al.* Stability of catalytic foam diesel-soot filters based on Cs2O, MoO3, and Cs2SO4 molten-salt catalysts. *Appl. Catal. B Environ.* **42**, 337–347 (2003).
147. Tan, W. C. *et al.* Overview of porous media/metal foam application in fuel cells and solar power systems. *Renew. Sustain. Energy Rev.* **96**, 181–197 (2018).
148. Li, Q., Flamant, G., Yuan, X., Neveu, P. & Luo, L. Compact heat exchangers: A review and future applications for a new generation of high temperature solar receivers. *Renewable and Sustainable Energy Reviews* vol. 15 4855–4875 (2011).
149. Rehman, T. ur & Ali, H. M. Thermal performance analysis of metallic foam-based heat sinks embedded with RT-54HC paraffin: an experimental investigation for

electronic cooling. *J. Therm. Anal. Calorim.* **140**, 979–990 (2020).

150. Lu, W., Zhao, C. Y. & Tassou, S. A. Thermal analysis on metal-foam filled heat exchangers. Part I: Metal-foam filled pipes. *Int. J. Heat Mass Transf.* **49**, 2751–2761 (2006).
151. Peles, Y., Koşar, A., Mishra, C., Kuo, C. J. & Schneider, B. Forced convective heat transfer across a pin fin micro heat sink. *Int. J. Heat Mass Transf.* **48**, 3615–3627 (2005).
152. Tunc, G. & Bayazitoglu, Y. Heat transfer in microtubes with viscous dissipation. *Int. J. Heat Mass Transf.* **44**, 2395–2403 (2001).
153. Cetin, B., Yazicioglu, A. G. & Kakac, S. Fluid flow in microtubes with axial conduction including rarefaction and viscous dissipation. *Int. Commun. Heat Mass Transf.* **35**, 535–544 (2008).
154. Shojaeian, M. & Koşar, A. Convective heat transfer and entropy generation analysis on Newtonian and non-Newtonian fluid flows between parallel-plates under slip boundary conditions. *Int. J. Heat Mass Transf.* **70**, 664–673 (2014).
155. Shokouhmand, H., Meghdadi Isfahani, A. H. & Shirani, E. Friction and heat transfer coefficient in micro and nano channels filled with porous media for wide range of Knudsen number. *Int. Commun. Heat Mass Transf.* **37**, 890–894 (2010).
156. Nield, D. A. & Kuznetsov, A. V. Forced convection with slip-flow in a channel or duct occupied by a hyper-porous medium saturated by a rarefied gas. *Transp. Porous Media* **64**, 161–170 (2006).
157. Buonomo, B., Manca, O. & Lauriat, G. Forced convection in micro-channels filled with porous media in local thermal non-equilibrium conditions. *Int. J. Therm. Sci.* **77**, 206–222 (2014).
158. Haddad, O. M., Abuzaid, M. M. & Al-Nimr, M. A. Developing Free-Convection Gas Flow in a Vertical Open-Ended Microchannel Filled with Porous Media. *Numer. Heat Transf. Part A Appl.* **48**, 693–710 (2005).
159. Shojaeian, M. & Dibaji, S. A. R. Three-dimensional numerical simulation of the slip flow through triangular microchannels. *Int. Commun. Heat Mass Transf.* **37**, 324–329 (2010).
160. Ruina, X., Yuli, H., Peixue, J. & Buxuan, W. Internal heat transfer coefficients in microporous media with rarefaction effects. *Sci. China Technol. Sci.* **55**, 2869–2876 (2012).
161. Hettiarachchi, H. D. M., Golubovic, M., Worek, W. M. & Minkowycz, W. J.

Three-dimensional laminar slip-flow and heat transfer in a rectangular microchannel with constant wall temperature. *Int. J. Heat Mass Transf.* **51**, 5088–5096 (2008).

162. Niazmand, H., Renksizbulut, M. & Saeedi, E. Developing slip-flow and heat transfer in trapezoidal microchannels. *Int. J. Heat Mass Transf.* **51**, 6126–6135 (2008).
163. Renksizbulut, M., Niazmand, H. & Tercan, G. Slip-flow and heat transfer in rectangular microchannels with constant wall temperature. *Int. J. Therm. Sci.* **45**, 870–881 (2006).
164. Tunc, G. & Bayazitoglu, Y. Heat transfer in rectangular microchannels. *Int. J. Heat Mass Transf.* **45**, 765–773 (2001).
165. Della Torre, A., Montenegro, G., Tabor, G. R. & Wears, M. L. CFD characterization of flow regimes inside open cell foam substrates. *Int. J. Heat Fluid Flow* **50**, 72–82 (2014).
166. Ambrosio, G. *et al.* The effect of open-cell metal foams strut shape on convection heat transfer and pressure drop. *Appl. Therm. Eng.* **103**, 333–343 (2016).
167. Jang, W. Y., Kraynik, A. M. & Kyriakides, S. On the microstructure of open-cell foams and its effect on elastic properties. *Int. J. Solids Struct.* **45**, 1845–1875 (2008).
168. Tabor, G., Yeo, O., Young, P. & Laity, P. CFD simulation of flow through an open cell foam. *Int. J. Mod. Phys. C* **19**, 703–715 (2008).
169. Evans, A. G., Hutchinson, J. W. & Ashby, M. F. Cellular metals. *Curr. Opin. Solid State Mater. Sci.* **3**, 288–303 (1998).
170. Giani, L., Groppi, G. & Tronconi, E. Heat transfer characterization of metallic foams. *Ind. Eng. Chem. Res.* **44**, 9078–9085 (2005).
171. Huu, T. T., Lacroix, M., Pham Huu, C., Schweich, D. & Edouard, D. Towards a more realistic modeling of solid foam: Use of the pentagonal dodecahedron geometry. *Chem. Eng. Sci.* **64**, 5131–5142 (2009).
172. Thomson, W. LXIII. On the division of space with minimum partitional area . *London, Edinburgh, Dublin Philos. Mag. J. Sci.* **24**, 503–514 (1887).
173. Cunsolo, S. *et al.* Lord kelvin and weaire-phelan foam models: Heat transfer and pressure drop. *J. Heat Transfer* **138**, (2016).
174. Pusterla, S., Barbato, M., Ortona, A. & D'Angelo, C. Numerical study of cell morphology effects on convective heat transfer in reticulated ceramics. *Int. J. Heat*

Mass Transf. **55**, 7902–7910 (2012).

175. Inayat, A. *et al.* Periodic open-cell foams: Pressure drop measurements and modeling of an ideal tetrakaidecahedra packing. *Chem. Eng. Sci.* **66**, 2758–2763 (2011).
176. Hooman, K. & Dukhan, N. A Theoretical Model with Experimental Verification to Predict Hydrodynamics of Foams. *Transp. Porous Media* **100**, 393–406 (2013).
177. Sullivan, R. M., Ghosn, L. J. & Lerch, B. A. A general tetrakaidecahedron model for open-celled foams. *Int. J. Solids Struct.* **45**, 1754–1765 (2008).
178. Lucci, F. *et al.* Performance of randomized Kelvin cell structures as catalytic substrates: Mass-transfer based analysis. *Chem. Eng. Sci.* **112**, 143–151 (2014).
179. Brakke, K. A. The surface evolver. *Exp. Math.* **1**, 141–165 (1992).
180. Calmidi, V. V. & Mahajan, R. L. Forced Convection in High Porosity Metal Foams. *J. Heat Transfer* **122**, 557–565 (2000).
181. Krishnan, S., Murthy, J. Y. & Garimella, S. V. Direct simulation of transport in open-cell metal foam. *J. Heat Transfer* **128**, 793–799 (2006).
182. Vafai, K. *Handbook of porous media*. (CRC Press, 2015).
183. Kaviany, M. *Principles of Heat Transfer in Porous Media*. (Springer New York, 1995).

VITA

SAFA SABET

EDUCATION

- Ph.D. in Mechanical Engineering, İzmir Institute of Technology (2021)
- Researcher in Engineering Department of Università degli Studi della Campania "Luigi Vanvitelli" (2020)
- M.Sc. in Mechanical Engineering, İzmir Institute of Technology (2015)
- B.Sc. in Mechanical Engineering, İzmir Institute of Technology (2013)

RESEARCH INTERESTS

CFD, Heat Transfer, Micro/nano-scale Transport, Microfluidics, Numerical Methods, Porous Transport

LANGUAGE

Persian (Native), Turkish (Native), English (Full professional proficiency), Italian (Beginner)

PUBLICATIONS

- **Sabet, S.**, Mobedi, M. & Ozgumus, T. A pore scale study on fluid flow through two-dimensional dual scale porous media with small number of intraparticle pores. Polish J. Chem. Technol. 18, 80–92 (2016).
- **Sabet, S.**, Mobedi, M., Barisik, M. & Nakayama, A. Numerical determination of interfacial heat transfer coefficient for an aligned dual scale porous medium. Int. J. Numer. Methods Heat Fluid Flow 28, 2716–2733 (2018).
- **Sabet, S.**, Barisik, M., Mobedi, M. & Beskok, A. An extended Kozeny-Carman-Klinkenberg model for gas permeability in micro/nano-porous media. Phys. Fluids 31, (2019).
- **Sabet, S.**, Barisik, M., Buonomo, B. & Manca, O. Thermal and hydrodynamic behavior of forced convection gaseous slip flow in a Kelvin cell metal foam. Int. Commun. Heat Mass Transf. 131, 105838 (2022).